

Washington University in St. Louis

Washington University Open Scholarship

All Theses and Dissertations (ETDs)

1-1-2011

Novel Plasmonic Nanostructures for Applications in Sensing, Imaging, and Controlled Release

Weiyang Li

Washington University in St. Louis

Follow this and additional works at: <https://openscholarship.wustl.edu/etd>

Recommended Citation

Li, Weiyang, "Novel Plasmonic Nanostructures for Applications in Sensing, Imaging, and Controlled Release" (2011). *All Theses and Dissertations (ETDs)*. 609.

<https://openscholarship.wustl.edu/etd/609>

This Dissertation is brought to you for free and open access by Washington University Open Scholarship. It has been accepted for inclusion in All Theses and Dissertations (ETDs) by an authorized administrator of Washington University Open Scholarship. For more information, please contact digital@wumail.wustl.edu.

WASHINGTON UNIVERSITY IN ST. LOUIS

School of Engineering and Applied Science
Department of Biomedical Engineering

Dissertation Examination Committee:

Younan Xia, Chair
Mark Anastasio
Da-Ren Chen
Donald Elbert
Samuel Wickline
Pamela Woodard

Novel Plasmonic Nanostructures for Applications
in Sensing, Imaging, and Controlled Release

by

Weiyang Li

A dissertation presented to the
Graduate School of Arts and Sciences
of Washington University
in partial fulfillment of the
requirements for the degree of

DOCTOR OF PHILOSOPHY

December 2011
Saint Louis, Missouri

ABSTRACT OF THE DISSERTATION

Novel Plasmonic Nanostructures for Applications in
Sensing, Imaging, and Controlled Release

by

Weiyang Li

Doctor of Philosophy in Biomedical Engineering

Washington University in St. Louis, 2011

Professor Younan Xia, Chairperson

This research placed emphasis on engineering the properties of novel plasmonic nanostructures, especially silver (Ag) and gold (Au) nanostructures with well-defined shapes, for biomedical applications in sensing, imaging and drug delivery.

The first part of this work focused on the development of novel dimeric nanostructures of Ag for surface-enhanced Raman scattering (SERS) applications. In this section, I successfully demonstrated the synthesis of well-defined Ag dimers consisting of nanospheres with a broad range of sizes by using two methods. The first method was based on polyol process and the second was based on wet etching. The key for the dimerization process is to control the colloidal stability by adding appropriate amount of ionic species. I then investigated the SERS properties of the dimers of Ag nanospheres with various sizes and the application of using these dimers as SERS tags for Raman mapping of cancer cells.

The second part of this work systematically investigated the use of Au nanocages as a novel class of optical tracers for noninvasive sentinel lymph node (SLN) imaging

by photoacoustic (PA) tomography. The transport kinetics of Au nanocages in a lymphatic system was evaluated by PA imaging on the axillary region of a rat. Several experimental parameters, including the injection concentration, particle size, and surface charge were systematically studied. Quantification of the amount of nanocages accumulated in the lymph nodes was achieved by correlating the data from PA imaging with the results from inductively-coupled plasma mass spectrometry.

In the final part of this work, I focused on the development of Au nanocages as a new platform for controlled drug release. Two temperature-regulated systems were developed by combining Au nanocages with high-intensity focused ultrasound (HIFU). Because it can penetrate more deeply into soft tissues than near-infrared light, HIFU is a potentially more effective external stimulus for rapid, on-demand drug release. The first system was based on nanocages covered with smart, thermally-responsive polymers, and the second was based on nanocages filled with a biocompatible phase-change material. The released dosage could be remotely controlled by manipulating the power of HIFU and/or the duration of exposure. Localization and depth capability of the HIFU-controlled release have also been investigated.

ACKNOWLEDGEMENTS

First of all, I would like to express my sincere appreciation to my advisor, Professor Younan Xia, for his guidance and continuous support during my Ph. D. study. His extensive knowledge, creative thinking, and insightful understanding of science have been the source of inspiration for me throughout this work. I would also like to thank Dr. Dong Qin for her support and advice, and for her effort to build a Nano Research Facility at Washington University, which played an important role in my research. I would like to express gratitude to the excellent collaborators, in particular, Xin Cai in Prof. Lihong Wang's group for high-intensity focused ultrasound and photoacoustic imaging, and Professor Zhi-Yuan Li at the Institute of Physics, Chinese Academy of Sciences for DDA calculations. I am also very thankful to Prof. Lihong Wang for giving me valuable advice on the projects we collaborated on. Special thanks go to Prof. Jingyi Chen, Dr. Claire Cobley, Xiaohu Xia, Dr. Rui Deng, Dr. Guorong Sun, Dr. Matthew Rycenga, Yu Zhang, Dr. Yucai Wang, Dr. Qiang Zhang, Miaoxin Yang, and Yiyun Zheng, for all their help on my research. I would like to thank all past and current members of the Xia group, in particular Dr. Pedro Camargo, Dr. Eric Lee, Dr. Yanyun Ma, Dr. Jie Zeng, Prof. Hui Zhang, Prof. Xianmao Lu, Prof. Zhengquan Li, Prof. Xiaofeng Lu, Dr. Xiaoran Li, and Mingshang Jin. I would also like to express my gratitude to Prof. Frank Yin for his help and all the staff in the BME department, in particular, Lori Williams, Karen Teasdale and Glen Reitz. I am very grateful to my committee members, Prof. Mark Anastasio, Prof. Da-ren Chen, Prof. Donald Elbert, Prof. Samuel Wickline, Prof. Palama Woodard, and Prof. Barani Raman for their assistance and patience during the pursuing of my Ph. D degree.

DEDICATION

To my parents,
Chunzhen Wang and Lihui Li

To my husband,
Sheng Liu

TABLE OF CONTENTS

	Page
Abstract.....	ii
Acknowledgments.....	iv
List of Figures.....	ix
List of Tables.....	xiii
List of Abbreviations.....	xiv
Chapter 1. Introduction.....	1
1.1 Plasmonics and Metal Nanostructures.....	1
1.2 Plasmonic Nanostructures and Their Applications.....	2
1.3 Scope of This Work.....	6
1.4 References for Chapter 1.....	11
Chapter 2. Novel Dimeric Nanostructures of Silver for Surface-Enhanced Raman Scattering (SERS) Applications.....	14
2.1 Introduction.....	14
2.2 Syntheses of Dimers of Silver Nanospheres.....	17
2.2.1 Dimerization Based on the Polyol Process.....	17
2.2.2 Dimerization Based on the Etching Process.....	23
2.3 SERS Properties of Dimers of Silver Nanospheres with Different Sizes.....	28
2.3.1 SERS of the Dimers Prepared Using the Polyol Process.....	29

2.3.2	SERS of the Dimers Prepared Using the Etching Process.....	32
2.4	Dimers of Silver Nanospheres as SERS Tags for Raman Imaging	33
2.4.1	Structural and Optical Characterization of the SERS Tags	34
2.4.2	Raman Characterization of the SERS Tags	34
2.4.3	SERS Tags for Cancer Cells Imaging.....	36
2.5	Summary	37
2.6	Experimental Section	38
2.7	References for Chapter 2	62
Chapter 3.	Quantitative Evaluation of the Transport Kinetics of Gold Nanocages in a Lymphatic System by Photoacoustic (PA) Tomography	66
3.1	Introduction.....	66
3.2	<i>Ex Vivo</i> and <i>In Vivo</i> Sensitivity of PA Tomography for SLN Imaging with Gold Nanocages.....	69
3.3	Depth Capability of PA Tomography for SLN Imaging with Gold Nanocages.....	72
3.4	Comparison of Gold Nanocages with Different Sizes.....	73
3.5	Comparison of Gold Nanocages with Different Surface Charges.....	74
3.6	Summary	77
3.7	Experimental Section	78
3.8	References for Chapter 3	91

Chapter 4. Gold Nanocages for Controlled Release by High Intensity Focused Ultrasound (HIFU)	94
4.1 Introduction.....	94
4.2 A Controlled Release System Based on Gold Nanocages Covered with Smart Polymers.....	97
4.2.1 Experimental Setup and Mechanism	97
4.2.2 Synthesis of Thermally-Responsive Polymers	98
4.2.3 Surface Modification of Gold Nanocages.....	99
4.2.4 HIFU-Controlled Release for the Gold Nanocages Covered with Smart Polymers	100
4.2.5 Localization of the HIFU-Controlled Release	101
4.2.6 Depth Capability of the HIFU-Controlled Release.....	104
4.3 A Controlled Release System Based on Gold Nanocages Loaded with Phase-Change Material (PCM).....	104
4.3.1 Mechanism.....	104
4.3.2 HIFU-Controlled Release for the Gold Nanocages Loaded with PCM/Dye.....	106
4.4 Summary	108
4.5 Experimental Section.....	108
4.6 References for Chapter 4	130

LIST OF FIGURES

1.1 Schematic illustration of the LSPR phenomenon of a metal nanosphere	9
1.2 SEM, TEM images and UV-vis spectra of Ag nanocubes and Au nanocages	10
2.1 TEM and HRTEM images of dimers consisting of 30-nm Ag nanospheres	44
2.2 TEM images and UV-vis extinction spectra of samples obtained at different stages of the reaction for synthesizing the Ag dimer	45
2.3 TEM images of samples prepared with the addition of different amounts of NaCl/EG solution.....	46
2.4 A schematic showing how dimers of Ag nanospheres are formed during etching of Ag nanocubes	47
2.5 SEM and TEM images of dimers of Ag nanospheres prepared from 100-nm Ag nanocubes.....	48
2.6 SEM and TEM images of dimers of Ag nanospheres with different sizes prepared from 82-nm and 47-nm Ag nanocubes	49
2.7 SEM images of Ag nanocubes with an average edge length of 100 nm, 82 nm, and 47 nm	51
2.8 UV-vis extinction spectra of Ag nanocubes and dimers of Ag nanospheres.....	52
2.9 SEM images and EDX spectrum of the samples obtained without the addition of PVP	53
2.10 SERS spectra of a Ag dimer consisting of 30-nm nanospheres.....	54
2.11 SERS spectra of a Ag dimer consisting of 80-nm nanospheres.....	55
2.12 TEM images and UV-vis spectra of three different SERS tags.....	57

2.13 SERS spectra of individual SERS tags deposited on glass slides.....	58
2.14 SERS spectra obtained from aqueous suspensions of three different SERS tags	59
2.15 SERS images of SK-BR-3 cells incubated with SERS tags conjugated with anti-HER2 antibodies	61
3.1 TEM images of Au nanocages with average edge lengths of 50 nm and 30 nm...	83
3.2 PA signals recorded from gelatin phantoms containing Au nanocages at various concentrations	84
3.3 PA images of the axillary region of rats acquired at 0, 5, and 120 min after injection of the Au nanocages with different concentrations	85
3.4 PA signal enhancement in SLNs as a function of time after the injection of the Au nanocages with different concentrations.....	86
3.5 PA imaging of SLN at different depths after the injection Au nanocages.....	87
3.6 PA signal enhancement in SLNs after the injection of 50-nm and 30-nm Au nanocages.....	88
3.7 PA images acquired before, 5 min, and 60 min after the injection of Au nanocages with different surface charges.....	89
3.8 PA signal enhancement in SLNs as a function of time post injection of Au nanocages with different surface charges	90
3.9 PA images showing the transport of Au nanocages from SLN to LN2 and LN3.....	91
4.1 Schematic illustrations of the setup for HIFU experiments and how the controlled-release system works	117

4.2 Procedure for the synthesis of poly(NIPAAm- <i>co</i> -AAm) copolymers through RAFT copolymerization	118
4.3 ¹ H-NMR and quantitative ¹³ C NMR spectra of the poly(NIPAAm- <i>co</i> -AAm) copolymers.....	119
4.4 The LCST of the poly(NIPAAm- <i>co</i> -AAm) copolymers measured spectrophotometrically	120
4.5 TEM image and UV-vis spectrum of the Au nanocages functionalized with poly(NIPAAm- <i>co</i> -AAm).....	121
4.6 Controlled release of R6G from Au nanocages covered by a copolymer with an LCST at 38.5 °C.....	122
4.7 The absorption spectra taken before the release and after the samples had been heated at 37 °C for 48 h	123
4.8 The changes in temperature measured at the focal volume of HIFU for aqueous suspensions of Au nanocages	124
4.9 Fluorescence microscopy images of the gelatin phantom with dye-loaded Au nanocages before and after exposure to HIFU.....	125
4.10 Fluorescence microscopy images of the gelatin phantoms that were covered with chicken breast tissues of two different thicknesses and then exposed to HIFU	126
4.11 Schematic illustrating the release of drugs from Au nanocages loaded with a drug-doped PCM.....	127
4.12 Release profiles of R6G by direct heating and by HIFU	128

4.13 Photobleaching ratio of R6G and MB in aqueous solutions as a function of exposure time at room temperature	129
4.14 Release profiles of MB from PCM/dye loaded nanocages at 37 °C and 40 °C.....	130

LIST OF TABLES

2.1 A summary of the edge lengths of the Ag nanocubes, diameters of the resultant spheres in the dimers after etching, percentages of dimerization, and widths of the gap regions in the dimers	50
2.2 EFs for dimers of Ag nanospheres with the laser polarization parallel and perpendicular to the dimer's longitudinal axis, as well as those of the corresponding spheres.....	56
2.3 The EFs of individual SERS tags supported on glass slides and EFs of the different SERS tags in solution phase.....	60

LIST OF ABBREVIATIONS

AuNCs	Au nanocages
1,4-BDT	1,4-Benzenedithiol
BV	Blood Vessel
DCC	<i>N,N'</i> -Dicyclohexylcarbodiimide
DMAP	4-Dimethylaminopyridine
EDX	Energy Dispersion X-ray
EF	Enhancement Factor
E-field	Electromagnetic Field
EG	Ethylene Glycol
<i>fcc</i>	Face Centered Cubic
HIFU	High-intensity focused ultrasound
ICP-MS	Inductively Coupled Plasma Mass Spectroscopy
LSPR	Localized Surface Plasmon Resonance
LV	Lymphatic Vessel
MB	Methylene Blue
4-MBA	4-Mercapto Benzoic acid
4-MBT	4-Methyl Benzenethiol
NIR	Near-Infrared
PA	Photoacoustic
PBS	Phosphate Buffered Saline
PCM	Phase-Change Material

PEG	Poly(ethylene glycol)
PVP	Poly(vinyl pyrrolidone)
R6G	Rhodamine 6G
rpm	Revolutions Per Minute
SEM	Scanning Electron Microscopy
SERS	Surface Enhanced Raman Scattering
SLN	Sentinel Lymph Node
SNR	Signal to Noise Ratio
TEM	Transmission Electron Microscopy
TEOS	Tetraethyl Orthosilicate
UV-vis	Ultraviolet-visible

Chapter 1

Introduction

1.1. Plasmonics and Metal Nanostructures

Plasmonics refers to the study of light-matter interactions that can be used to localize and manipulate electromagnetic waves down to the length of nanometer scale.^[1,2] The key component of plasmonics is metal nanostructures, which can serve as antennas to convert light into localized electromagnetic fields (E-fields) or as waveguides to route light to desired locations with nanometer precision. All of these are realized through a resonant interaction between the incident light and free electrons in the nanostructures. When a metal nanoparticle is illuminated with an electromagnetic wave, the delocalized conduction electrons of the metal will begin to oscillate collectively relative to the lattice of positive ions, creating intense scattering and absorption at resonant wavelengths. This phenomenon has been widely known as localized surface plasmon resonance (LSPR).^[3] Here, *surface* refers to the polarization of surface charges resulting from collective electron oscillations; *plasmon* is in analogy to the collective electron oscillations within gaseous plasma; *localized* indicates that the oscillation of plasmon is confined to the surface of a nanostructure.

Figure 1.1 illustrates the LSPR phenomenon for a metal nanosphere with a size much smaller than the wavelength of light.^[4] For a small, spherical nanoparticle, the

surface plasmon oscillation is dominated by the dipolar mode with a polarizability α given by the equation as below: ^[5]

$$\alpha = r^3(\varepsilon - \varepsilon_m)/(\varepsilon + 2\varepsilon_m) \quad (1)$$

where r is the radius of the sphere, ε_m is the dielectric constant of the external environment, and ε is the complex dielectric function of the metal nanoparticle, which is given by:

$$\varepsilon(\omega) = \varepsilon_r(\omega) + i\varepsilon_i(\omega) \quad (2)$$

where ε_r and ε_i denote the real and imaginary part of ε , respectively, expressed as a function of the frequency (ω) of light. As such, the strongest resonance occurs at a frequency ω where $\varepsilon_r = -2\varepsilon_m$ (when the denominator of equation 1 equals zero), thus determining the LSPR frequency.

The large optical polarization associated with the LSPR enables enhanced E-fields near the nanoparticle surface, as well as strong absorption and scattering of light at the LSPR frequency, thus imparting unique optical properties to the nanoparticles. The LSPR frequency is highly dependent on the size, shape, and structure (solid vs. hollow) of the nanoparticles, as well as the dielectric properties of the surrounding medium and inter-nanoparticle coupling interactions.^[3,6-10] By tailoring these parameters, one can readily manipulate the LSPR properties of plasmonic nanoparticles for a variety of applications.

1.2. Applications of Plasmonic Nanostructures

The bright colors of noble metal nanoparticles, especially those of gold (Au) and

silver (Ag), have attracted considerable attention since historical times as decorative pigments in stained glasses and artworks. In recent times, the rapid advances in the synthesis of metal nanoparticles with controllable sizes, shapes as well as tunable LSPR properties have enabled a rich variety of applications in photonics, catalysis, information storage, chemical/biological sensing, and biomedicine.^[11-16]

Surface-enhanced Raman scattering (SERS) is one of the most important applications of plasmonic nanostructures, in which normally weak Raman signals can be amplified by many orders of magnitude (as high as 10^8 - 10^{14}) near a nanoparticle surface, allowing ultrasensitive trace analysis and single-molecule detection.^[17-20] SERS can provide unique rotational/vibrational information of a molecule, for the purpose of fingerprinting. Therefore, SERS does not just infer the existence of a molecule through spectral signals, but can be used to identify its structure based on the spectroscopic fingerprint. For these reasons, SERS is considered as a direct and sensitive technique, and its use in biomedical sensing and imaging has been actively explored over the past decades.^[21-23]

The enormous enhancement of Raman signals in SERS strongly depends on the magnitude of near fields originating from the LSPR.^[24-26] These near fields can be optimized by careful tuning the LSPR peak to ensure maximal overlap with the exciting laser, and by using SERS-active substrates based on plasmonic nanostructures that generate enhanced E-fields. Silver nanostructures are especially attractive for SERS due to its large enhancement of near fields, and the enhancement can be an order of magnitude greater than what is possible with similar Au nanostructures.^[24] The signal enhancement provided by Ag nanostructures is most

pronounced when the LSPR is excited by the incident light under a resonant condition. As a result, there is a strong desire to synthesize Ag nanostructures with tunable LSPR properties.

In recent years, plasmonic nanostructures, especially those of Au, provide a versatile, multifaceted platform for a broad range of biomedical applications.^[4] Recent studies have validated their use in a number of techniques for both cancer diagnosis and therapies. For example, they can function as contrast agents for a number of optical imaging modalities; they can act as carriers for the delivery and controlled release of drugs; and they can serve as transducers for the photothermal destruction of tumor cells. For *in vivo* applications, especially when optical excitation or transduction is involved, the LSPR peaks of the nanostructures have to be tuned to the transparent window of soft tissues in the NIR region (from 700-900 nm) in order to maximize the penetration depth. In this so-called transparent window, light can penetrate deeply into soft tissues due to a great reduction in absorption from hemoglobin and water in the blood and in scattering by the tissue.^[27] For this reason, much research has focused on tuning the LSPR peaks of plasmonic nanostructures to wavelengths in the NIR region. For conventional Au colloids with a solid structure and a spherical shape, their LSPR peaks are typically limited to the visible region ranging from 500-600 nm. Only those Au nanostructures with nonspherical morphologies (e.g., rod, rice, multipod, and star) or a hollow structure (e.g., shell, box, and cage) can have LSPR peaks in the NIR region.^[4] While nanostructures made of other metals can also exhibit strong LSPR, the non-reactive and relatively bio-inert nature of Au makes this metal the most prominent candidate for both *in vitro* and *in*

vivo applications.

One novel class of nanostructures with tunable LSPR peaks in the NIR region is AuNCs, invented and developed by our group.^[28] These versatile nanostructures are characterized by hollow interiors, ultrathin and porous walls, and can be prepared using a remarkably simple procedure based on the galvanic replacement between Ag nanocubes and aqueous chloroauric acid.^[29] Figure 1.2, A and B, shows scanning electron microscopy (SEM) images of Ag nanocubes and the resultant AuNCs, respectively, and the insets display their corresponding transmission electron microscopy (TEM) images. The LSPR peaks of AuNCs can be readily and precisely tuned to any wavelength in the NIR region by controlling their size and/or wall thickness. Gold nanocages possess many unique features that make them particularly intriguing materials for biomedical applications: *i*) they are single crystals with good mechanical flexibility and stability, as well as atomically flat surfaces; *ii*) they can be routinely produced in large quantities with wall thicknesses tunable in the range of 2-10 nm with an accuracy of 0.5 nm; *iii*) their LSPR peaks can be easily and precisely tuned to any wavelength of interest in the range of 600-1200 nm by simply controlling the amount of H₂AuCl₄ added into the reaction, as shown in Figure 1.2C; *iv*) their hollow interiors can be used for encapsulation, and their porous walls can be used for drug delivery, with the release being controlled by various stimuli; *v*) their sizes can be readily varied from 20 to 500 nm to optimize biodistribution, facilitate particle permeation through epithelial tissues, or increasing drug loading; *vi*) their LSPR peaks can be dominated by absorption or scattering to adapt to different imaging modalities. Because of all of these attributes that AuNCs can provide, they

have been investigated for a broad range of biomedical applications:^[30,31] *i*) as tracers for tracking by multi-photon luminescence imaging; *ii*) as contrast agents for photoacoustic (PA) and multimodal imaging; *iii*) as photothermal agents for the selective destruction of cancerous tissue; and *iv*) as drug delivery vehicles for controlled and localized release.

1.3. Scope of This work

This work will be organized into three main sections: *i*) development of novel dimeric nanostructures of Ag for SERS applications; *ii*) *in vivo* quantitative evaluation of the transport kinetics of AuNCs in a lymphatic system by noninvasive PA tomography; *iii*) development of AuNCs as a new platform for controlled drug release with high-intensity focused ultrasound (HIFU).

In Chapter 2, I focus on the synthesis and SERS applications of well-defined dimers consisting of Ag nanospheres with a broad range of sizes. Two methods were developed for generating the Ag dimers. The first one was based on the polyol process, in which the growth of single-crystal Ag nanospheres and their dimerization occurred at the same time by adding a small amount of NaCl into the reaction solution.^[32] During the reaction, single-crystal Ag nanoparticles were formed as a result of oxidative etching, and the particle dimerization happened due to a change to colloidal stability. The second method was based on etching of Ag nanocubes with $\text{Fe}(\text{NO}_3)_3$.^[33] During the etching process, the corners and edges of the Ag nanocubes were truncated off to generate spherical particles, accompanied by dimerization because of the addition of ionic species. I further compared the SERS properties of

the dimers of Ag nanospheres with various sizes to achieve a systematic study of the hot-spot phenomenon in SERS. By correlating with SEM imaging, the SERS enhancement factors (EFs) of the dimers were calculated. Finally, I investigated the application of using these dimers as SERS tags for Raman mapping of cancer cells.

Chapter 3 systematically investigates the use of AuNCs as a novel class of optical tracers for noninvasive sentinel lymph node (SLN) mapping by PA imaging on a rat model.^[34] The transport and uptake of AuNCs in the lymphatic system were evaluated by PA imaging on the axillary region of a rat. Quantification of the amount of AuNCs accumulated in the lymph nodes was achieved by correlating the data from PA imaging with the results from inductively-coupled plasma mass spectrometry (ICP-MS). Several experimental parameters, including the injection concentration, particle size, and surface charge were systematically studied.

Chapter 4 demonstrates two temperature-regulated release systems by combining the unique features of AuNCs with HIFU. In the first system, I functionalized the surface of AuNCs with smart, thermally-responsive polymers.^[35] When a significant amount of acoustic energy is delivered to the focus using HIFU, the polymer chains will collapse as the temperature increases beyond a certain point, opening the pores and thus releasing the pre-loaded effectors. The second system simply involves filling the hollow interiors of AuNCs with a phase-change material (PCM).^[36] When exposed to HIFU, the PCM will melt when the temperature is above its melting point, and escape from the interiors of nanocages, concurrently releasing the molecules encapsulated in the PCM. The released dosage could be remotely controlled by manipulating the power of HIFU and/or the duration of exposure. The two controlled

release systems can also be further developed into a theranostic system with an array of functions, including the capabilities for *in vivo* molecular imaging, as well as chemo- and photothermal therapy.

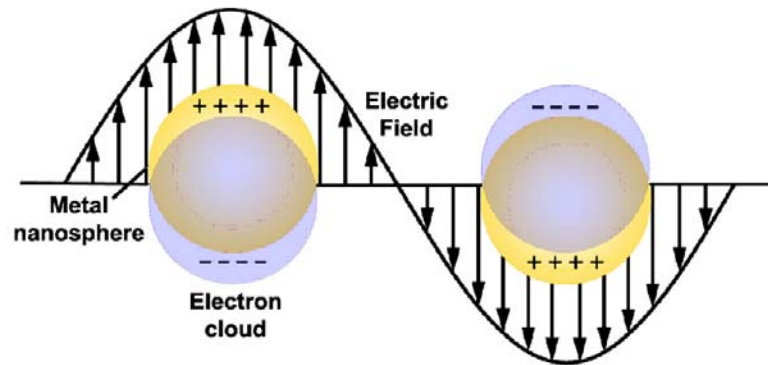


Figure 1.1. Schematic illustration of the LSPR phenomenon of a metal nanosphere, showing that the free electrons in the metal nanosphere can be displaced from the lattice of positive ions and collectively oscillate in resonance with the incident light.

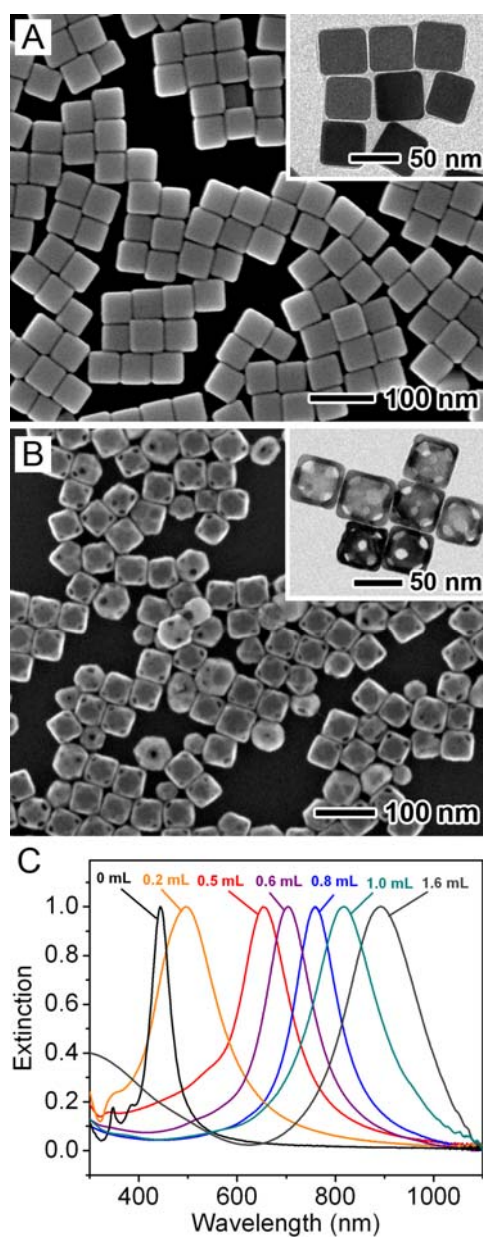


Figure 1.2. SEM images of (A) Ag nanocubes and (B) Au nanocages. The inset shows the corresponding TEM images of the same sample. (C) UV-vis spectra of the samples obtained by titrating an aqueous suspension of Ag nanocubes with different volumes of 0.1 mM aqueous H₂AuCl₄ solution.

1.4. References for Chapter 1

- [1] Gramotnev, D. K.; Bozhevolnyi, S. I. *Nat. Photonics* **2010**, *4*, 83.
- [2] Schuller, J. A.; Barnard, E. S.; Cai, W.; Jun, Y. C.; White, J. S.; Brongersma, M. L. *Nat. Mater.* **2010**, *9*, 193.
- [3] Kreibig, U.; Vollmer, M. *Optical Properties of Metal Clusters*; Springer Series in Material Science 25; Springer: Berlin, 1995.
- [4] Cobley, C. M.; Chen, J.; Cho, E. C.; Wang, L. V.; Xia, Y. *Chem. Soc. Rev.* **2011**, *40*, 44.
- [5] Stiles, P. L.; Dieringer, J. A.; Shah, N. C.; Van Duyne, R. P. *Annu. Rev. Anal. Chem.* **2008**, *1*, 601.
- [6] El-Sayed, M. A. *Acc. Chem. Res.* **2001**, *34*, 257.
- [7] Kelly, K.; Coronado, E.; Zhao L.; Schatz, G. C. *J. Phys. Chem. B* **2003**, *107*, 668.
- [8] Ghosh, S. K.; Nath, S.; Kundu, S.; Esumi, K.; Pal, T. *J. Phys. Chem. B* **2004**, *108*, 13963.
- [9] Storhoff, J. J.; Lazarides, A. A.; Mucic, R. C.; Mirkin, C. A.; Letsinger, R. L.; Schatz, G. C. *J. Am. Chem. Soc.* **2000**, *122*, 4640.
- [10] Wiley, B. J.; Im, S. H.; Li, Z.-Y.; McLellan, J.; Siekkinen A. R.; Xia, Y. *J. Phys. Chem. B* **2006**, *110*, 15666.
- [11] Pyayt, A. L.; Wiley, B.; Xia, Y.; Chen, A.; Dalton, L. *Nat. Nanotechnol.* **2008**, *3*, 660.
- [12] Peng, S.; Lee, Y.; Wang, C.; Yin, H.; Dai, S.; Sun, S. *Nano Res.* **2008**, *1*, 229.
- [13] Murphy, C. J.; Gole, A. M.; Hunyadi, S. E.; Stone, J. W.; Sisco, P. N.; Alkilany, A.; Kinard, B. E.; Hankins, P. *Chem. Commun.* **2008**, 544.

- [14] Murphy, C. J.; Gole, A. M.; Stone, J. W.; Sisco, P. N.; Alkilany, A. M.; Goldsmith, E. C.; Baxter, S. C. *Acc. Chem. Res.* **2008**, *41*, 1721.
- [15] Cao, Y. C.; Jin, R.; Mirkin, C. A. *Science* **2002**, *297*, 1536.
- [16] Mulvihill, M. J.; Ling, X.; Henzie, J.; Yang, P. *J. Am. Chem. Soc.* **2010**, *132*, 268.
- [17] Blackie, E. J.; Ru, E. C. L.; Etchegoin, P. G. *J. Am. Chem. Soc.* **2009**, *131*, 14466.
- [18] Nie, S.; Emory, S. R. *Science* **1997**, *275*, 1102.
- [19] Dieringer, J. A.; Lettan, R. B.; Scheidt, K. A.; Van Duyne, R. P. *J. Am. Chem. Soc.* **2007**, *129*, 16249.
- [20] Camden, J. P.; Dieringer, J. A.; Wang, Y.; Masiello, D. J.; Marks, L. D.; Schatz, G. C.; Van Duyne, R. P. *J. Am. Chem. Soc.* **2008**, *130*, 12616.
- [21] Banholzer, M. J.; Millstone, J. E.; Qin, L.; Mirkin, C. A. *Chem. Soc. Rev.* **2008**, *37*, 885.
- [22] Kneipp, J.; Kneipp, H.; Kneipp, K. *Chem. Soc. Rev.* **2008**, *37*, 1052.
- [23] Qian, X.-M.; Nie, S. M. *Chem. Soc. Rev.* **2008**, *37*, 912.
- [24] Haynes, C. L.; McFarland, A. D.; Van Duyne, R. P. *Anal. Chem.* **2005**, *77*, 338A.
- [25] Moskovits, M. *J. Raman Spectrosc.* **2005**, *36*, 485.
- [26] Le Ru, E. C.; Etchegoin, P. G. *Chem. Phys. Lett.* **2006**, *423*, 63.
- [27] Weissleder, R. *Nat. Biotech.* **2001**, *19*, 316.
- [28] Sun, Y.; Mayers, B. T.; Xia, Y. *Nano Lett.* **2002**, *2*, 481.
- [29] Sun, Y.; Xia, Y. *J. Am. Chem. Soc.* **2004**, *126*, 3892.
- [30] Skrabalak, S. E.; Chen, J.; Sun, Y.; Lu, X.; Au, L.; Cobley, C.; Xia, Y. *Acc. Chem. Res.* **2008**, *41*, 1587.
- [31] Xia, Y.; Li, W.; Cobley, C. M.; Chen, J.; Xia, X.; Zhang, Q.; Yang, M.; Cho, E.

- C.; Brown, K. P. *Acc. Chem. Res.* **2011**, DOI: 10.1021/ar200061q.
- [32] Li, W.; Camargo, P. H. C.; Lu, X.; Xia, Y. *Nano Letters* **2009**, *9*, 485.
- [33] Li, W.; Camargo, P. H. C.; Au, L.; Zhang, Q.; Rycenga, M.; Xia, Y. *Angew. Chem. Int. Ed.* **2010**, *49*, 164.
- [34] Cai, X.; Li, W.; Kim, C.; Yuan, Y.; Wang, L. V.; Xia, Y. *ACS Nano* **2011**, submitted.
- [35] Li, W.; Cai, X.; Kim, C.; Sun, G.; Zhang, Y.; Deng, R.; Yang, M.; Chen, J.; Achilefu, S.; Wang, L. V.; Xia, Y. *Nanoscale* **2011**, *3*, 1724.
- [36] Moon, G. D.; Choi, S. -W.; Cai, X.; Li, W.; Cho, E. C.; Jeong, U.; Wang, L. V.; Xia, Y. *J. Am. Chem. Soc.* **2011**, *133*, 4762.

Chapter 2

Novel Dimeric Nanostructures of Silver for Surface-Enhanced Raman Scattering (SERS) Applications

2.1. Introduction

Silver nanostructures have attracted considerable interests because of their spectacular property known as localized surface plasmon resonance (LSPR), which has enabled their widespread use as optical probes, contrast agents, sensors, plasmonic waveguides, and substrates for SERS.^[1-5] Among various applications of Ag nanostructures, SERS has particularly been of great interest due to its application in ultrasensitive trace analysis and single-molecule detection as it has been demonstrated with samples fabricated from Ag nanoparticles via salt-induced aggregation.^[6,7] For these substrates, it is generally accepted that single-molecule sensitivity can only be achieved at the specific site known as hot spot -- the gap region of a pair of strongly coupled Ag (or Au) nanoparticles, where the electromagnetic field can be drastically amplified, leading to the observation of enhancement factors (EFs) several orders in magnitude greater than those of the individual nanoparticles.^[8-10]

Although the hot spot phenomenon has been extensively investigated from both theoretical and experimental perspectives, it remains an elusive, feebly understood subject. One of the most commonly used methods for generating hot spots is based on the salt-induced, random aggregation of Ag or Au colloidal particles in a solution

phase.^[11,12] In addition to the poor reproducibility in terms of inter-particle spacing and number of particles that is characteristic of a random aggregation process, the constituent nanoparticles are also troubled by irregularity and non-uniformity in terms of size, shape, crystallinity, and overall morphology. As a result, it has been hard (if impossible) to correlate the observed giant EF to the specific attribute(s) of a hot spot. In an attempt to address this issue, many research groups have developed various methods for controlling the assembly of Ag or Au nanoparticles into well-defined structures for SERS applications.^[13-16] Most of these studies were, however, based on functionalization of the surface of nanoparticles with organic or biological molecules.^[17-21] In general, the procedures for producing a dimeric structure through surface modification are rather complicated, usually involving a number of steps. On the other hand, the resultant dimers are limited in use for SERS applications because the biological or organic linkers that bridge the two nanoparticles tend to prevent the analyte molecules from entering the hot spot. As a result, it still remains a grand challenge in assembling Ag or Au nanoparticles into dimers with well-defined hot spots for SERS.

During the past decade, SERS has been used as an effective technique in many analytical systems, including environmental monitoring,^[22] heterogeneous catalytic reaction monitoring,^[23] chemical warfare-stimulant detection,^[24] and explosive-agent detection.^[25] In recent years, SERS has attracted much attention in biomedical applications, and has been developed as a viable and novel imaging technique for cellular/tissue imaging and tumor detection.^[26-29] SERS imaging takes advantage of the high intensities of SERS signals and the rich chemical information contained in a

SERS spectrum to generate images of metal nanoparticle distributions.^[26,29,30-33]

SERS imaging effectively locates the nanoparticles over a scanned region, and the presence of nanoparticles can be used to infer the presence of a desired target. Typically, the metal nanoparticle (usually Ag or Au) is derivatized with Raman probe molecules and coated with a shell made of SiO₂ or polymer to generate the so-called SERS tag. The probe molecule provides a unique SERS signal, while the shell protects the Raman probes and allows further conjugation with targeting ligands, such as monoclonal antibodies, peptides, or small molecules, to target cells and tissue with high specificity.

The main benefits of SERS imaging lie in its multiplexing capabilities and sensitivity.^[32-35] *i)* many unique SERS probes can be fabricated by simply changing the probe molecules attached to the surface of metal nanoparticles; *ii)* compared with fluorescence bands, the SERS vibrational bands are much narrower, allowing for easier and more accurate data analysis and image construction; *iii)* unlike quantum dots and fluorescence molecules, only a single excitation source is needed to generate the SERS signals from numerous different probe molecules, and the excitation can be conveniently tuned to the transparent window of soft tissues in the NIR region.

In this chapter, I will discuss the synthetic methods for generating well-defined dimers consisting of Ag nanospheres and the feasibility to employ these novel dimeric nanostructures for ultrasensitive detection and imaging through SERS. First, in Section 2.2, I will discuss the synthesis of dimers of Ag nanospheres with a range of sizes by using two methods. The first method is based on polyol synthesis and the second is based on wet etching. I have found that the key for the dimerization process

is to control the colloidal stability by adding appropriate amount of ionic species. In Section 2.3, I will discuss the SERS properties of the dimers of Ag nanospheres with various sizes. By correlating with SEM imaging, I have measured and compared the SERS EFs for individual dimers with different sizes. Finally, in Section 2.4, I will discuss the feasibility of using the dimers of Ag nanospheres as SERS tags for imaging cancer cells.

2.2. Syntheses of Dimers of Silver Nanospheres

I developed two methods for synthesizing dimers made of Ag nanospheres by manipulating the colloidal stability with the addition of ionic species into a suspension.^[36,37] Spherical particles will give additional benefit for the study of hot spot due to their simplicity for computational simulation. I focus on Ag instead of Au because Ag has been shown to outperform Au by at least ten folds in terms of SERS sensitivity.^[38]

2.2.1. Dimerization Based on the Polyol Process

The first method for generating the Ag dimers is based on the polyol process,^[39] in which a polyol (a molecule containing multiple hydroxyl groups) such as ethylene glycol (EG) serves as both a solvent and a precursor to the reducing agent. In a typical synthesis, a capping agent, poly(vinyl pyrrolidone) (PVP), and a Ag precursor, AgNO₃, were injected into pre-heated EG, and the reduction of Ag⁺ ions resulted in the nucleation and growth of Ag nanostructures. By introducing a small amount of NaCl into the reaction solution, I obtained single-crystal Ag nanoparticles as a result

of oxidative etching, and at the same time dimerization due to a reduction of the colloidal stability.

Figure 2.1A shows a typical TEM image of the dimers of Ag nanospheres obtained at 20.5 h into the reaction, with the addition of 90 μ L NaCl/EG solution into the mixture. Black circles were drawn to highlight the dimers. Counting over 150 Ag nanoparticles, I found that \sim 58% of them had dimerized during the synthesis (the percentage of dimerization is defined as the number of dimerized spheres divided by the total number of spheres). To confirm that the dimers were formed in the reaction solution rather than during TEM sample preparation, I added tetraethylorthosilicate (TEOS) to the reaction mixture to fix the dimers via silica coating. Figure 2.1B shows a TEM image of the SiO₂-coated sample. Many dimers can be easily identified in this sample, clearly demonstrating the presence of dimers in the reaction solution. The clear contrast between the core and shell indicates that the SiO₂ coating had a uniform thickness of \sim 7 nm over the entire surface of the dimer.

A magnified TEM image of an individual dimer (Figure 2.1C) shows a spherical shape for the two Ag nanoparticles that were 30.0 and 31.7 nm in diameter. There is a narrow gap of 1.8 nm wide between the two nanospheres, forming the so-called hot spot. The Ag nanospheres obtained using this protocol were actually truncated octahedrons (or cuboctahedrons) with a rounded profile (see the inset of Figure 2.1C), which are enclosed by a mix of (111) and (100) facets.^[40] The uniform contrast across each particle indicates that the Ag nanospheres were single crystalline, which is also supported by the high-resolution TEM image (Figure 2.1D). Each sphere displayed a periodic fringe with an inter-planar spacing of 0.24 nm, a value that is consistent with

the separation between the $\{111\}$ lattice planes. As labeled in the same Figure, the top sphere interacted with the bottom sphere through one of its (111) facets. In a truncated octahedron, the angle between adjacent $\{111\}$ facets is 73.2° , indicating that the facet used by the bottom sphere to interact with the top sphere was also (111). All these results are supported by previous observations, where PVP was found to interact more strongly with the $\{100\}$ than $\{111\}$ facets,^[41] and thus preferentially adsorb on the $\{100\}$ facets. When two Ag nanospheres approached each other, it is not unreasonable to expect that they would prefer to interact through the $\{111\}$ rather than $\{100\}$ facets.

To further understand and monitor the evolution of dimers, I took samples at various stages of the reaction as guided by the distinctive color changes. Within the first minute of reaction, the solution turned into light yellow, indicating the formation of Ag nanoparticles due to polyol reduction. The yellow color kept increasing in intensity and maintained its appearance for another 20 min. Our group's previous experiments showed that most of the particles had a twinned structure at this time.^[39] As the reaction proceeded, the yellow color started to fade and became colorless after ca. 1 h due to oxidative etching of the twinned nanoparticles in the solution. The solution remained colorless for a long period of time until a light yellow color appeared again at ca. 19 h into the synthesis. Note that the time at which the reaction mixture became light yellow again could vary for different syntheses, so the state of the reaction should be identified from the color change rather than a specific time. Figure 2.2A shows a TEM image of the sample when the reaction mixture turned into light yellow again after oxidative etching. The inset in Figure 2.2A gives a TEM

image at a higher magnification. It is clear that the sample at this point contained many dimers, but the nanospheres in the dimers were very small, with their diameters being in the range of 8-10 nm. When the reaction was continued, the color of the reaction mixture became darker. Figure 2.2B shows a TEM image of particles sampled 1.5 h later when the reaction mixture exhibited a bright yellow color with a slight orange tint. Compared to the sample shown in Figure 2.2A, the Ag nanospheres increased to ~30 nm in diameter as shown by the magnified TEM image (inset of Figure 2.2B). As the reaction was continued for another 0.5 h, the solution became dark orange-yellow with a slight red-brown tint. From the TEM images (Figure 2.2C), it can be seen that the Ag particles grew a little bigger and their shape became more or less cubic, not as spherical as those shown in Figure 2.2B. In addition, I found that instead of approaching each other through the {111} facets as shown in Figure 2.1C, the Ag nanoparticles with a cubic shape could also interact with each other through their {100} facets. This is because the particles had evolved into cubes with only slight truncation at corners and thus mainly enclosed by {100} facets due to the preferential stabilization of these facets by PVP. This observation suggests that the two Ag nanoparticles in the dimer could freely rotate in space during the synthesis, reflecting the dynamic aspect of the dimeric structure.

Figure 2.2D shows UV-vis spectra taken from samples at these three different reaction stages, corresponding to the products shown in Figure 2.2, A-C, respectively (the inset in Figure 2.2D shows photographs of these samples dispersed in ethanol). Note that the LSPR peak at 400 nm associated with the Ag nanoparticles gradually increased in intensity as the reaction proceeded. It is worth noting that a shoulder

peak appeared in the range of 450 to 550 nm for samples in Figure 2.2, B and C, which could be attributed to dimerization. It is worth pointing out that spectrum-b agrees well with the extinction spectrum calculated for dimers of Ag nanospheres,^[42] further confirming the formation of dimers in the reaction solution. Additionally, there was a slight red-shift for the main peak as the reaction proceeded, which could be ascribed to the growth of particle size.

I found that the yield of the dimers was sensitive to the concentration of NaCl in the reaction mixture. Figure 2.3A shows a TEM image of the sample when a smaller amount (66 rather than 90 μL) of NaCl/EG solution was added to the reaction. In this case, both single-crystal and multiply twinned nanoparticles were formed, but there was essentially no dimer in the sample. This observation can be explained by the oxidative etching scheme outlined in the previous studies.^[43] According to this scheme, a combination of oxygen from air and a ligand for the metal ion (such as chloride for Ag^+) in the reaction solution can result in a powerful etchant for both the nuclei and seeds. In the presence of sufficient chloride, the defects inherently present on twinned particles will provide more reactive sites for oxidative dissolution, while single-crystal seeds are more resistant to oxidative etching as there are no twin boundary defects on the surface. As clearly shown in Figure 2.3A, both single-crystal and twinned particles were formed when not enough NaCl was added. In contrast, when a larger amount (114 μL) of the NaCl/EG solution was added to the reaction, dimers of single-crystal Ag nanospheres could also be produced, as shown in Figure 2.3B. However, it is clear that the yield of dimers was much lower than the sample shown in Figure 2.1 and larger aggregates could be easily found in the sample. The

higher degree of agglomeration can be attributed to the higher concentration of NaCl in the reaction mixture.

We can use the DLVO theory to explain the formation of dimers and the dependence of yield on the concentration of NaCl. The DLVO theory, which was proposed by four renowned scientists Derjaguin, Landau, Verwey, and Overbeek during the 1940s, provides a framework for colloidal interactions and colloidal stability (the theory became known by the initial letters of their names: DLVO). In the DLVO theory, colloidal stability is determined by a balance between the short-range double-layer repulsion and long-range van der Waals attraction.^[44] As two particles approach each other, a repulsive barrier appears due to the electrostatic repulsion between the double layers. When the repulsive barrier is greater than $10k_B T$, where k_B is the Boltzmann constant and T is the temperature, the collisions derived from Brownian motion will be unable to overcome the barrier and thus there is no agglomeration. However, when the repulsive barrier is reduced to the scale below $10k_B T$, it is highly possible that dimerization, as well as higher degrees of aggregation, will occur in the suspension as a result of the constant collisions between colloidal particles derived from Brownian motion. In the diffusive double layer, the repulsive electrostatic potential V_R can be expressed by the following equation.^[44]

$$V_R(h) \propto \kappa^{-1} e^{-\kappa h} \quad (2.1)$$

where h is the separation distance between two particles, and κ is the inverse Debye length. In general, κ is given by

$$\kappa = (\text{F}^2 \sum_i c_i z_i^2 / \epsilon_0 \epsilon \text{RT})^{1/2} \quad (2.2)$$

where F is the Faraday constant, ϵ_0 is the permittivity of vacuum, ϵ is the dielectric constant of the dispersion medium, R is the ideal gas constant, and c_i and z_i are the concentration and valence of each ionic species i . Based on equation (2.2), the easiest way to control κ is to vary the concentration and nature of the electrolytes or ionic species. An increase in the electrolyte concentration c_i will result in a decrease repulsive electrostatic potential V_R , causing an unstability for the colloidal system, thus inducing dimerization and higher degrees of aggregation for the colloidal particles. In order to optimize the yield of dimers, one has to control the concentration of NaCl in the medium region, not too low or too high.

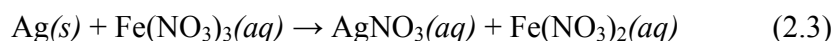
2.2.2. Dimerization Based on the Etching Process

As a disadvantage for the polyol growth-based method for generating the dimers I developed in Section 2.2.1, I could not extend it to produce dimers of Ag spheres larger than 30 nm, because further growth will lead to transformation of the spheres into cubic particles. As shown in Figure 2.2C, when the reaction was extended to a longer time, the shapes of the Ag particles became more or less cubic. It will be a great advantage to have dimers made of Ag nanospheres with a broad range of sizes for SERS studies due to the simplicity of spherical particles for computational simulation.

Our group has developed a number of protocols for producing Ag nanocubes, and their edge lengths could be controlled from 30 to 200 nm by adjusting the reaction parameters.^[45-47] Starting from a uniform sample of Ag nanocubes, I demonstrated a facile method based upon wet etching with $\text{Fe}(\text{NO}_3)_3$ for generating well-defined

dimers of Ag nanospheres with a wide range of sizes. The etching reaction was performed at room temperature in ethanol with the help of PVP. When an aqueous suspension of Ag nanocubes was mixed with a small amount of aqueous $\text{Fe}(\text{NO}_3)_3$ solution in ethanol, the corners and edges of the cubes were truncated off to form spheres, which were also induced to dimerize at the same time. This approach was demonstrated to work well for Ag cubes having edge lengths in the range of 40-100 nm.

Figure 2.4 schematically illustrates the procedure I used for fabricating the dimers. I started with Ag nanocubes dispersed in a mixture of ethanol (majority) and water. Aqueous $\text{Fe}(\text{NO}_3)_3$ solution can be used as a powerful wet etchant to dissolve Ag,^[48] and the reaction can be described as the following:



As I discussed in the last section, the stability of a colloidal system is dependent on the concentrations of electrolytes or ionic species in the medium, which can be explained by the DLVO theory. An increase in the electrolyte concentration will reduce the stability of a colloidal system. Therefore, when a small amount of aqueous $\text{Fe}(\text{NO}_3)_3$ solution was added into an ethanol suspension of Ag nanocubes, the salt not only served as an etchant for the Ag cubes but also triggered the resultant Ag spheres to dimerize at the same time.

Figure 2.5, A and B, shows typical SEM and TEM images of the Ag nanosphere dimers prepared from Ag nanocubes of ~100 nm in edge length. White and black ellipses were drawn to highlight the dimers in the SEM and TEM images, respectively. It can be seen that a large number of dimers were distributed over a wide

area on the substrate, indicating that a significant proportion of the particles in the final product existed in the well-defined dimeric structure. Counting over 150 Ag nanoparticles on the SEM or TEM images, I found that the percentage of dimerization was ~66%. The insets in Figure 2.5, A and B, show magnified SEM and TEM images of the dimers, implying that the dimers had a smooth surface. The magnified TEM image of an individual dimer clearly shows a spherical shape for the two constituent Ag spheres that were 79.4 and 81.1 nm in diameter, respectively. Because the cubes we used for the etching process were single crystals, the resulting nanospheres in the dimers were also single crystals, as confirmed by the uniform contrast across the particle under TEM. This is further supported by the HRTEM image shown in Figure 2.5C. There was a narrow gap of ~0.67 nm wide between the two nanospheres, forming the so-called hot spot. Figure 2.5D shows a TEM image of the sample after SiO₂ coating. Again, a large number of dimers can be easily identified in this sample, demonstrating that the dimers were formed in the reaction solution rather than on the substrate during SEM or TEM sample preparation. The inset in Figure 2.5D shows a magnified TEM image of an individual SiO₂-coated dimer. The strong contrast difference between Ag and SiO₂ suggests that the SiO₂ coating had a more or less uniform thickness of ~11.6 nm over the entire surface of the dimer.

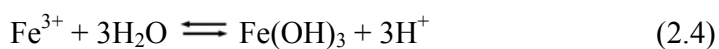
This etching method of preparing dimers can be extended to Ag nanospheres with a range of different sizes by employing Ag nanocubes of different edge lengths as precursors. Figure 2.6, A and B, shows typical SEM and TEM images of Ag dimers of nanospheres derived from Ag cubes ~82 nm in edge length. Figure 2.6, C and D, shows SEM and TEM images of dimers fabricated from Ag cubes ~47 nm in edge

length. Similar to the sample shown in Figure 2.5, a large number of dimers can be easily identified from the SEM and TEM images, as highlighted again by white and black ellipses. The inset in each image shows a magnified SEM or TEM image of the sample, indicating that all of the spheres had a smooth surface and exhibited a round profile. The dimers derived from 82- and 47-nm Ag cubes were consisted of single-crystal spheres approximately 63 and 40 nm in diameter, respectively. Table 2.1 provides a summary of the major parameters for the different samples. It can be seen that the as-prepared samples all had relatively high percentages of dimerization (>60%), and the gap widths of the dimers all fell into a narrow range of 0.6-0.7 nm.

Figure 2.7 shows the SEM images of the Ag nanocubes with average edge lengths of 100 nm, 82 nm, and 47 nm, respectively. Figure 2.8 shows the UV-vis extinction spectra of the cube precursors and the resulting dimers. Four LSPR peaks were present for both the 100- and 82-nm cubes, while three peaks can be resolved for the 47-nm cubes. These observations are consistent with the characteristic dipole and quadrupole resonances for Ag nanocubes of these sizes.^[44] After wet etching and dimerization, the primary LSPR peak of the samples all blue-shifted because of the reduction in size as compared to the corresponding cube precursors. The two peaks located at 350 and 390 nm disappeared due to higher symmetry of a sphere than a cube. It is worth noting that a shoulder peak appeared at ~500 nm (just next to the primary LSPR peak) for the 40-nm Ag sphere dimers, indicative of dimerization. This is consistent with the LSPR study on dimers consisting of 30-nm Ag spheres described in the previous section. However, the existence of a shoulder peak that implies dimerization could not be resolved from the spectra of dimers made of 80-

and 63-nm spheres. This can probably be attributed to the broad LSPR peaks for Ag spheres of such large sizes, which could overshadow the shoulder peaks characteristic of dimers.

The etching process for generating the Ag dimers was typically performed in a medium containing a large amount of ethanol, a small quantity of water, and a certain amount of PVP. Both PVP and ethanol played an important role in the dimerization process. I found that the etching reaction could not proceed without the addition of PVP. Figure 2.9 shows SEM image of the product obtained under the same experimental condition as that for the sample shown in Figure 2.5 except that no PVP was added. In this case, the resulting product exhibited a cubic shape instead of the spherical morphology, and no dimers could be found. Compared to the precursor cubes, the surface of the cubes shown in Figure 2.9A was much rougher and there was an obvious coating deposited on the surface. When the reaction time was extended to 18 h, more coating was found on the surface of the cubes and there was still no dimers (Figure 2.9B), indicating that the etching process was essentially blocked by the coated material. Energy-dispersive X-ray (EDX) analysis was performed in order to identify the composition of the coating on the surface of the nanocubes. Figure 2.9C displays the EDX spectrum taken from the 18-h sample. In addition to the peak for Si from the substrate and the peak for Ag from the cubes, we also detected the peak for Fe. It is known that Fe(III) ions tend to undergo hydrolysis in an aqueous solution to form iron hydroxide, Fe(OH)₃, and the reaction can be described as the following:



Even though the etching process was performed in a medium largely made of ethanol, a small amount of water was introduced into the system when we added the aqueous $\text{Fe}(\text{NO}_3)_3$ solution (40 or 50 μL) and the aqueous suspension of Ag nanocubes (20 μL) into the reaction system. Therefore, formation of $\text{Fe}(\text{OH})_3$ during the etching process would be inevitable. Meanwhile, $\text{Fe}(\text{OH})_3$ has long been known as a good adsorbent, and is widely used in water purification for entrapping and removing contaminants. Therefore, it can easily adsorb onto the surface of Ag nanocubes. As I discussed in the previous section, PVP was found to strongly interact with the surface of Ag nanoparticles, with a preferential adsorption on the $\{100\}$ facets.^[39] Since the surface of the cubes were all covered by $\{100\}$ facets, it is possible that PVP could prevent the adsorption of $\text{Fe}(\text{OH})_3$ onto the surface of Ag cubes, thereby facilitating the etching process. In addition, ethanol was also found to be a key component for the successful preparation of the dimers. No dimers was found in our group's previous study when the etching was performed in water even with the addition of extra PVP.^[49] Some coating was still observed on the surface of the product prepared in water, which was most likely $\text{Fe}(\text{OH})_3$. This is because the hydrolysis of $\text{Fe}(\text{III})$ ions in water is much faster than it is in ethanol. It is not unexpected that more $\text{Fe}(\text{OH})_3$ would be formed when the reaction was performed in water, which subsequently impeded the formation of dimers.

2.3. SERS Properties of Dimers of Silver Nanospheres with Different Sizes

2.3.1. SERS of the Dimers Prepared Using the Polyol Process

I first performed correlated SERS/SEM measurements on the dimers of 30-nm Ag spheres prepared using the polyol method. In a typical procedure, the sample was prepared by drop-casting an ethanol suspension of the dimers on a Si substrate that had been patterned with registration marks and letting it dry under ambient conditions. Once the sample had dried, it was rinsed with copious amounts of ethanol, immersed in a 5 mM solution of 4-methyl-benzenethiol (4-MBT) in ethanol for 3 h, taken out, washed with copious amounts of ethanol, and finally dried under a stream of nitrogen. All samples were used immediately for SERS measurement after preparation.

Figure 2.10 shows SERS spectra taken from the sample that had been functionalized with 4-MBT. I used 4-MBT as the probe molecule because it is known to form a well-defined monolayer on the Ag surface with a characteristic molecular footprint, which is critical to estimate of the total number of molecules probed in the SERS measurement and thus calculation of the EF. In addition, the relatively small size of 4-MBT molecules makes it easier for them to get into the hot-spot region of the dimers. Owing to the relatively small size (~30 nm in diameter) of the Ag nanospheres, I expect that probe molecules outside the hot-spot region will not contribute to the detected SERS signals.^[50] Hence, these small dimers can provide an ideal model system for investigating the EF and polarization effect of an individual hot spot. The top trace in Figure 2.10A shows the SERS spectrum taken from a single dimer, with the laser polarization parallel to the longitudinal axis. The two characteristic peaks for 4-MBT at 1079 and 1594 cm^{-1} were clearly resolved, albeit at

low intensity. The peak at 1079 cm^{-1} is due to a combination of the phenyl ring-breathing mode, CH in-plane bending, and CS stretching, while the peak at 1594 cm^{-1} can be assigned to phenyl stretching (8a vibrational mode).^[51,52] The low intensity reflects the small number of molecules trapped in the hot-spot region and the relatively smaller Raman cross-section for the 4-MBT molecules as compared to organic dyes usually employed in single-molecule SERS studies.^[6,7] Figure 2.10 also gives the SERS spectra recorded from two Ag nanospheres separated by $\sim 600\text{ nm}$ (middle trace) and a single Ag nanosphere (bottom trace). In these two cases, there was no hot spot involved. In the case of two Ag nanospheres separated by 600 nm , both of them were within the laser focal volume ($\sim 10\text{ }\mu\text{m}$ in diameter), and the total number of probed 4-MBT molecules should be similar to the case of a dimer. The absence of detectable SERS signals confirm that only 4-MBT molecules trapped in the hot-spot region are responsible for the SERS peaks at 1079 and 1594 cm^{-1} .

I employed the peak at 1079 cm^{-1} to estimate the EF of the hot spot through the following equation:

$$EF = (I_{\text{sers}} \times N_{\text{bulk}}) / (I_{\text{bulk}} \times N_{\text{trap}}) \quad (2.5)$$

where I_{sers} and I_{bulk} are the intensities of the same band for the SERS and bulk spectra, N_{bulk} is the number of bulk molecules probed for a bulk sample, and N_{trap} is the number of molecules probed in the SERS spectrum. The areas of the 1079 cm^{-1} band were used for the intensities I_{sers} and I_{bulk} . I chose this band because it was the strongest band in the spectra. N_{bulk} was determined based on the ordinary Raman spectrum of a 0.1 M 4-MBT solution in $12\text{ M NaOH}_{(\text{aq})}$ and the focal volume of our Raman system (1.48 pL). When determining the number of trapped molecules

(N_{trap}) in the hot spot region, I assume that the 4-MBT molecules will be absorbed as a monolayer with a 0.19 nm^2 molecular footprint onto a spherical cap having $h = r/6.6$ located on each Ag nanosphere of the dimer (i.e., the inter-particle region), as shown in Figure 2.10B. This approximation was based on the TEM images shown in Figure 2.1, C and D, and yielded $N_{\text{trap}} = 2,510$. This number represents a theoretical maximum number of molecules, and is surely an overestimate, thus the EF reported here is likely an underestimate rather than an overestimate of the actual EF value. According to this approach, the EF of the hot spot was calculated to be 1.9×10^7 . Alternatively, if we assume that the hot spot region is enclosed by two hexagonal (111) faces (see the inset in Figure 2.2C), $N_{\text{trap}} = 1,904$ and the EF became 2.5×10^7 , which is also close to 1.9×10^7 . It is important to note that 4-MBT does not exhibit any absorption bands around 785 nm (the wavelength of the laser), which excludes the possibility of any resonance Raman effects for the excitation laser employed in our study. Further enhancement of the SERS effect can be achieved by employing probe molecules with resonance effects and/or by optimizing the laser wavelength employed in the measurements.

I also found that the SERS signals were highly dependent on the laser polarization. It can be observed that the 4-MBT peaks were maximized when the laser was polarized parallel to the longitudinal axis of the dimer. The 4-MBT signals were gradually reduced when the laser was rotated by 22.5 and 45 degrees away from the longitudinal axis. At 45 degrees, the area of the peak at 1079 cm^{-1} was reduced by a factor of ~ 3 . Finally, the 4-MBT peaks disappeared when the polarization was off from the longitudinal axis by angles larger than 45 degrees (e.g., 77 and 90 degrees).

2.3.2. SERS of the Dimers Prepared Using the Etching Process

Although the small dimers prepared using the polyol process provide useful information about the hot-spot phenomenon, the detected SERS signals were actually very weak due to the small size of the Ag spheres (~30 nm) and thus the small number of molecules trapped in the hot-spot region, suggesting the difficulty of dimers with such a small size for ultrasensitive detection. It will be a great advantage to have dimers made of Ag nanospheres with bigger of sizes for SERS studies. Therefore, I further performed SERS measurements on the dimers of Ag nanospheres with various sizes prepared using the etching process. Figure 2.11 shows the SERS spectra taken from a single dimer of 80-nm Ag spheres, with the laser polarization parallel (top trace) and perpendicular (middle trace) to the dimer's longitudinal axis. The bottom trace in Figure 2.11 gives the SERS spectrum recorded from an individual Ag nanosphere. The insets show the corresponding SEM images. The two strong peaks located at 1072 and 1583 cm^{-1} are the characteristic peaks for 4-MBT. The broad band shown in the middle and bottom trace at 900-1000 cm^{-1} comes from the Si substrate. In order to compare the SERS spectra recorded for the three different systems in one figure, I amplified the SERS signals by 10 times for the middle and bottom spectra in the plot. It is clear that the intensity of the characteristic 4-MBT SERS peaks decreased in the order of: *dimer (parallel)* \gg *dimer (perpendicular)* $>$ *single sphere*.

Table 2.2 summarizes the EFs for dimers of Ag nanospheres with three different sizes with the laser polarization parallel and perpendicular to the dimer's longitudinal

axis, as well as the corresponding individual spheres. The EF was calculated using Equation (2.5) described in Section 2.3.1, except replacing the N_{trap} with N_{SERS} . N_{SERS} is the number of molecules probed in the SERS spectrum, based upon the assumption that a monolayer of 4-MBT molecules was formed on the surface of Ag with 0.19 nm² molecular footprint. It can be seen that the EFs for the dimer decreased with decreasing size for the sphere. In addition, the EFs for dimers with laser polarization parallel to the dimer's longitudinal axis are all much higher than the corresponding ones with the polarization perpendicular to the dimer's longitudinal axis. This indicates that the SERS signals taken from the dimer were polarization dependent, which is consistent with our study on the dimers made of 30-nm Ag spheres. The strong dependence on laser polarization could be attributed to the difference in the electric field enhancements under different excitation directions.^[53] When comparing the EF of a dimer and that of a single sphere, we found that the EF of an individual sphere was much lower than that of the corresponding dimer, indicating the hot-spot phenomenon. Besides, the EF (1.7×10^8) for a dimer of 80-nm spheres with the laser polarization parallel to the dimer's longitudinal axis is almost 10 times higher than that of the dimer of 30-nm spheres.

2.4. Dimers of Silver Nanospheres as SERS Tags for Raman Imaging

In this section, I will discuss the feasibility of using dimers of Ag nanospheres as SERS tags for Raman imaging. The surface of the dimers of Ag nanospheres was first modified with Raman probe molecules, and then coated with a SiO₂ shell for protection. After that, anti-HER2 antibodies were immobilized on the SiO₂ shell. I

then incubated cancer cells that overexpress HER2 with the as-prepared SERS tags and used a Raman system to generate SERS images of these cancer cells. I also prepared SERS tags from Ag nanospheres and Ag nanocubes, and compared their properties with the tags fabricated from the Ag dimers.

2.4.1. Structural and Optical Characterization of the SERS Tags

Figure 2.12 shows typical TEM images and UV-vis extinction spectra of the three different SERS tags fabricated from the dimers of Ag nanospheres, Ag nanospheres, and Ag nanocubes. In the following discussion, they will be termed dimer-tags, sphere-tags, and cube-tags, respectively. The Ag particles of the three samples were all first functionalized with 4-mercaptopbenzoic acid (4-MBA), a Raman probe, and then coated with SiO₂. As shown in Figure 2.12, A-C, the diameter of the Ag spheres in the dimer, the diameter of the individual Ag spheres, as well as the edge length of the Ag cubes were all about 50 nm. The thicknesses of the SiO₂ coating of all three samples were also kept the same, ~15 nm, as indicated by the clear contrast difference between Ag and SiO₂. The UV-vis spectra (Figure 2.12, D-F) show that after surface modification (including both 4-MBA functionalization and SiO₂ coating), the LSPR peaks of the three samples (Ag dimers, spheres, and cubes) were all slightly red-shifted. In addition, the LSPR peak of the dimer-tags was more red-shifted, and much broader than that of the sphere-tags, indicating the dimerization of the particles.

2.4.2. Raman Characterization of the SERS Tags

Figure 2.13 shows the SERS spectra of individual SERS tags deposited on a glass

slide. The insets show SEM images of the corresponding SERS tags, from which the spectra were recorded. It can be observed that the two characteristic peaks for 4-MBA at 1080 and 1588 cm^{-1} were clearly resolved for the Ag dimer-tag,^[54] while the peak at 1080 cm^{-1} was barely detected for the sphere-tag and cube-tag due to the relatively weak enhancement. For a Ag dimer-tag, the SERS signals of 4-MBA were gradually reduced when the laser was rotated by 45° and 90° away from the longitudinal axis of the dimer. At 90°, the intensity of the peak at 1588 cm^{-1} was reduced by a factor of ~15 compared to that with laser polarization parallel to the dimer's longitudinal axis. In addition, the SERS signal recorded from a dimer-tag was obviously much stronger than that of a sphere-tag or cube-tag, indicating the efficient preservation of the hot spot in the dimer-tag. With respect to the cube-tag (Figure 2.13C), it can be seen that the intensity of the SERS signal with the laser polarization along a face diagonal of the cube was about two times stronger than that with laser polarization along an edge of the cube. Additionally, the SERS signal from the cube-tag was higher than that from the sphere-tag, mainly due to the sharp corners associated with the cube.

Furthermore, the SERS signals from aqueous suspensions of the Ag dimer-tags, sphere-tags, and cube-tags with the same particle concentration ($\sim 1.2 \times 10^{15}$ particles/L) were also compared. As shown in Figure 2.14, the intensity of the 4-MBA peaks from the suspension of the dimer-tags was about 14 times stronger than that from the sphere-tags and about 5 times stronger than that from the cube-tags.

I then employed the peak at 1588 cm^{-1} (the strongest band in the spectra) to estimate the SERS EFs of different SERS tags, as summarized in Table 2.3. It can be seen that the EF for a dimer-tag gradually decreased when the laser was rotated by

45° and 90° away from the longitudinal axis of the dimer. At 90°, the EF is about 6.5 times lower than that with laser polarization parallel to the dimer's longitudinal axis. When comparing the EF of a dimer-tag and that of a sphere-tag, we found that the EF of the dimer-tag (laser parallel to the dimer's longitudinal axis) was about 15 times higher than that of a sphere-tag on the substrate; while in the solution phase, the EF of the dimer-tags are about 7 times and 4 times higher than that of the sphere-tags and cube-tags, respectively. In addition, the EFs of the cube-tags, either on the substrate or in the solution, are both greater than that of the sphere-tags.

2.4.3. SERS Tags for Cancer Cells Imaging

I finally examined the feasibility of using the as-prepared SERS tags for imaging cancer cells. SK-BR-3 human breast adenocarcinoma cells that overexpress HER2 were chosen as a model to demonstrate the SERS imaging, while U-87 MG human glioblastoma cells that do not express HER2 were used as a negative control. The cells were incubated with the as-prepared SERS tags conjugated with HER2 antibodies. When an incident laser beam was used to illuminate a cancer cell, the SERS signals from the Raman reporter molecules of the SERS tags were detected. SERS images were acquired using a point-mapping method. It generated a spectral image by measuring the Raman spectrum of each pixel of the image, one at a time, and thus a SERS image showing the distribution of the SERS tags attached to the cancer cell could be obtained. As shown in Figure 2.15, in each panel, (a) is the bright-field optical microscope image of a single cell, while (b) are the corresponding Raman mapping image acquired based on the intensity of the band of 4-MBA at 1588

cm⁻¹. The Raman signals of 4-MBA could be detected on SK-BR-3 cells incubated with anti-HER2 antibodies-conjugated Ag dimer-tags (Figure 2.15A), sphere-tags (Figure 2.15B), and cube-tags (Figure 2.15C), respectively, while the signals could not be detected from U-87 cells due to the lack of HER2 receptors. These results show the excellent targeting capability of the as-prepared SERS tags. Typical SERS spectra of different spots on the Raman mapping images, as indicated by the coordinates A6, D6, G6 and J6, are shown in (c) of each panel. It was found that the dimer-tags gave the strongest SERS signals, about 5 and 4 times greater than those from the sphere-tags and cube-tags, respectively. These results show that the dimer-tags could be used as promising candidates in SERS imaging for cancer diagnosis.

2.5. Summary

In summary, I have successfully developed two methods for generating well-defined dimers consisting of Ag spheres with a wide range of sizes. The key to the success of these two methods lies in the control of colloidal stability by optimizing the amount of ionic species added into a suspension. The first method was a facile, one-step approach based on the polyol reduction, in which the growth of Ag nanospheres and their dimerization occurred at the same time with the addition of trace amount of NaCl. The dimers prepared from this method are consisted of single-crystal Ag nanospheres ~30 nm in diameter and separated by a gap of 1.8 nm wide. The second method was based on etching of Ag nanocubes of various sizes with Fe(NO₃)₃, in which the corners and edges of the nanocubes were truncated off to generate spherical particles, accompanied by dimerization because of the addition of

ionic species. This method can be extended to produce dimers of Ag nanospheres with a broad range of sizes. Additionally, the dimers prepared from the two methods were all SERS active and could serve as ideal systems for experimental studies on the hot-spot phenomenon in SERS. By correlating with SEM imaging, we measured the SERS EFs for individual dimers consisting of 30-nm, 40-nm, 60-nm and 80-nm Ag spheres using 4-MBT as a probe molecule, and an average value of 1.9×10^7 , 3.9×10^7 , 9.3×10^7 , and 1.7×10^8 was obtained, respectively. I further successfully demonstrated the application of using these dimers as SERS tags for Raman imaging of cancer cells, showing that the dimer-tags were better candidates for SERS imaging than the cube-tags and sphere-tags because of the preservation of the hot spots.

2.6. Experimental Section

Synthesis of Dimers of Ag Nanospheres. For the synthesis of dimers of Ag nanospheres based upon the polyol method, in a typical procedure, 5 mL of EG (J. T. Baker, 9300-03) was placed in a three-neck flask equipped with a reflux condenser and heated in an oil bath at 145 °C for 90 min. Meanwhile, 0.064 g of AgNO₃ (Aldrich, 08922LE) and 0.064 g of PVP (M_w ≈ 55,000, Aldrich, 04207JD) were dissolved separately in 3 mL of EG at room temperature. A certain amount of 10 mM NaCl, which was pre-dissolved in EG, was added to the PVP/EG solution. The AgNO₃ and PVP solutions were then simultaneously injected into the hot EG at a rate of 45 mL/h using a syringe pump (KDS-200, Stoelting). Magnetic stirring was applied throughout the synthesis. The reaction mixture went through a series of color changes, including light yellow, yellow, colorless, light yellow again, strong yellow,

and strong yellow with a slight orange tint. A series of samples were taken using a glass pipet after the reaction mixture became light yellow again. The samples were washed with acetone and then with water to remove most of the EG and PVP. In the washing process, the suspension was first centrifuged at 6,000 rpm for 45 min when acetone was used and then centrifuged at 13,000 rpm for 10 min when water was used. Finally, the precipitate was re-dispersed in ethanol for further characterization.

For the synthesis of dimers of Ag nanospheres based upon the etching process, the Ag nanocube precursors used in this method were synthesized according to published protocols developed by our group: the 47-nm cubes were synthesized using a sulfide-mediated polyol synthesis;^[47] the 82-nm and 100-nm cubes were prepared using a HCl-mediated polyol synthesis that involved oxidative etching of twinned seeds.^[45] In a typical synthesis of dimers of Ag nanospheres, 0.01 g of PVP was dissolved in 1.5 mL of ethanol. Then, a small aliquot of Ag nanocubes (dispersed in water, 20 μ L) was added into this ethanol solution. Under magnetic stirring, the nanocube suspension was mixed with 50 μ L of 10 mM $\text{Fe}(\text{NO}_3)_3$ (Aldrich, 05713KH) aqueous solution. After the reaction had proceeded at room temperature for 2 h, the product was collected by centrifugation at 10,000 rpm for 5 min and washed three times with ethanol. To prepare the 40 nm-dimer, 40 μ L of 10 mM $\text{Fe}(\text{NO}_3)_3$ was added and the etching time was 1 h. The sample was then re-dispersed in ethanol for further characterization.

In a typical process of silica coating on dimers of Ag nanospheres, the as-prepared dimers of Ag nanospheres were mixed with 0.5 mL ethanol. Then, 0.25 mL of this mixture was then transferred to a solution of 0.8 mL ethanol and 20 μ L deionized

water. Under continuous magnetic stirring, 20 μL of 29% ammonia solution and 10 μL TEOS (Aldrich, 09118DJ) were sequentially added. After the reaction had proceeded at room temperature for 5 h, the solution was centrifuged at 10,000 rpm to isolate the precipitate, which was then re-dispersed in ethanol for further characterization.

Preparation of SERS Tags. The prepared solution of dimers of Ag nanospheres, Ag nanocubes, or nanospheres was suspended in 3 mL of ethanol containing 0.5 mg/mL PVP to form a ~ 0.2 nM nanoparticle solution. 50 μL of 1 mM Raman reporter molecule (4-MBA or 1,4-BDT) in ethanol were added into the nanoparticle solution with stirring. After 1 h, 250 μL of H_2O , 70 μL of 29% ammonia solution, and 4 μL of TEOS were sequentially added. After the reaction had proceeded at room temperature for 3 h, the resultant SiO_2 -coated Ag nanoparticles were collected by centrifuging at 10,000 rpm and washed with water three times.

Amino groups were firstly introduced onto the SiO_2 shell by adding 5 μL of (3-aminopropyl)trimethoxysilane (APTMS, Aldrich, 97%) into 3 mL of SiO_2 -coated Ag nanoparticle ethanol solution (0.1 nM), followed by a 2 h reaction at room temperature with stirring. Anti-HER2 antibodies were covalently linked to the aminated SiO_2 -coated Ag nanoparticles using the periodate oxidation method. Briefly, 500 μL of anti-HER2 antibody (1 mg/mL) in 0.01 M acetate buffer (pH=5.2) were mixed with 5 μL of 0.3 M NaIO_4 . After incubation for 20 min, unreacted reagents were removed by dialysis against deionized water. The dialyzed solution was then adjusted to pH=9.0 before the amino group modified SiO_2 -coated Ag nanoparticles were added. After 6 h at 4°C , NaBH_3CN was added at a final

concentration of 5 mM followed by incubation for 6 h. The antibody-linked Ag nanoparticles were finally blocked by adding an equal volume of blocking solution (10 mM Tris-HCl buffer containing 2% bovine serum albumin (BSA), 4% sucrose, and 1% glycine, pH=7.8). The resulting SERS tags were rinsed twice with 10 mM Tris-HCl buffer (pH=7.8) and finally suspended in 100 μ L Tris-HCl buffer and stored at 4°C.

Cell Culture and Targeting. *Cell culture:* SK-BR-3 human adenocarcinoma cells and U-87 MG human glioblastoma cells were obtained from ATCC. SK-BR-3 cells were maintained in McCoy's 5A medium (ATCC), supplemented with 10% fetal bovine serum (FBS, ATCC) and 1% penicillin-streptomycin (P/S, Invitrogen). U-87 cells were maintained in Eagle's Minimum Essential Medium (EMEM, ATCC), supplemented with 10% FBS and 1% P/S. All cultures were kept in an incubator at 37 °C in a humidified atmosphere containing 5% CO₂ and the media were changed every other day. *Immunofluorescence:* The cells were seeded in the wells of a 24-well plate at a density of 1×10^4 cells/well, and left to attach overnight. The cells were then fixed with 4% formaldehyde for 10 min, and washed for 3 times with phosphate buffered saline (PBS, Invitrogen). The cells were then blocked with a PBS solution containing 1.5% BSA for 1 h, followed by incubation with primary antibody (mouse anti-HER2, 1:200) in the above-mentioned blocking solution overnight at 4 °C. After washing with PBS for 3 times, fluorescein isothiocyanate (FITC)-conjugated secondary antibody (goat anti-mouse IgG, Invitrogen, 1:200) was applied for 1 h at room temperature, followed by PBS washes. Cell nuclei were labeled with 4',6-diamidino-2-phenylindole (DAPI, Invitrogen). The fluorescent micrographs were taken using a

QICAM Fast Cooled Mono 12-bit camera (Q Imaging, Burnaby) attached to an Olympus microscope with Capture 2.90.1 (Olympus), and were then converted into corresponding color images in Photoshop (Adobe). *Cell targeting with SERS tags:* The cells were seeded onto sterile cover glasses in the wells of a 24-well plate, at a density of 5×10^3 cells/well, and left to attach overnight. The staining method was the same as immunofluorescence except for that, mouse anti-HER2 primary antibody was replaced with anti-HER2 conjugated SERS tags.

Electron Microscopy and Spectroscopic Characterization. TEM images were captured using a Tenai G2 Spirit Twin microscope operated at 120 kV (FEI, Hillsboro, OR). High-resolution TEM images were captured using a field-emission 2100F microscope (JEOL, Tokyo, Japan) operated at 200 kV. SEM images were captured using a Nova NanoSEM 230 field-emission microscope (FEI, Hillsboro, OR) operated at an accelerating voltage of 15 kV. Samples were prepared by dropping an ethanol suspension of the particles on a piece of silicon wafer (for SEM) or carbon-coated copper grid (for TEM). The UV-vis extinction spectra were recorded with a Cary 50 spectrometer (Varian) using a quartz cuvette with an optical path length of 1 cm.

SERS Measurements. The SERS spectra were recorded using a Renishaw inVia confocal Raman spectrometer coupled to a Leica microscope with 50x objective in backscattering geometry. The 785 nm (or 514 nm) wavelength was generated with a diode laser (or an argon laser) coupled to a holographic notch filter. The backscattered Raman signals were collected on a thermoelectrically cooled (-60 °C) CCD detector. The scattering spectra were recorded in the range of $800\text{-}2000\text{ cm}^{-1}$, in

one acquisition, 30 s accumulations, and 1.5 mW at the sample. SERS images were obtained using a Raman point-mapping method, in which a spectral image was generated by measuring the Raman spectrum of each pixel of the image, one at a time. SERS signals were collected by scanning an area of $24\ \mu\text{m} \times 24\ \mu\text{m}$ with a step size of $2.0\ \mu\text{m}$.

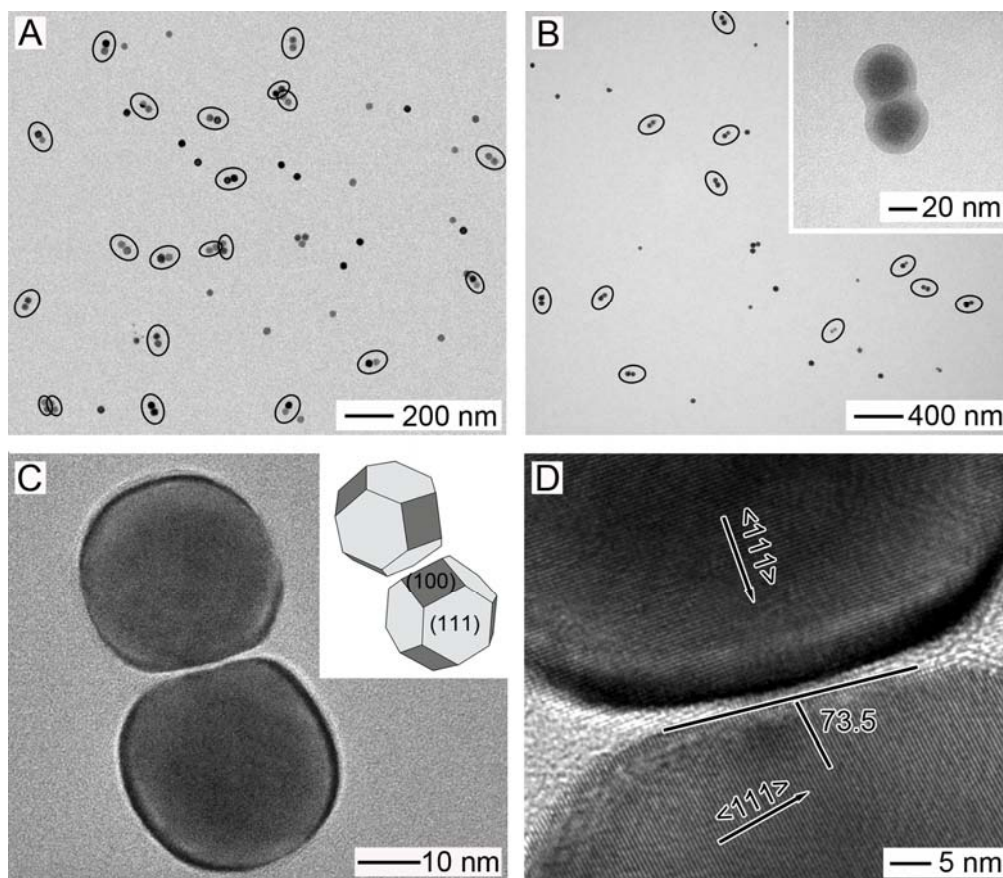


Figure 2.1. (A) TEM image of dimers of Ag nanospheres, and (B) TEM image of the dimers after their surface had been coated with silica. The dimers are highlighted by black ellipses. The inset in (B) shows a magnified TEM image of the sample. (C) TEM image of an individual dimer of Ag nanospheres. The inset in (C) gives a schematic illustration of the Ag nanospheres (cuboctahedra) in the dimer. (D) HRTEM image of the gap in an individual dimer of Ag nanospheres. Experimental conditions: temperature: 145 °C; the amount of NaCl/EG solution (10 mM): 90 μ L; and the reaction time: ca. 20.5 h.

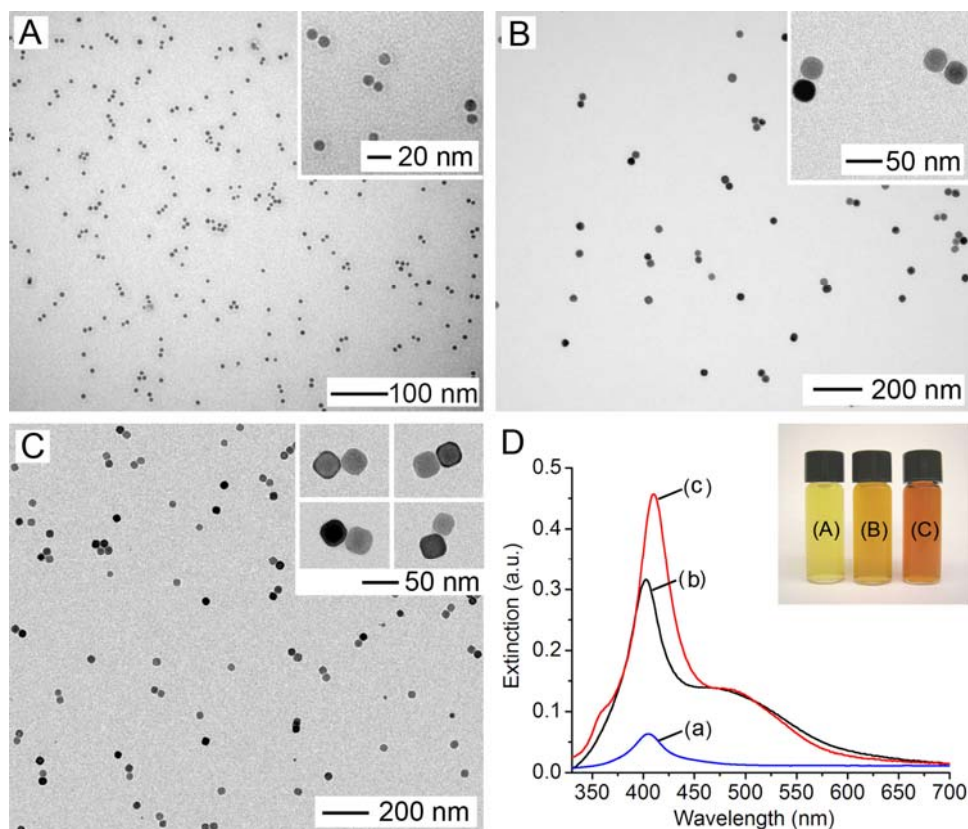


Figure 2.2. TEM images of samples obtained at three different stages of the reaction. The samples were taken when the color of the reaction mixture was (A) light yellow (ca. 19 h), (B) bright yellow with a slight orange tint (ca. 20.5 h), and (C) and dark orange yellow with a slight red-brown tint (ca. 21 h). The insets show magnified TEM images of the samples. The inset in (C) shows dimers of cubic Ag nanoparticles that were formed by interacting with different types of facets. (D) UV-vis extinction spectra of the samples taken at different reaction states. Experimental conditions: temperature: 145 °C; and the amount of NaCl/EG solution (10 mM): 90 μ L.

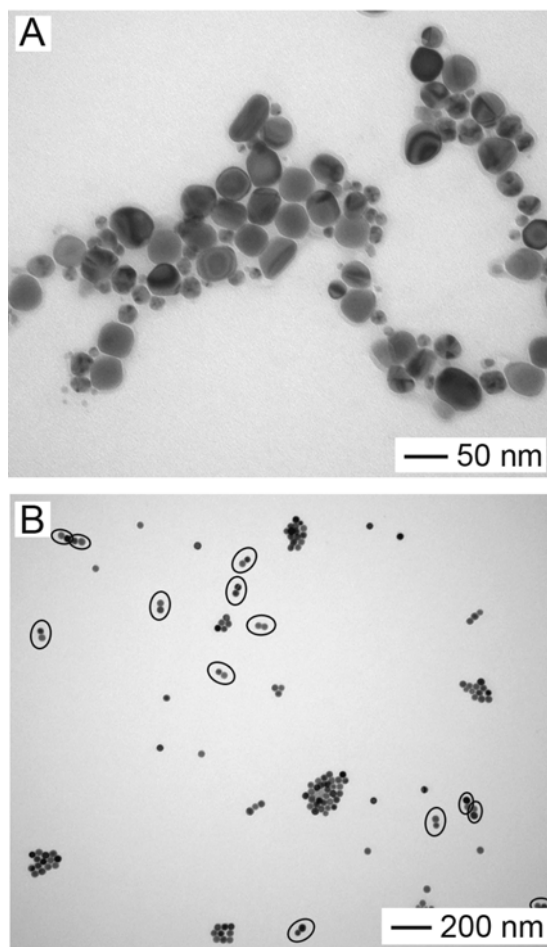


Figure 2.3. TEM images of samples prepared with the addition of different amounts of NaCl/EG solution (10 mM): (A) 66 μ L and (B) 114 μ L. The reaction temperature was 145 $^{\circ}$ C. The dimers are highlighted by black ellipses in (B).

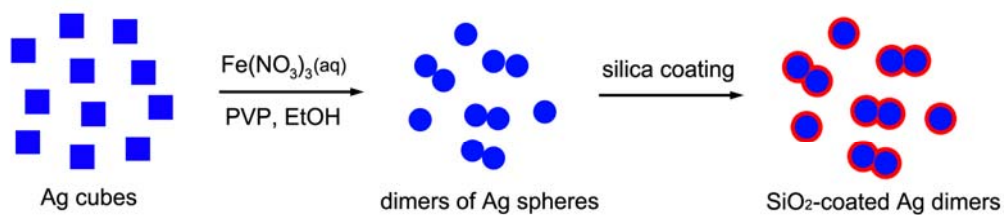


Figure 2.4. A schematic showing how dimers of Ag nanospheres are formed during etching of Ag nanocubes with an aqueous $\text{Fe}(\text{NO}_3)_3$ solution in ethanol.

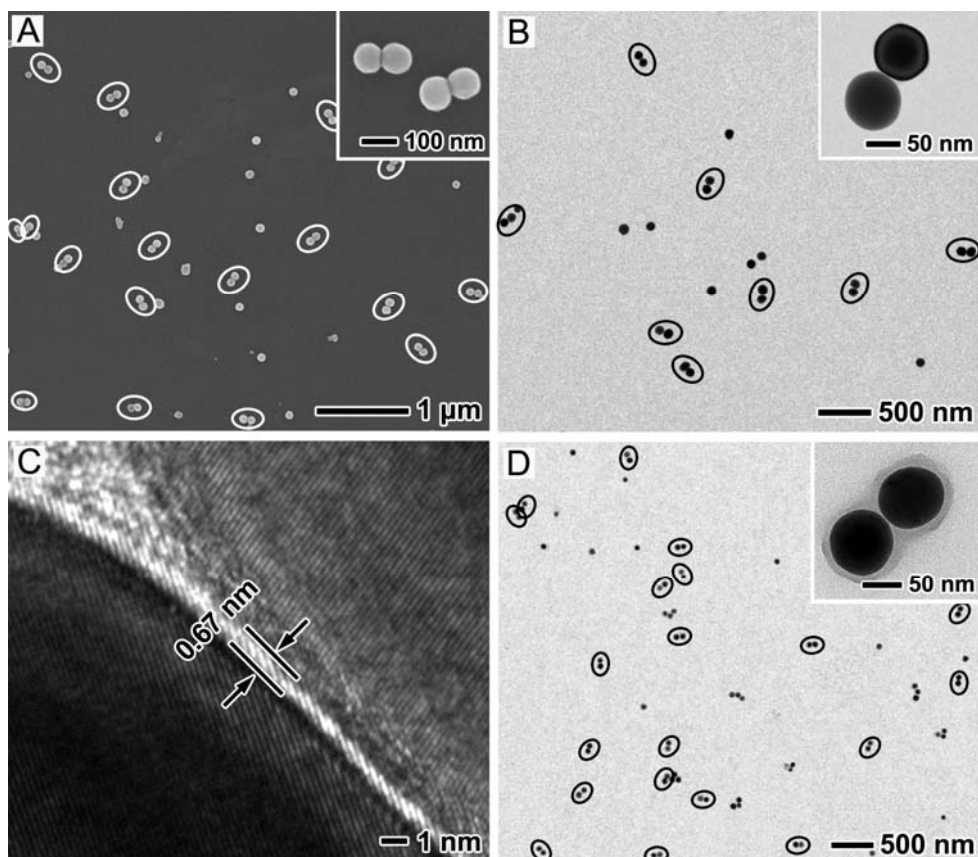


Figure 2.5. (A) SEM and (B) TEM images of dimers of Ag nanospheres prepared from 100-nm Ag nanocubes. (C) HRTEM image of the gap in a dimer and (D) TEM image of the dimers after their surface had been coated with SiO₂. The dimers are highlighted by white and black ellipses in SEM and TEM images, respectively. The inset in each image shows a magnified SEM or TEM image of the same sample. Experimental conditions: 0.01g of PVP, 1.5 mL ethanol, 50 μL of Fe(NO₃)₃ aqueous solution (10 mM), and etching for 2 h at room temperature.

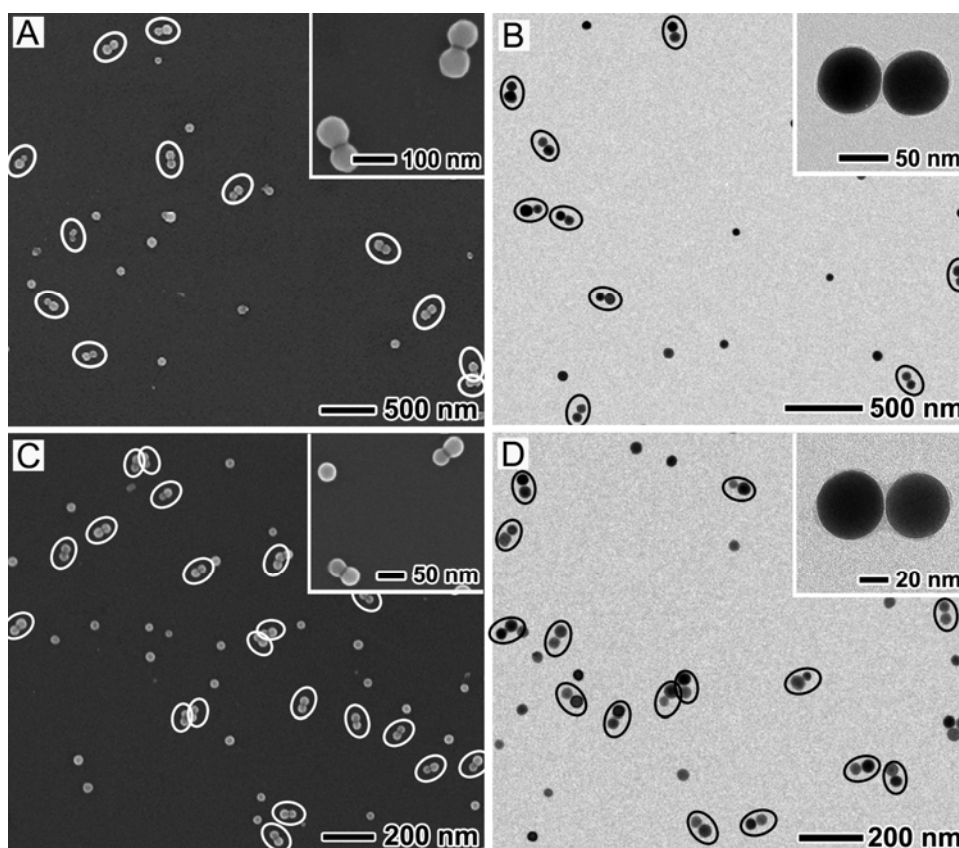


Figure 2.6. (A, C) SEM and (B, D) TEM images of dimers of Ag nanospheres with different sizes prepared from 82-nm and 47-nm Ag nanocubes, respectively. The dimers are highlighted by white and black ellipses in the SEM and TEM images, respectively. The inset in each image shows a magnified SEM or TEM image of the same sample. The dimers of 63 nm-spheres were prepared under the same conditions as those in Figure 2, except for the use of 82-nm Ag nanocubes. To prepare the dimers of 40 nm-spheres, 40 μL of 10 mM $\text{Fe}(\text{NO}_3)_3$ was added and the etching time was 1 h.

Table 2.1. A summary of the edge lengths of the Ag nanocubes (l_{cube}), diameters of the resultant spheres in the dimers after etching (d_{sphere}), percentages of dimerization, and widths of the gap regions in the dimers.

l_{cube} (nm)	d_{sphere} (nm)	dimerization%	gap width (nm)
100.4 ± 4.5	80.4 ± 4.2	66%	0.67
82.2 ± 4.5	63.0 ± 3.7	65%	0.69
47.4 ± 3.5	39.7 ± 3.4	61%	0.65

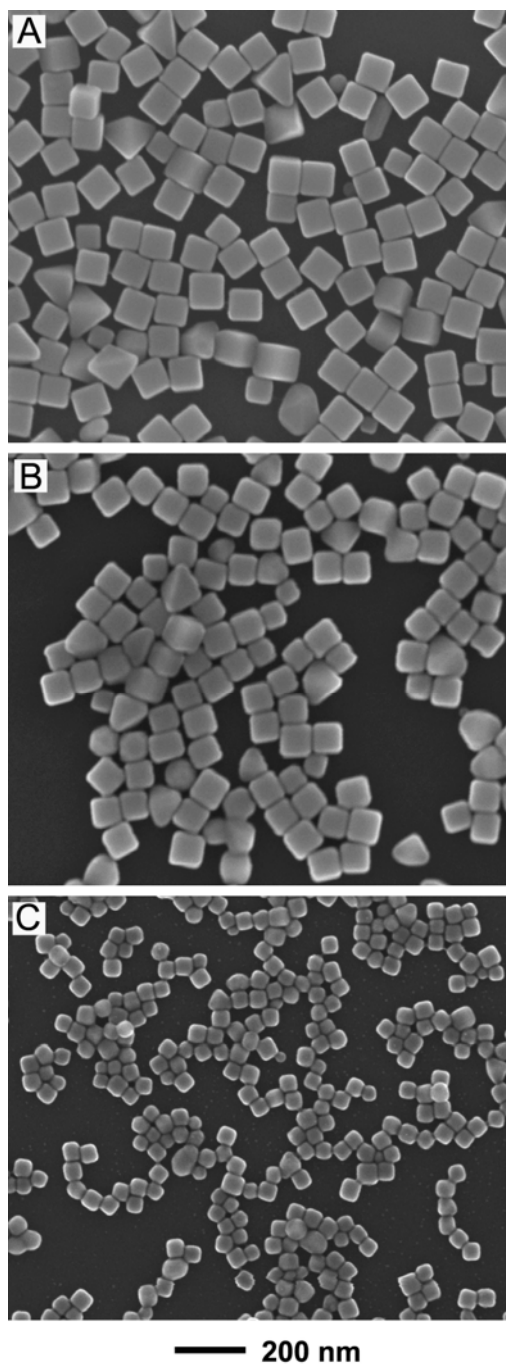


Figure 2.7. SEM images of Ag nanocubes with an average edge length of (A) 100 nm, (B) 82 nm, and (C) 47 nm, respectively.

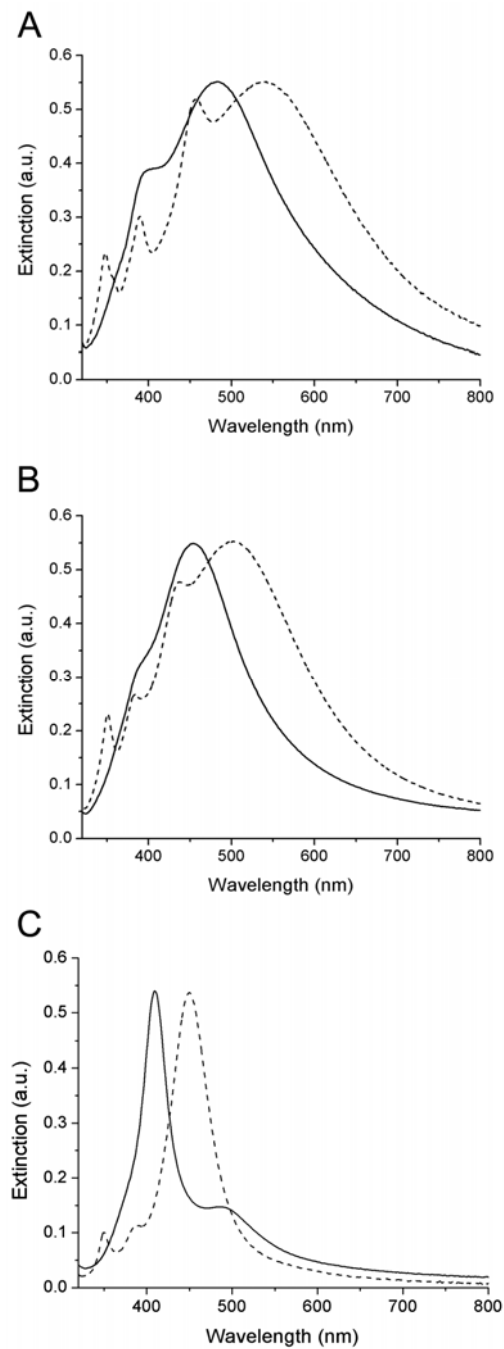


Figure 2.8. UV-vis extinction spectra of Ag nanocubes (dashed line) of (A) 100 nm, (B) 82 nm, (C) 47 nm in edge length, and spectra of the corresponding dimers of Ag nanospheres (solid line) of (A) 80 nm, (B) 63 nm, (C) 40 nm in diameter, which were prepared by etching.

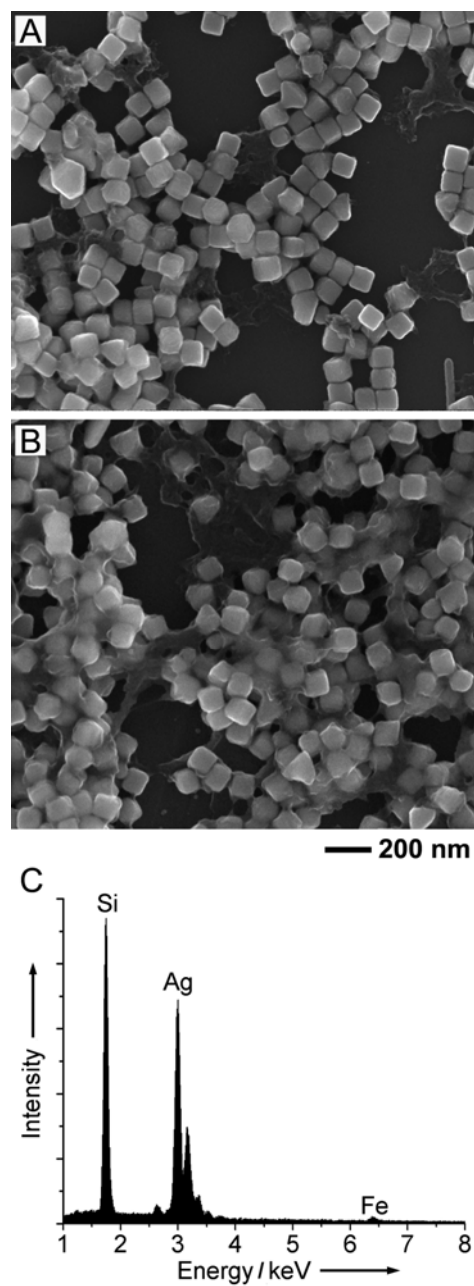


Figure 2.9. (A, B) SEM images of two samples obtained by wet etching for (A) 1 h and (B) 18 h, respectively. The etching was carried out under the same conditions as those used in Figure 2, except that no PVP was added. (C) EDX spectrum taken from the 18-h sample.

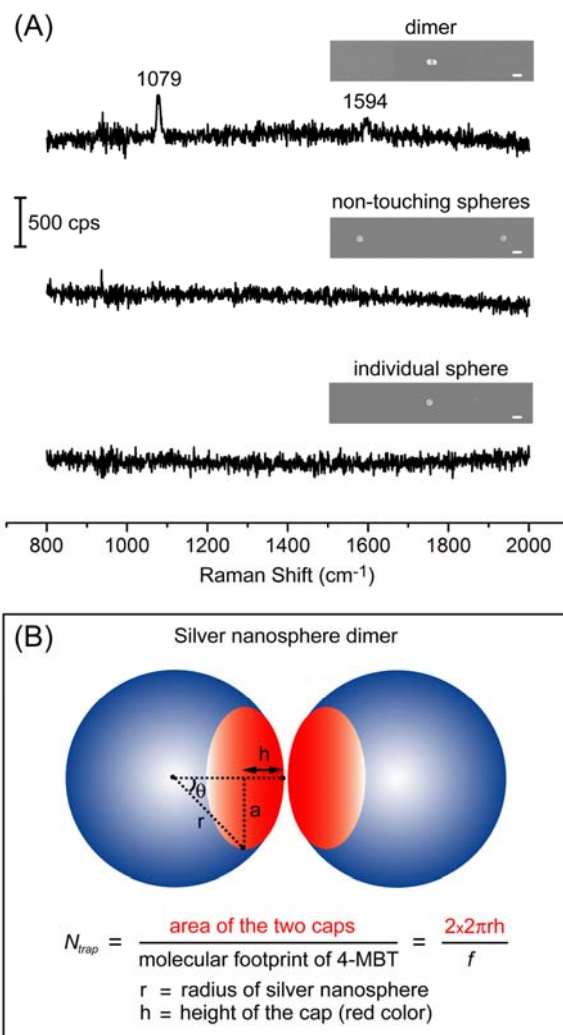


Figure 2.10. (A) SERS spectra taken from (top) a dimer of Ag nanospheres, (middle) two Ag nanospheres separated by ~ 600 nm, and (bottom) a single Ag nanosphere. The scale bars in the insets correspond to 50 nm. (B) A schematic showing our approach to estimate the number of probe molecules trapped in the hot spot (N_{trap}) of a dimer. The hot spot region is assumed to comprise a cap on the surface of each nanosphere in the inter-particle region of the dimer (red color). N_{trap} is obtained by calculating the total surface area of the hot spot region (surface area of the two caps) and dividing it by the molecular footprint of a 4-MBT molecule. In our calculations, $h = r/6.6$ (where h is the height of the cap and r is the radius of the nanosphere).

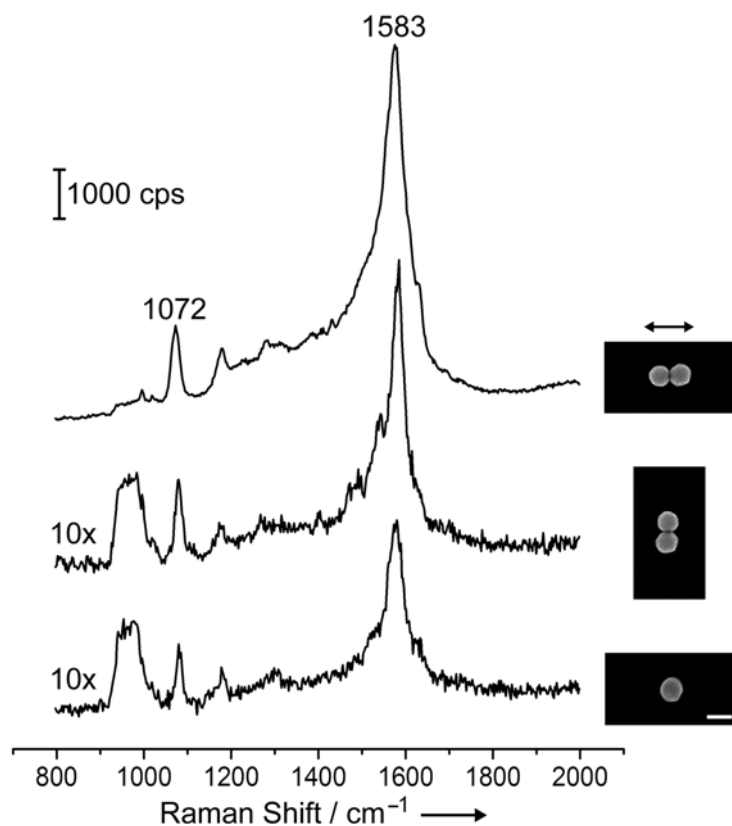


Figure 2.11. SERS spectra taken from a dimer of Ag nanospheres when the laser polarization was parallel (top trace) and perpendicular (middle trace) to the longitudinal axis of the dimer; and from a single Ag nanosphere (bottom trace). As indicated by “10×”, the intensity of the SERS signals was multiplied by ten times for the middle and bottom traces. The insets show the corresponding SEM images. The scale bar corresponds to 100 nm and is applied to all the images.

Table 2.2 Enhancement factors (EFs) for dimers of Ag nanospheres with the laser polarization parallel ($EF_{dimer-para}$) and perpendicular ($EF_{dimer-perp}$) to the dimer's longitudinal axis, as well as those of the corresponding spheres (EF_{sphere}).

d_{sphere} (nm)	$EF_{dimer-para}$	$EF_{dimer-perp}$	EF_{sphere}
80.4 ± 4.2	1.7×10^8	1.5×10^7	1.0×10^7
63.0 ± 3.7	9.3×10^7	9.2×10^6	7.8×10^6
39.7 ± 3.4	3.9×10^7	4.6×10^6	1.2×10^6

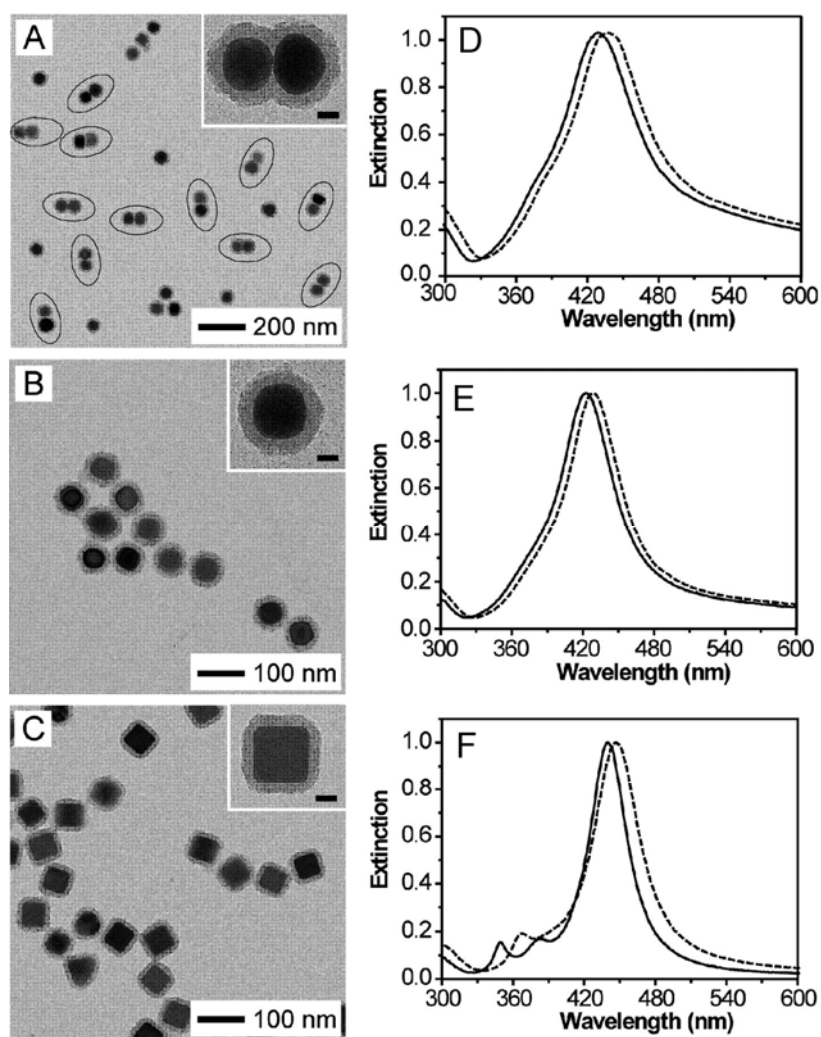


Figure 2.12. TEM images of three different SERS tags: (A) Ag dimer-tags, (B) Ag sphere-tags, (C) Ag cube-tags, with encapsulated Raman reporter molecules 4-MBA inside the SiO₂ shell. The insets show TEM images of individual SERS tags at a higher magnification. Scale bars in the insets are 20 nm. The corresponding UV-vis extinction spectra of the SERS tags were shown in the right column (D-F). The solid and dashed lines indicate the spectra of the Ag dimers, spheres and cubes before (solid) and after (dashed) the surface modification.

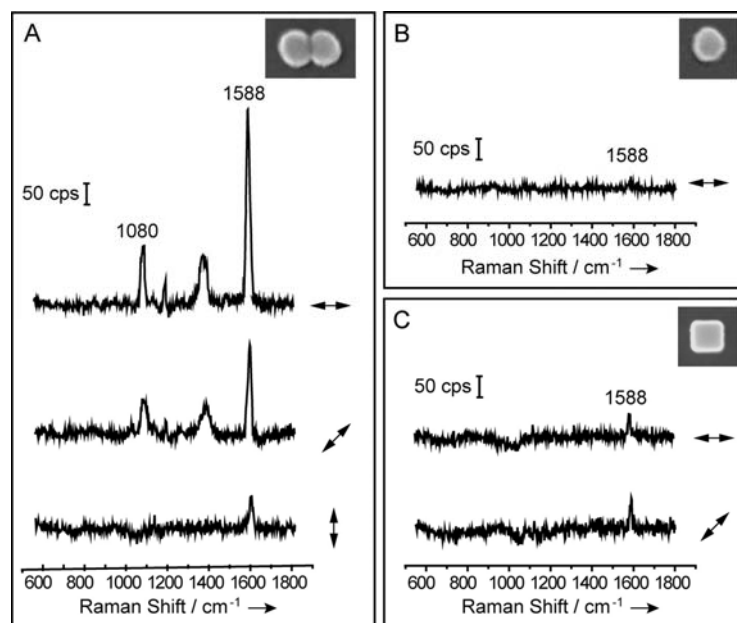


Figure 2.13. SERS spectra of individual SERS tags deposited on glass slides: (A) Ag dimer-tags, (B) Ag sphere-tags, (C) Ag cube-tags. The double arrows denote laser polarization. The insets show SEM images of the corresponding SERS tags from which the spectra were recorded.

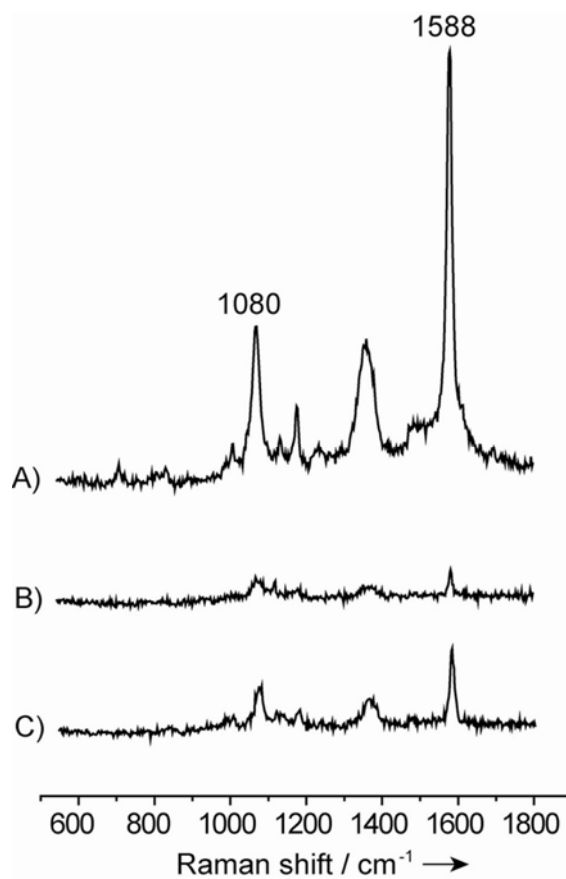









Figure 2.14. SERS spectra obtained from aqueous suspensions of (A) Ag dimer-tags, (B) Ag sphere-tags, (C) Ag cube-tags. The concentration of the SERS tags was $\sim 1.2 \times 10^{15}$ particles/L in all experiments.

Table 2.3. The EFs of individual SERS tags supported on glass slides ($EF_{\text{substrate}}$) and EFs of the different SERS tags in solution phase (EF_{solution}). Each value represents an average of the data from 20 independent experiments. The double arrows denote direction of the laser polarization.

	$EF_{\text{substrate}}$	EF_{solution}
	4.3×10^6	
	1.7×10^6	9.8×10^5
	6.6×10^5	
	2.8×10^5	1.4×10^5
	4.5×10^5	2.4×10^5
	8.7×10^5	

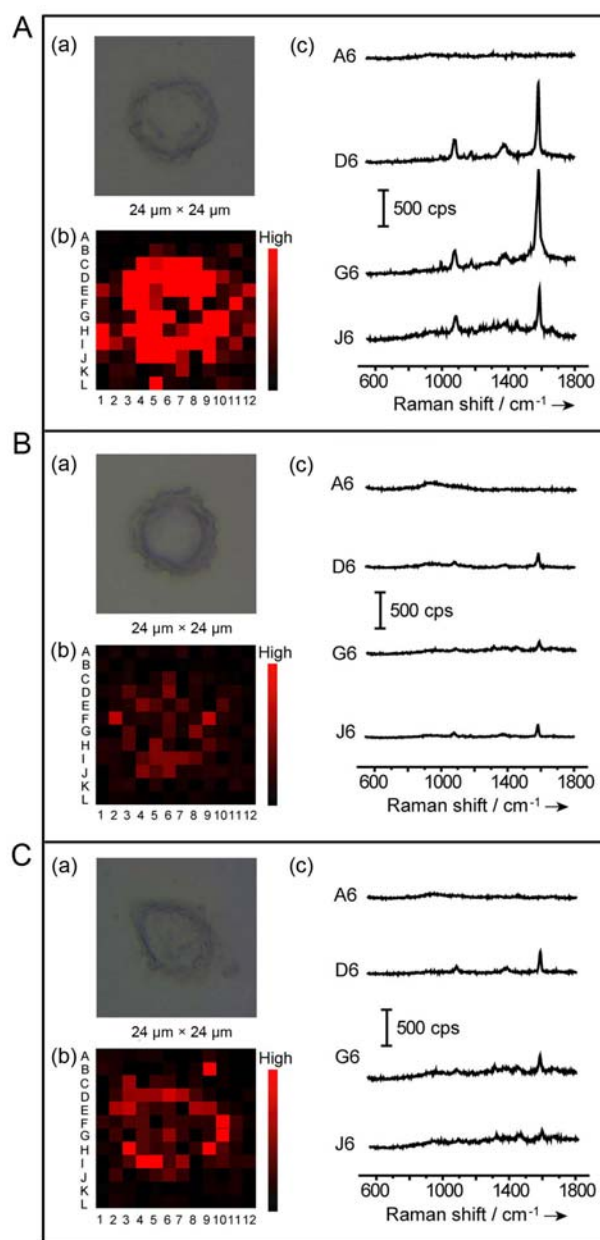


Figure 2.15. SERS images of SK-BR-3 cells incubated with (A) Ag dimer-tags, (B) Ag sphere-tags, and (C) Ag cube-tags conjugated with anti-HER2 antibodies. In each panel, (a) is bright-field images of an individual cell, while (b) is the corresponding Raman mapping image based on the intensity of the band of 4-MBA at 1588 cm⁻¹; (c) shows typical SERS spectra of the different spots on the Raman mapping images, as indicated by the coordinates A6, D6, G6, and J6.

2.7. References for Chapter 2

- [1] Cao, Y. C.; Jin, R.; Mirkin, C. A. *Science* **2002**, *297*, 1536.
- [2] Alivisatos, A. P. *Nat. Biotechnol.* **2004**, *22*, 47.
- [3] Pyayt, A. L.; Wiley, B.; Xia, Y.; Chen, A.; Dalton, L. *Nature Nanotech.* **2008**, *3*, 660.
- [4] Stiles, P. L.; Dieringer, J. A.; Shah, N. L.; Van Duyne, R. P. *Annu. Rev. Anal. Chem.* **2008**, *1*, 601.
- [5] Banholzer, M. J.; Millstone, J. E.; Mirkin, C. A. *Chem. Soc. Rev.* **2008**, *37*, 885.
- [6] Nie, S.; Emory, S. R. *Science* **1997**, *275*, 1102.
- [7] Kneipp, K.; Wang, Y.; Kneipp, H.; Perelman, L. T.; Itzkan, I.; Dasari, R. R.; Feld, M. S. *Phys. Rev. Lett.* **1997**, *78*, 1667.
- [8] Le Ru, E. C.; Meyer, M.; Blackie, E.; Etchegoin, P. G. *J. Raman Spectrosc.* **2008**, *39*, 1127.
- [9] Wang, Z.; Pan, S.; Krauss, T. D.; Du, H.; Rothberg, L. J. *Proc. Natl. Acad. Sci.* **2003**, *100*, 8638.
- [10] Otto, A. *J. Raman Spectrosc.* **2002**, *33*, 593.
- [11] Kneipp, K.; Kneipp, H.; Itzkan, I.; Dasari, R.; Feld, M. *Chem. Rev.* **1999**, *99*, 2957.
- [12] Etchegoin, P. G. ; Le Ru, E. C. *Phys. Chem. Chem. Phys.* **2008**, *10*, 6079.
- [13] Glotzer, S. C.; Solomon, M. J. *Nat. Mater.* **2007**, *6*, 557.
- [14] Whitesides, G. M.; Grzybowski, B. A. *Science* **2002**, *295*, 2418.
- [15] Klajn, R.; Bishop, K. J. M.; Fialkowski, M.; Paszewski, M.; Campbell, C. J.; Gray, T. P.; Grzybowski, B. A. *Science* **2007**, *316*, 261.

- [16] Rycenga, M.; McLellan, J. M.; Xia, Y. *Adv. Mater.* **2008**, *20*, 2416.
- [17] Alivisatos, A. P.; Johnsson, K. P.; Peng, X. G.; Wilson, T. E.; Loweth, C. J.; Bruchez, M. P.; Schultz, P. G. *Nature* **1996**, *382*, 609.
- [18] Loweth, C. J.; Caldwell, W. B.; Peng, X. G.; Alivisatos, A. P.; Schultz, P. G. *Angew. Chem. Int. Ed.* **1999**, *38*, 1808.
- [19] Park, S. Y.; Lytton-Jean, A. K. R.; Lee, B.; Weigand, S.; Schatz, G. C.; Mirkin, C. A. *Nature* **2008**, *451*, 553.
- [20] Novak, J. P.; Feldheim, D. L. *J. Am. Chem. Soc.* **2000**, *122*, 3979.
- [21] Sardar, R.; Heap, T. B.; Shumaker-Parry, J. S. *J. Am. Chem. Soc.* **2007**, *129*, 5356.
- [22] Stokes, D. L.; Alarie, J. P.; Ananthanarayanan, V.; Vo-Dinh, T. *Proc. SPIE.* **1999**, *3534*, 647.
- [23] Kundu, S.; Mandal, M.; Ghosh, S. K.; Pal, T. *J. Colloid Interface Sci.* **2004**, *272*, 134.
- [24] Stuart, D. A.; Biggs, K. B.; Van Duyne, R. P. *Analyst* **2006**, *131*, 568.
- [25] Sylvia, J. M.; Janni, J. A.; Klein, J. D.; Spencer, K. M. *Anal. Chem.* **2000**, *72*, 5834.
- [26] Qian, X.; Peng, X.-H.; Ansari, D. O.; Yin-Goen, Q.; Chen, G. Z.; Shin, D. M.; Yang, L.; Young, A. N.; Wang, M. D.; Nie, S. *Nat. Biotech.* **2008**, *26*, 83.
- [27] Lutz, B. R.; Dentinger, C. E.; Nguyen, L. N.; Sun, L.; Zhang, J.; Allen, A. N.; Chan, S.; Knudsen, B. S. *ACS Nano* **2008**, *2*, 2306.

- [28] Sun, L.; Sung, K.-B.; Dentinger, C.; Lutz, B.; Nguyen, L.; Zhang, J.; Qin, H.; Yamakawa, M.; Cao, M.; Lu, Y.; Chmura, A.; Zhu, J.; Su, X.; Berlin, A. A.; Chan, S.; Knudsen, B. *Nano Lett.* **2007**, *7*, 351.
- [29] Lee, S.; Kim, S.; Choo, J.; Shin, S. Y.; Lee, Y. H.; Choi, H. Y.; Ha, S.; Kang, K.; Oh, C. H. *Anal. Chem.* **2007**, *79*, 916.
- [30] Kim, J.-H.; Kim, J.-S.; Choi, H.; Lee, S.-M.; Jun, B.-H.; Yu, K.-N.; Kuk, E.; Kim, Y.-K.; Jeong, D. H.; Cho, M.-H.; Lee, Y.-S. *Anal. Chem.* **2006**, *78*, 6967.
- [31] Sha, M. Y.; Xu, H.; Natan, M. J.; Cromer, R. *J. Am. Chem. Soc.* **2008**, *130*, 17214.
- [32] Zavaleta, C. L.; Smith, B. R.; Walton, I.; Doering, W.; Davis, G.; Shojaei, B.; Natan, M. J.; Gambhir, S. S. *Proc. Natl. Acad. Sci.* **2009**, *106*, 13511.
- [33] Jun, B.-H.; Kim, J.-H.; Park, H.; Kim, J.-S.; Yu, K.-N.; Lee, S.-M.; Choi, H.; Kwak, S.-Y.; Kim, Y.-K.; Jeong, D.; Cho, M.-H.; Lee, Y.-S. *J. Comb. Chem.* **2007**, *9*, 237.
- [34] Lutz, B. R.; Dentinger, C. E.; Nguyen, L. N.; Sun, L.; Zhang, J.; Allen, A. N.; Chan, S.; Knudsen, B. S. *ACS Nano* **2008**, *2*, 2306.
- [35] Keren, S.; Zavaleta, C.; Cheng, Z.; de la Zerda, A.; Gheysens, O.; Gambhir, S. S. *Proc. Natl. Acad. Sci.* **2008**, *105*, 5844.
- [36] Li, W.; Camargo, P. H. C.; Lu, X.; Xia, Y. *Nano Letters* **2009**, *9*, 485.
- [37] Li, W.; Camargo, P. H. C.; Au, L.; Zhang, Q.; Rycenga, M.; Xia, Y. *Angew. Chem. Int. Ed.* **2010**, *49*, 164.
- [38] Moskovits, M. *J. Raman Spectrosc.* **2005**, *36*, 485.
- [39] Wiley, B.; Sun, Y.; Xia, Y. *Acc. Chem. Res.* **2007**, *40*, 1067.

- [40] Kim, M. H.; Lu, X.; Wiley, B.; Lee, E. P.; Xia, Y. *J. Phys. Chem. C* **2008**, *112*, 7872.
- [41] Sun, Y.; Mayers, B.; Herricks, T.; Xia, Y. *Nano Lett.* **2003**, *3*, 955.
- [42] Hao, E.; Schatz, G. C. *J. Chem. Phys.* **2004**, *120*, 357.
- [43] Wiley, B.; Herricks, T.; Sun, Y.; Xia, Y. *Nano Lett.* **2004**, *4*, 1733.
- [44] Evans, D. F.; Wennerström, H. *The Colloidal Domain: Where Physics, Chemistry, Biology, and Technology Meet*, 2nd ed.; Wiley: New York, **1999**, chapter 8.
- [45] Im, S. H.; Lee, Y. T.; Wiley, B. J.; Xia, Y. *Angew. Chem. Int. Ed.* **2005**, *44*, 2154.
- [46] Siekkinen, A. R.; McLellan, J.; Chen, J.; Xia, Y. *Chem. Phys. Lett.* **2006**, *432*, 491.
- [47] Skrabalak, S. E.; Au, L.; Li, X.; Xia, Y. *Nature Protoc.* **2007**, *2*, 2182.
- [48] Lu, X.; Au, L.; McLellan, J.; Li, Z.; Marquez, M.; Xia, Y. *Nano Lett.* **2007**, *7*, 1764.
- [49] Cobley, C.; Rycenga, M.; Zhou, F.; Li, Z.; Xia, Y. *J. Phys. Chem. C* **2009**, *113*, 16975.
- [50] Le Ru, E. C.; Etchegoin, P. G.; Meyer, M. *J. Chem. Phys.* **2006**, *125*, 204701.
- [51] Sauer, G.; Brehm, G.; Scheneider, S. *J. Raman Spectrosc.* **2004**, *35*, 568.
- [52] Osawa, M.; Matsuda, N.; Yoshii, K.; Uchida, I. *J. Phys. Chem.* **1994**, *98*, 12702.
- [53] McLellan, J. M.; Li, Z. Y.; Siekkinen, A. R.; Xia, Y. *Nano Lett.* **2007**, *7*, 1013.
- [54] Sun, Z. H.; Zhao, B.; Lombardi, J. R. *Appl. Phys. Lett.* **2007**, *91*, 221106.

Chapter 3

Quantitative Evaluation of the Transport Kinetics of Gold Nanocages in a Lymphatic System by Photoacoustic (PA) Tomography

3.1. Introduction

The metastatic spread of a tumor occurs by invading the adjacent tissue and disseminating cancerous cells through the lymphatic system into the blood stream.^[1] The closest lymph node that receives the drainage from a tumor is known as the sentinel lymph node (SLN), which represents the most likely first location of metastatic spread. To reduce the side effects of axillary lymph node dissection,^[2] sentinel lymph node biopsy (SLNB) is widely performed and has become the standard for axillary staging in breast cancer patients.^[3] Although SLNB with blue dyes (such as lymphazurin or methylene blue) or radioactive colloidal tracers has an identification rate of more than 90%, these methods involve invasive surgical operations and use carcinogenic ionizing radiation. They may also fail to identify axillary diseases owing to a high false negative rate of 5-10%.^[4] Furthermore, they can pose a risk of postoperative complications, such as seroma formation, lymphedema, and motion limitation.^[5]

Recently, ultrasound-guided fine needle aspiration biopsy (FNAB) has been clinically evaluated as a minimally invasive procedure.^[6] This technique requires

accurate positioning of the SLN, which initiates studies to develop accurate, nonionizing, and noninvasive methods for SLN mapping. Photoacoustic (PA) imaging is such a technique with remarkable resolution, which is based on the optical absorption contrast mechanism.^[7,8] Since the spatial resolution of this technique is determined by ultrasound parameters, the imaging depth can be extended to the optical quasidiffusive or diffusive regime while maintaining high resolution. By using diffusive photons, the maximum PA imaging depth can be pushed up to 50 mm in biological tissues.^[9] Our previous work successfully demonstrated PA SLN imaging by using clinically available organic dyes.^[10, 11] Although this dye-based PA imaging system has been demonstrated with a depth capability of ~31 mm, satisfactory spatial resolution, and clinical potential, it still has a number of drawbacks: *i*) the size of the dye molecule is rather small (<2 nm), so it can easily transport into the echelon lymph nodes, causing a high possibility of false positives;^[12] and *ii*) it is hard to bioconjugate the dye molecule to form molecular probe with the targeting capability.

In contrast, gold nanocages (AuNCs) have proper size range (30–100 nm) to stay ensure sufficiently fast migration and sufficient duration of trapping in SLN for imaging.^[8] The LSPR peak of AuNCs can also be precisely tuned to the NIR region from 700 to 900 nm, in which the attenuation of light by blood and soft tissue is relatively low.^[13] Most importantly, compared to organic dyes, AuNCs can be easily bioconjugated with various types of ligands such as antibodies, peptides, and nucleic acids to target specific receptors,^[14,15] potentially eliminating the need for invasive axillary staging procedures in addition to providing noninvasive SLN mapping. Other attractive features of AuNCs include bio-inertness, large absorption cross sections

(almost five orders of magnitude greater than those of conventional organic dyes), and the ability to encapsulate therapeutic drugs, which offers a great benefit for theranostic applications.^[16] In a previous report, we have demonstrated a proof-of-concept use of AuNCs for SLN imaging by PA, where an intradermal injection of 100 μ L of 2 nM AuNC solution was performed on the forepaw pad of a rat, and the SLN was identified with enhanced contrast and good spatial resolution.^[17] Many parameters associated with the AuNCs, including the minimum requirement on the concentration and injected volume and the influence of particle size, shape, and surface characteristics on their transport kinetics and uptakes by lymph nodes, still need to be examined and optimized before this system can be further considered for potential clinical use.

In this chapter, we will quantitatively evaluate the transport of AuNCs in the lymphatic system and the uptake by lymph nodes through PA imaging on a rat model. The influences of concentration, particle size, and surface characteristics will be systematically examined by using suspensions of AuNCs with a range of concentrations, two different sizes (50 and 30 nm in edge length), and three different surface charges (negative, positive, and neutral). Figure 3.1, A and B shows TEM images of AuNCs with an edge length of 50 and 30 nm, respectively. Except for the experiments involving comparison of particle size, the AuNCs used in all studies were 50 nm in edge length. The surface of the as-synthesized AuNCs is typically covered with PVP (MW \approx 55,000), a biocompatible polymer. To investigate the effect of surface charges, the PVP layer was replaced by heterofunctional poly(ethylene glycol) (PEG, MW \approx 5,000) with one end terminated in the sulfhydryl group and the

other terminated by the amine (-NH₂), methoxy (-OMe), or carboxylic acid (-COOH) group, to generate positive, neutral, or negative surface charges, respectively. The as-prepared AuNCs covered by PVP were used in all experiments except the study of surface charges. The injection volume was kept the same at 100 μL for all experiments while the concentration of AuNCs was varied. PA imaging of the axillary region of a Sprague-Dawley rat (250-300 g) was performed at different time points after intradermal injection of an aqueous suspension of AuNCs in the left forepaw pad, and the amplitude change of PA signals was then monitored as a function of time. The amounts of AuNCs accumulated in the SLNs will be quantified by ICP-MS analysis of the dissected lymph nodes after the rats are euthanized. The results can provide valuable information for further development of this AuNC-based PA imaging system for noninvasive lymph node mapping.

3.2. *Ex Vivo* and *In Vivo* Sensitivity of PA Tomography for SLN

Imaging with Gold Nanocages

Because AuNCs have much larger optical absorption cross sections than those of organic dyes,^[18] their concentration can be drastically reduced. As such, the potential toxicity of AuNCs can be minimized. We first tested the *ex vivo* sensitivity of our current deep-reflection mode PA imaging system by using gelatin phantoms based on a mixture of gelatin and AuNCs.^[17,19] As shown in Figure 3.2, PA signals from the gelatin phantom containing AuNCs at a concentration as low as 10 pM could still be detected with a signal-to-noise ratio (SNR) of ~2.2 dB. This detection limit corresponds to ~2×10⁵ (or 3.3×10⁻¹⁹ mol) AuNCs per imaging voxel. If we assume

the typical volume of SLN in a rat is $\sim 23.6 \text{ mm}^3$ (the SLN is approximated as an ellipsoid of $3 \text{ mm} \times 5 \text{ mm} \times 3 \text{ mm}$), this detection sensitivity indicates that only $\sim 1.3 \times 10^8$ (or $2.1 \times 10^{-16} \text{ mol}$) AuNCs need to enter the lymph node to provide sufficient signals for imaging. The noise equivalent concentration (i.e., the concentration that provides an SNR of unity) is calculated to be $\sim 4.5 \text{ pM}$.

To evaluate the *in vivo* sensitivity of our PA system and AuNCs for lymph node imaging, we intradermally injected an aqueous suspension of AuNCs at a specific, decreasing concentration (100, 50, and 20 pM) at a dose of $100 \mu\text{L}$ (this corresponds to an amount of 2.2×10^7 , 1.1×10^7 , and 0.55×10^7 AuNCs per gram of body weight, respectively) on the left forepaw pad of a rat and then the left axillary region of the rat was noninvasively imaged using the PA system. Before the injection of AuNCs, PA images were acquired as control images (Fig. 3.3, A, D and G), revealing the vasculature within $\sim 3 \text{ mm}$ below the skin surface. After the injection of AuNCs, a series of PA images were obtained up to 120 min post-injection. It can be observed that the SLNs started to appear at 5 min after the injection of 100 pM (Fig. 3.3B) and 50 pM (Fig. 3.3E) AuNC suspensions while the SLN was not detected at 5 min after the injection of 20 pM AuNCs (Fig. 3.3H). As time elapsed, the PA signals gradually increased and the SLNs, including the case with the injection of 20 pM AuNCs, could be clearly observed at 120 min post-injection (Fig. 3.3, C, F and I). Note that the minimum concentration of 20 pM we used here for PA SLN imaging in a rat model was about 100 times less than the value (2 nM) reported in our previous work,^[17] greatly reducing the potential toxicity of AuNCs. It is also worth pointing out that the drainage of AuNCs to lymph nodes was much faster than that of Au nanorods, even at

a relatively low injection concentration. In our previous study, it took more than 20 h for Au nanorods (10 nm in diameter and 41 nm in length) with an injection concentration of 1 μM to be observed at SLNs.^[20] These results suggest that AuNCs should serve as a better diagnostic imaging agent than Au nanorods for SLN imaging.

We also performed *in vivo* PA SLN imaging in two additional rats at each concentration, following the same procedure. The PA signal enhancements in SLNs were summarized as a function of time (Fig. 3.4A). Each data point was normalized against the PA signal from the corresponding adjacent blood vessels (BV) acquired before the injection of AuNCs. This normalization method was also applied to the experiments described in other sections. We found that the PA signal enhancement increased with increasing injection concentration. The enhancement also increased with post-injection time, indicating the gradual accumulation of AuNCs in SLNs. For example, after the injection of 100 pM AuNCs, the enhancement was $182\% \pm 12\%$ at $t=5$ min, and then gradually increased to $355\% \pm 24\%$ at $t=120$ min post-injection. For the group with 20 pM AuNCs, the SLNs in two of the three rats were not even detected at $t=120$ min post-injection. This high false negative rate indicates that we had reached the *in vivo* detection limit of the PA system. Note that the standard errors for PA signal enhancement at 5 and 30 min post-injection in the group of 50 pM AuNCs injection were still relatively high compared to those with 100 pM sample, indicating that a 100 pM suspension of AuNCs at a dose of 100 μL (2.2×10^7 AuNCs per gram of body weight) seems to be the best candidate to start with for SLN imaging. We further quantified the number of AuNCs accumulated in the SLN by ICP-MS analysis of the excised node. The accumulated amount of AuNCs in SLN for

the 100 pM sample was approximately 2 and 7.5 times higher than the 50 pM and 20 pM samples, respectively (Fig. 3.4B). The average numbers of AuNCs in SLN per mass at 120 min post-injection of 20, 50 and 100 pM of AuNCs were about $(0.86\pm 0.74)\times 10^{10}$, $(3.25\pm 1.07)\times 10^{10}$, and $(6.43\pm 0.94)\times 10^{10}$ AuNCs/g, respectively, which were qualitatively consistent with the trend revealed by PA enhancement shown in Figure 3.4A. According to our measurements, the average weight of the SLN in the rats was about 16.8 mg; therefore, about 18% of the injected 50 pM and 100 pM AuNCs had been accumulated in the SLN at $t=120$ min post injection, while about 12% of the injected 20 pM AuNCs had been accumulated in the SLN.

3.3. Depth Capability of PA Tomography for SLN Imaging with Gold Nanocages

The SLNs of rats are located at ~ 2 mm below the skin surface. In humans, the mean depth of SLNs is ~ 12 mm underneath the skin.^[17] Therefore, it is necessary to demonstrate the minimal dose of AuNCs at the clinical depth by using the same PA imaging modality. Similar to the previous experiments, after the SLN of a rat in the group of 100 pM AuNCs was identified (Fig. 3.5A), a chicken breast tissue of 5 mm thick was placed on top of the axillary surface of the rat, and a PA image was acquired at 150 min post-injection. The SLN of the rat could be obviously identified from this image, and the total depth of the SLN was now ~ 7 mm (Fig. 3.5B). With the addition of a second layer of chicken breast tissue, an imaging depth of ~ 12 mm was achieved by acquiring a PA image at 180 min post-injection (Fig. 3.5C), and the SLN can still be imaged with a good contrast. In the B-scan image (Fig. 3.5D), the depth

information of the SLN is clearly shown with ~ 7 dB SNR.

3.4. Comparison of Gold Nanocages with Different Sizes

An ideal mapping agent for lymphoscintigraphy should have proper size: on one hand, it should be small enough to rapidly drain to lymphatic vessels and then transport to lymph nodes; on the other hand, it should be large enough to stay within the lymph nodes during the imaging process. Particles smaller than 5 nm could easily leak into blood capillaries or migrate to echelon lymph nodes and thus cause false positives,^[21] while particles larger than 100 nm are believed to be trapped in the interstitial compartment for a long period of time, and are thus unable to transport to lymph nodes fast enough for lymphoscintigraphy.^[22] Therefore, it is critical to identify an optimal size range for the AuNCs in order to have sufficiently fast migration and sufficient duration of trapping for SLN mapping.

We compared the PA enhancements in SLNs as a function of time using AuNCs with edge lengths of 50 nm and 30 nm, respectively (Fig. 3.6A). We performed the *in vivo* PA imaging in 3 rats for each group. Note that the surface of the as-prepared AuNCs was covered with PVP, and thus the hydrodynamic diameter of the AuNCs measured by dynamic light scattering was about 95 nm, so we did not choose AuNCs with an edge length larger than 50 nm. Additionally, nanoparticles with larger size (>50 nm) are known to exhibit short circulation times in blood,^[23] making them less useful in diagnostic imaging. The injection concentrations for both the 30-nm and 50-nm AuNCs were 200 pM, as the SLN could hardly be detected with the injection of 30-nm AuNCs at a concentration of 100 pM. Both curves show that SLNs could be

detected at 5 min post injection, and the PA signal enhancement kept increasing in the following 120 min. It can be seen that the 50-nm AuNCs showed higher signal enhancement (about 150% to 170%) than the 30-nm sample. This difference can be ascribed to the fact that the 30-nm AuNCs had a smaller optical absorption cross section than the 50-nm AuNCs, generating weaker PA signals. We have also measured the absorption cross sections of these AuNCs using a PA-based method developed in our groups.^[18] The absorption cross section of the 50-nm AuNCs was found to be about 2.1 times higher than that of the 30-nm AuNCs. Figure 3.6B shows a comparison of the accumulation of 50-nm and 30-nm AuNCs in SLNs as a function of post-injection time calculated from the PA signals. Since the PA signal is directly proportional to the absorption coefficient (μ_a) of the AuNCs,^[17] the accumulation of AuNCs can be calculated according to the equation: $N_{\text{nano}} = \mu_{a,\text{nano}} / \sigma_{a,\text{nano}}$, where N_{nano} is the concentration of the AuNCs (number of particles per m^3) and $\sigma_{a,\text{nano}}$ is the absorption cross section (m^2) of the nanocages. Each data point was then normalized against the accumulation of 50-nm AuNCs in SLN at 5 min post-injection. It can be seen that the 30-nm AuNCs transported into the SLN faster than the 50-nm AuNCs and showed a larger amount of accumulation in the SLN. The ICP-MS data in Figure 3.6C indicate that the average number of 30-nm AuNCs in the excised SLN per mass at 120 min post-injection was about 1.8 times higher than that of the 50-nm AuNCs, $(14.5 \pm 1.0) \times 10^{10}$ vs. $(8.0 \pm 0.6) \times 10^{10}$ AuNCs/g, which is consistent with the trend of accumulation derived from the PA signals.

3.5. Comparison of Gold Nanocages with Different Surface Charges

Early studies on the transport kinetics and lymphatic uptake of particles showed that surface characteristics, such as charge and hydrophobicity, could affect the rate of particle drainage from the injection site to lymph nodes and their distribution within the lymphatic system.^[22] Therefore, it is important to study the transport behaviors of AuNCs with different surface charges. We replaced the PVP layer on the AuNCs with SH-PEG₅₀₀₀-X (X=OMe, NH₂, or COOH to give a neutral, positive, or negative surface charge). Following the same procedure, we performed *in vivo* SLN imaging using AuNCs modified with different surface charges. Each group had 3 rats and the injection concentration was 200 pM for all 3 groups. Figure 3.7 shows typical PA images acquired before as well as 5 min and 60 min after the injection of AuNCs modified with different surface charges. Unlike the other two groups, AuNCs with negative charges accumulated not only in the SLN but also in the adjacent lymphatic vessels. The lymphatic vessels began to show up in PA images at 5 min post injection (Fig. 3.7B) and the AuNCs could be trapped there for 60 min (Fig. 3.7C). It is known that lymphatic vessels play an important role in lymphatic metastasis,^[24,25] providing crucial prognostic information. Cancer cells can exploit these vascular systems by expressing growth factors, altering the normal pattern of angiogenesis and lymphatic vessel growth, creating conduits for tumor metastasis. As a result, the ability to target and image aberrant drainage patterns is of clinical significance. However, studies on lymphatic vessels have been hindered by technical limitations.^[26] The AuNCs with negative charges can potentially be used as a good contrast agent for lymphangiogenesis imaging. In addition, AuNCs with positive charges also showed a unique feature. It took 30 to 60 min, a much longer time than the other two groups, to

transport to SLNs and accumulate enough amounts for PA imaging (Fig. 3.7, D-F). Figure 3.8A shows PA signal enhancement in SLNs as a function of time after the injection of AuNCs with different surface charges. It can be seen that the signal enhancement originating from AuNCs with positive charges is much lower than that from the neutral AuNCs, especially in the first 60 min post injection, indicating a much slower transport rate to lymph nodes. As for the PA enhancement from the AuNCs with negative charges, it was also lower (about 50% to 60%) than the neutral AuNCs, but higher (about 150% to 160%) than the positive AuNCs in the first 60 min post injection, and then leveled off. The ICP-MS data in Figure 3.8B show that the average number of AuNCs in the excised SLN per mass at 240 min post injection decreased in the order of neutral > positive > negative, which is consistent with the trend for PA signal enhancement shown in Figure 3.8A.

We also found that the AuNCs were not only able to transport to the SLN, but also further down to the second and third axillary lymph nodes of a rat. As shown in Figure 3.9, C and D, both *in vivo* and *ex vivo* PA images clearly show the accumulation of nanocages in all three lymph nodes of the rat after the injection of AuNCs at a relatively higher concentration (500 pM) at 72 h post injection. Taken together, these features can probably be used to design AuNCs with switchable surface charges for noninvasive axillary lymph node staging of breast cancer by taking advantage of their different transport kinetics in lymph nodes. For example, we can conjugate the surface of AuNCs with an enzyme-sensitive peptide which can be cleaved by enzymes (e.g., matrix metalloproteases, a recognized biomarker associated with cancer-cell invasion and metastasis) overexpressed by cancer cells in the

metastatic lymph node.^[27] As such, the surface charges on the AuNCs will be different before and after the enzyme cleavage, and the transport rates of AuNCs between lymph nodes will be different for patients with different stages of metastatic cancer. In addition, we can also attach fluorescence dyes to the surface of AuNCs via an enzyme-cleavable peptide.^[28] The dye molecules will be cleaved and released from the surface of the nanocage in the presence of a protease, and thus fluorescence will be recovered. In practice, the distribution of AuNCs in lymph nodes can be mapped by PA imaging while the protease activity can be monitored by fluorescence spectroscopy, providing critical information for the diagnosis of breast cancer metastasis. Related researches are currently underway.

3.6. Summary

In this chapter, we have quantitatively evaluated the transport of AuNCs in a lymphatic system and their uptakes by lymph nodes in a rat model through PA imaging. We systematically examined and optimized a number of experimental parameters including the concentration, size, as well as surface characteristics of the AuNCs. We reduced the concentration of injected AuNCs down to 100 pM (20 times lower than our previous proof-to-concept report, greatly reducing the potential toxicity of AuNCs) for SLN imaging at a depth of ~12 mm (the depth of SLN in human) while keeping a sufficient signal-to-noise ratio. It was found that the 30-nm AuNCs exhibited a faster transport rate and a larger amount of accumulation in the SLN than the 50-nm AuNCs, but the latter generated stronger PA signals due to a larger optical absorption cross section. This result indicates that the 50-nm AuNCs

seem to be an ideal contrast agent for SLN imaging by PA tomography. As for AuNCs with different surface charges, their transport rates to SLNs decreased in the order of neutral > negative > positive. In addition, AuNCs with negative charges could be trapped in lymphatic vessels, making them potentially useful as contrast agents for lymphangiogenesis by PA imaging. We also found that the AuNCs were not only able to transport to the SLN, but can also further to the second and third axillary lymph nodes of a rat. These results can serve as guidelines for choosing optimal experimental parameters of AuNCs in metastatic lymph nodes mapping and other biomedical applications by noninvasive PA imaging.

3.7. Experimental Section

Synthesis and Surface Modification of AuNCs. The AuNCs were synthesized using the galvanic replacement reaction between Ag nanocubes and chloroauric acid in water according to our published protocol.^[29] To obtain different surface charges, the nanocages were derivatized with SH-PEG₅₀₀₀-X (X=OMe, NH₂, and COOH; all from Laysan Bio; Mw ≈ 5,000). In a typical process, 0.1 mL of HS-PEG₅₀₀₀-X aqueous solution (0.1 mM) and 0.1 mL of AuNCs aqueous suspension (1 nM in terms of particles) were added to 2.8 mL deionized water. The mixture was kept stirring at 4 °C overnight. After that, the mixture was centrifuged at 14,000 rpm for 15 min and the supernatant was decanted to remove the excess PEG. The PEGylated-AuNCs were then washed with water twice and re-suspended in water at a concentration of 200 pM (in terms of particles) for *in vivo* studies.

The PA Imaging System. A deep reflection-mode PA imaging system was used

for all PA experiments.^[19] A tunable Ti:sapphire laser (LT-2211A; Lotis TII, Minsk, Belarus) pumped by a Q-switched Nd:YAG (LS-2137; Lotis TII) laser was used for excitation, providing <15-ns pulse duration and a 10-Hz pulse repetition rate. A dark-field ring-shaped illumination was adopted to reduce the surface PA signal generation.^[30] The light energy on the sample surface was controlled to be less than the American National Standards Institute standard for maximum permissible exposure. A 5-MHz central frequency, spherically focused ultrasonic transducer (V308; Panametrics-NDT, Waltham, MA, USA) was used to acquire the generated PA signals. The 5 MHz ultrasonic transducer yields axial and transverse resolutions of 150 and 560 μm , respectively. The signal was amplified by a low-noise amplifier (5072PR; Panametrics-NDT) and recorded using a digital oscilloscope (TDS 5054, Tektronix, Beaverton, OR). A photodiode (SM05PD1A, Thorlabs, Newton, NJ) was used to compensate for the energy instability of laser pulses. A linear translation stage (XY-6060, Danaher Motion, Radford, VA) was used for raster scanning to obtain three-dimensional (3D) PA data. The signal was not averaged for any image to shorten the data acquisition time. By measuring PA amplitudes according to the arrival times, one-dimensional depth-resolved images (A-lines) are acquired. Additional raster scanning along a transverse direction provides two-dimensional depth-resolved images (B-scans), consisting of multiple A-scans, and further scanning along the other transverse direction provides 3D images. The acquired 3D raw data can be processed as a maximum amplitude projection (MAP)—a projection of the maximum PA amplitude along each A-line onto the corresponding plane. Typical scanning values were as follows: field of view, 20×20 mm; voxel dimension, $0.2 \times$

0.4 mm; laser pulse repetition rate, 10 Hz; and acquisition time, ~24 min. The transducer was located inside a water container with an opening of 5×5 cm at the bottom, sealed beneath a photoacoustically transparent clear membrane. The rats or gelatin phantom samples made from a mixture of gelatin solution and AuNCs were placed under the membrane, and ultrasonic gel was used for ultrasound coupling.

Animal Handling. All animal experiments were in compliance with the Washington University Institutional Animal Care and Use Committee. Sprague–Dawley rats weighting 200–300 g (Harlan, Indianapolis, IN) were anesthetized with a mixture of ketamine (87 mg/kg) and xylazine (13 mg/kg) at a dose of 0.15 mL per 100 g body weight. The hair in the left axillary region was removed by gentle clipping and depilatory cream before imaging. PA imaging was acquired before and after intradermal injection of AuNC solution (0.1 mL) in the left forepaw pad. Full anesthesia of the animal was maintained throughout the experiment by using vaporized isoflurane (1 L/min of oxygen and 0.75% isoflurane) and vitals were monitored by a pulse oximeter (NOMIN Medical, 2000SA). The body temperatures of the rats were maintained with a water heating pad. After data acquisition, the rats were euthanized by overdosed pentobarbital and SLNs were dissected for ICP-MS measurements.

ICP-MS of AuNCs in Dissected Lymph Nodes. The excised lymph nodes were weighed and then were completely digested with 5 mL of aqua regia in a 50 mL beaker at boiling temperature. The solution was evaporated to 1 mL and subsequently diluted to 15 mL with deionized water. Samples were passed through a 0.45-mm filter to remove any undigested debris prior to ICP-MS measurement. The analysis of Au

content was performed with ICP-MS (Perkin Elmer, Elan DRC II), and the concentration of Au ions was converted to the concentration of nanocages once the geometric dimensions of the nanocage had been determined from TEM images.

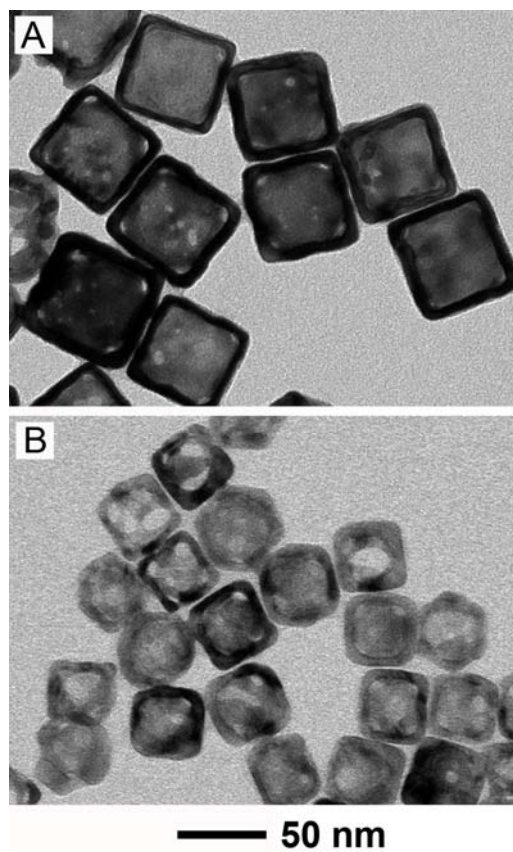


Figure 3.1. TEM images of Au nanocages (AuNCs) with average edge lengths of (A) 50 nm and (B) 30 nm, respectively.

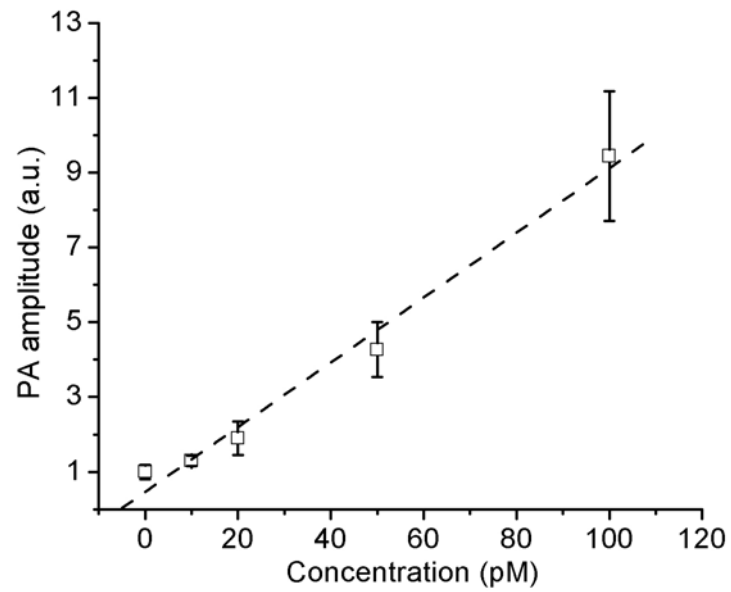


Figure 3.2. PA signals recorded from gelatin phantoms containing AuNCs at various concentrations ($R^2=0.99$), showing that the detection limit of AuNCs (50 nm in edge length) was less than 10 pM, or 2×10^5 (or 3.3×10^{-19} mol) AuNCs per imaging voxel, for the PA system. If we assume the typical volume of the SLN in a rat is $\sim 23.6 \text{ mm}^3$ (the SLN is approximated as an ellipsoid of $3 \text{ mm} \times 5 \text{ mm} \times 3 \text{ mm}$), this detection sensitivity indicates that only $\sim 1.3 \times 10^8$ (or 2.1×10^{-16} mol) AuNCs need to enter the lymph node to provide sufficient signals for imaging.

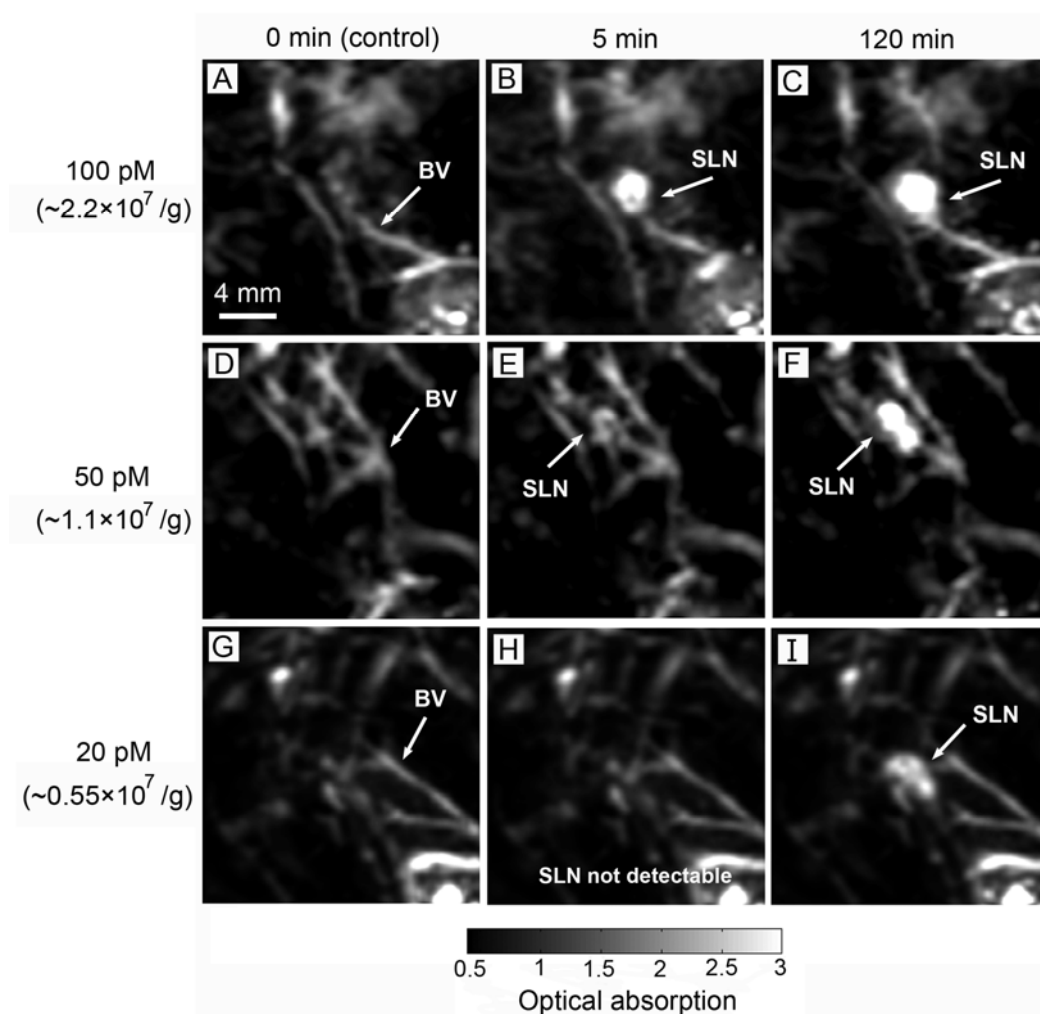


Figure 3.3. PA images of the axillary region of rats acquired at 0, 5, and 120 min after injection of the AuNCs with different concentrations. (A, D, G) PA images before injection of the AuNCs; (B, E, H) PA images 5 min after the injection of AuNCs at different concentrations. The SLNs started to appear except for the 20 pM sample; (C, F, I) PA images 120 min after the injection of AuNCs at different concentrations. The three concentrations correspond to amounts of 2.2×10^7 , 1.1×10^7 , and 0.55×10^7 AuNCs per gram of body weight, respectively. BV, blood vessels; SLN, sentinel lymph node.

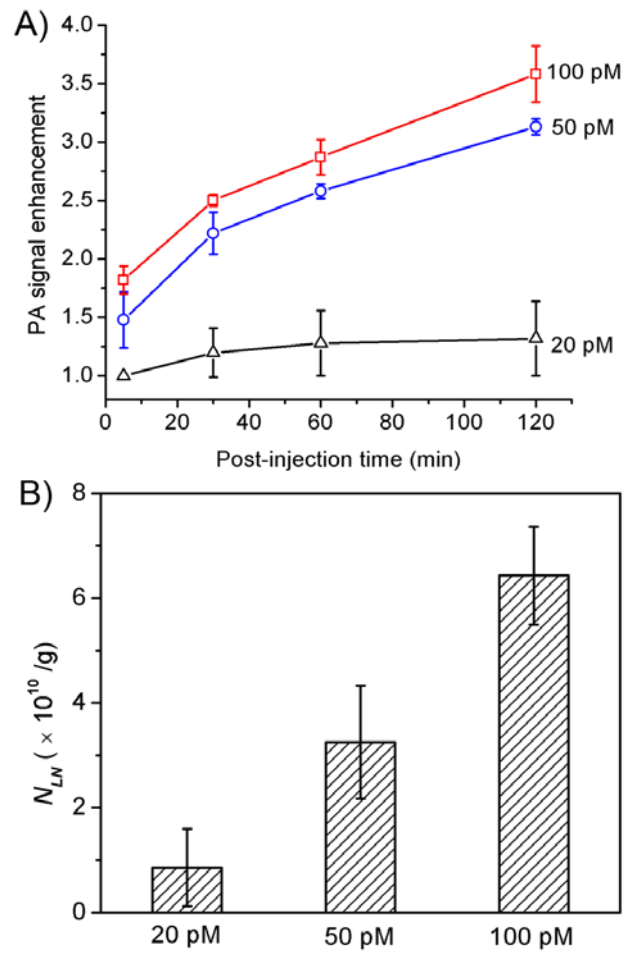


Figure 3.4. (A) PA signal enhancement in SLNs as a function of time after the injection of AuNCs at different concentrations ($n=3$ rats for each group): 100, 50, and 20 pM, respectively. Each data point was normalized against the PA signal from the corresponding adjacent blood vessels before the injection of AuNCs. (B) Average numbers of AuNCs accumulated in the SLNs dissected at 120 min post injection, as measured using ICP-MS. Here N_{LN} denotes the number of AuNCs per unit lymph node mass (g).

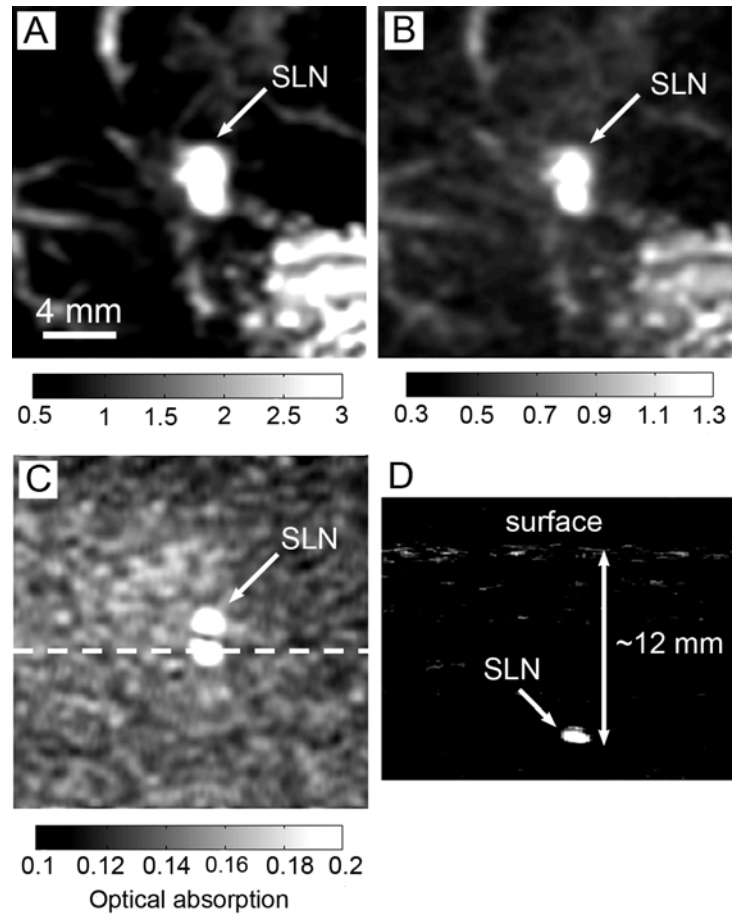


Figure 3.5. PA imaging of SLN in a rat after the injection of 100 pM AuNCs. The PA images were acquired (A) at 120 min post-injection with no chicken breast tissue added, (B) at 150 min post injection with one layer (thickness: 5 mm) of chicken breast tissue added, and (C) at 180 min post injection with two layers (total thickness: 10 mm) of chicken breast tissue added. (D) PA B-scan along the dashed line in (C), showing the SLN located at a depth of ~12 mm. SLN, sentinel lymph node.

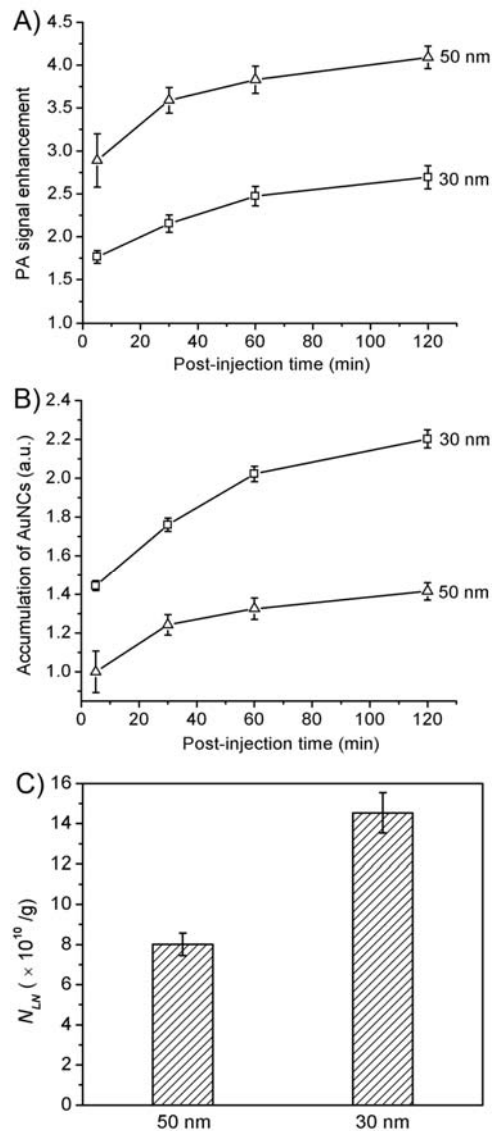


Figure 3.6. (A) PA signal enhancement in SLNs after the injection of 50-nm and 30-nm AuNCs with the same concentration and dose (200 pM and 100 μ L) as a function of post-injection time ($n=3$ rats for each group), respectively. (B) Accumulation of the 50-nm and 30-nm AuNCs in SLNs as a function of post-injection time calculated based on the PA signals. The data points were normalized against the 50-nm AuNCs at 5 min post injection. (C) Average numbers of AuNCs accumulated in the SLNs dissected at 2 h post injection of the 30-nm and 50-nm AuNCs, as measured by ICP-MS. Here N_{LN} denotes the number of AuNCs per unit lymph node mass (g).

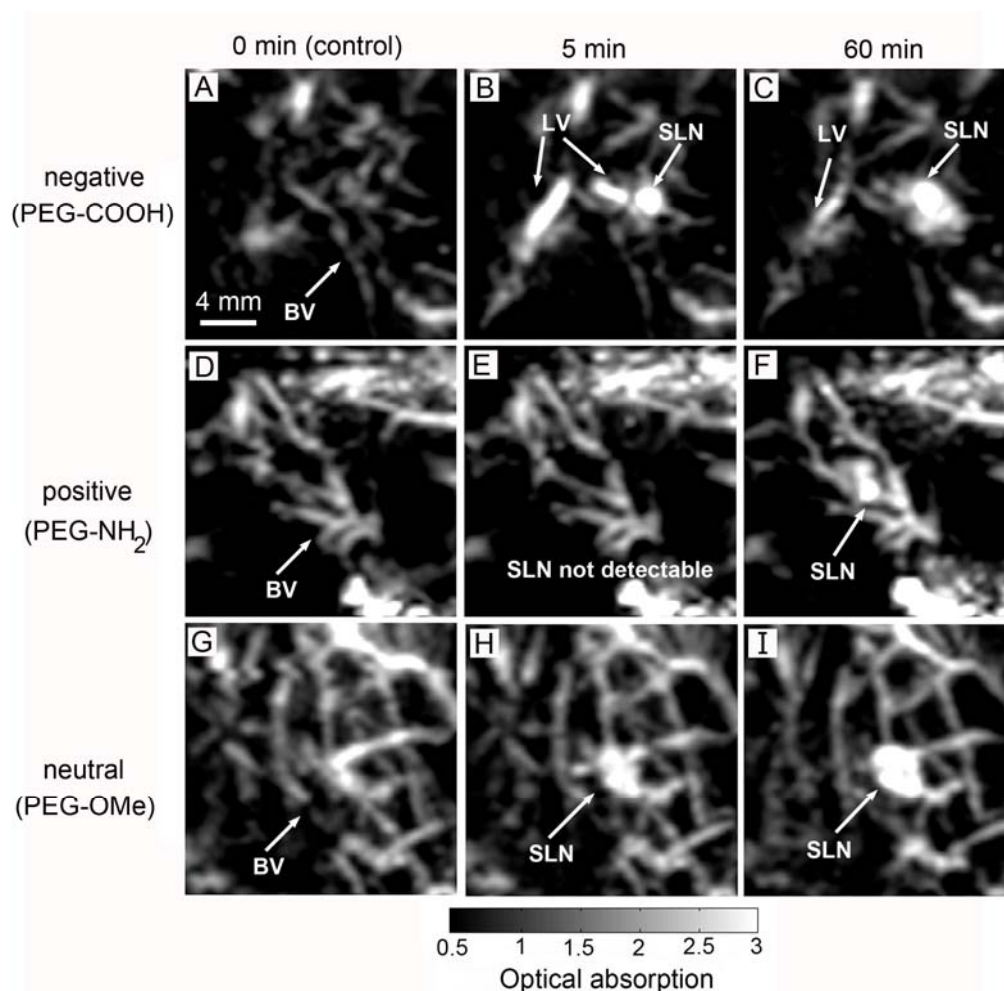


Figure 3.7. PA images acquired before, 5 min, and 60 min after the injection of AuNCs (200 pM, 100 μ L) with different surface charges. The PVP layer on the nanocages surface was replaced with SH-PEG₅₀₀₀-X, X=OMe, NH₂, or COOH to generate a neutral, positive, or negative surface charge. (A, D, G) PA images before the injection of AuNCs: (B, E, H) PA images at 5 min post injection of AuNCs with different charges. SLNs started to appear except for the case of AuNCs with positive charges. Some lymphatic vessels were also observed in the case of AuNCs with negative charges; (C, F, I) PA images at 60 min after the injection of AuNCs with different charges. BV, blood vessels; LV, lymphatic vessels; SLN, sentinel lymph node.

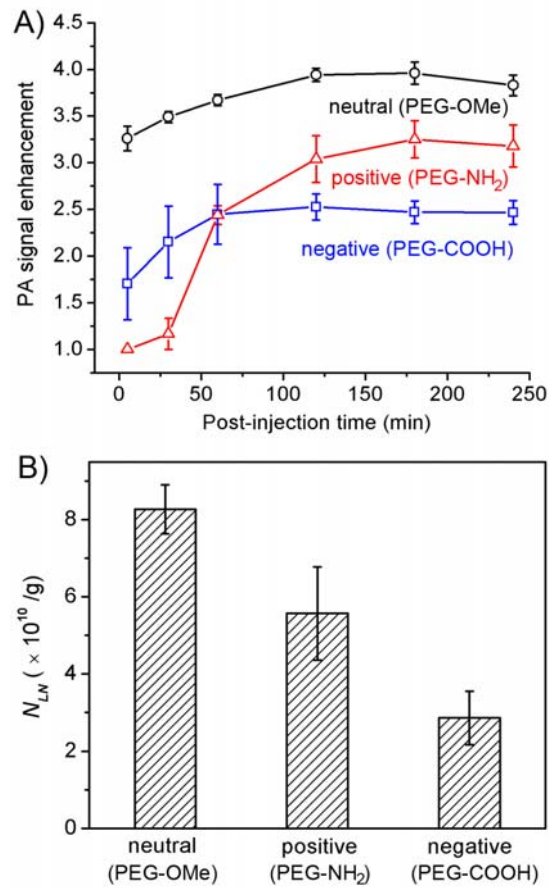


Figure 3.8. (A) PA signal enhancement in SLNs as a function of time post injection of AuNCs with different surface charges: negative (blue line), positive (red line), and neutral (black line) (n=3 rats for each group). (B) Average number of AuNCs accumulated in the SLN dissected at 4 h post injection of AuNCs with different surface charges, as measured by ICP-MS (n=3 rats for each group). Here N_{LN} denotes the number of AuNCs per unit lymph node mass (g).

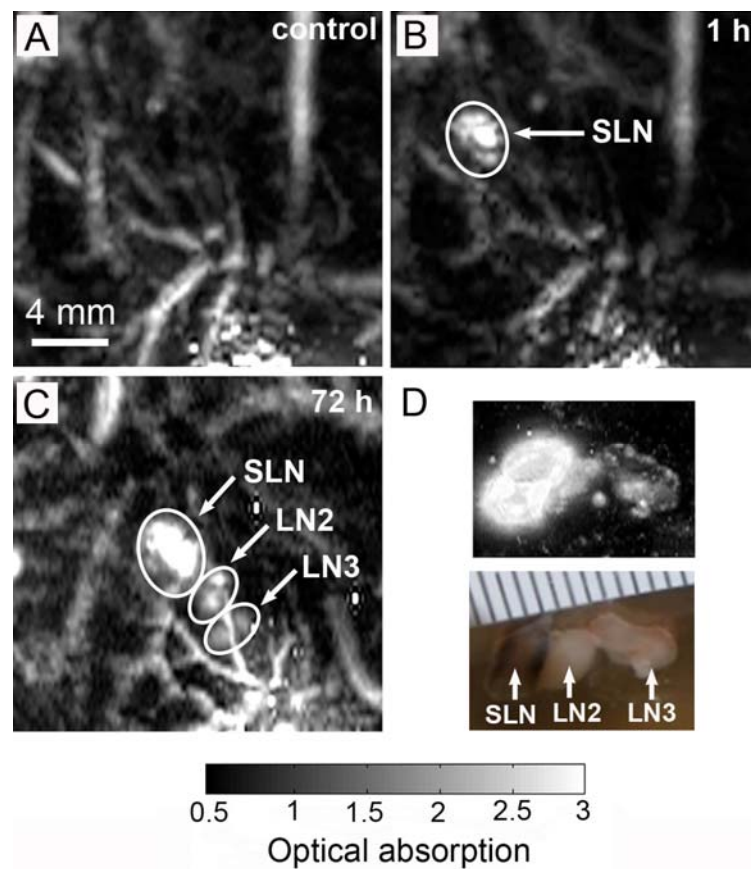


Figure 3.9. PA images acquired (A) before, (B) 1 h, and (C) 72 h after the injection of AuNCs (500 pM, 100 μ L), showing the transport of AuNCs from SLN to the second lymph node (LN2) and third lymph node (LN3). (D) *Ex vivo* PA image (top) and photograph (bottom) of dissected lymph nodes containing AuNCs. The scale of the ruler is mm/div.

3.8. Reference for Chapter 3

- [1] Alazraki, N. P.; Eshima, D.; Eshima, L. A.; Herda, S. C.; Murray, D. R.; Vansant, J. P.; Taylor, A. T. *Semin. Nucl. Med.* **1997**, *27*, 55.
- [2] Kobayashi, H.; Kawamoto, S.; Sakai, Y.; Choyke, P. L.; Star, R. A.; Brechbiel, M. W.; Sato, N.; Tagaya, Y.; Morris, J. C.; Waldmann, T. A. *J. Natl. Cancer Inst.* **2004**, *96*, 703.
- [3] Amersi, F.; Hansen, N. M. *Curr. Treat. Options Oncol.* **2006**, *7*, 141.
- [4] McMasters, K. M.; Tuttle, T. M.; Carlson, D. J.; Brown, C. M.; Noyes, R. D.; Glaser, R. L.; Vennekotter, D. J.; Turk, P. S.; Tate, P. S.; Sardi, A.; Cerrito, P. B.; Edwards, M. J. *J. Clin. Oncol.* **2000**, *18*, 2560.
- [5] Purushotham, A. D.; Upponi, S.; Klevesath, M. B.; Bobrow, L.; Millar, K.; Myles, J. P.; Duffy, S. W. *J. Clin. Oncol.* **2005**, *23*, 4312.
- [6] Krishnamurthy, S.; Sneige, N.; Bedi, D. G.; Edieken, B. S.; Fornage, B. D.; Kuerer, H. M.; Singletary, S. E.; Hunt, K. K. *Cancer* **2002**, *95*, 982.
- [7] Wang, L. V. *Nat. Photonics* **2009**, *3*, 503.
- [8] Kim, C.; Favazza, C.; Wang, L. V. *Chem. Rev.* **2010**, *110*, 2756.
- [9] Ku, G.; Wang, L. V. *Opt. Lett.* **2005**, *30*, 507.
- [10] Song, K. H.; Stein, E. W.; Margenthaler, J. A.; Wang, L. V. *J. Biomed. Opt.* **2008**, *13*, 054033-1.
- [11] Kim, C.; Song, K. H.; Gao, F.; Wang, L. V. *Radiology* **2010**, *255*, 442.
- [12] Sohrabnezhad, S.; Pourahmad, A.; Sadjadi, M. A. *Mater. Lett.* **2007**, *61*, 2311.
- [13] Skrabalak, S. E.; Chen, J.; Sun, Y.; Lu, X.; Au, L.; Cobley, C.; Xia, Y. *Acc. Chem. Res.* **2008**, *41*, 1587.

- [14] Chen, J.; Saeki, F.; Wiley, B. J.; Cang, H.; Cobb, M. J.; Li, Z. Y.; Au, L.; Zhang, H.; Kimmey, M. B.; Li, X.; Xia, Y. *Nano Lett.* **2005**, *5*, 473.
- [15] Kim, C.; Cho, E. C.; Chen, J.; Song, K. H.; Au, L.; Favazza, C.; Zhang, Q.; Cobley, C. M.; Gao, F.; Xia, Y.; Wang, L. V. *ACS Nano* **2010**, *4*, 4559.
- [16] Chen, J.; Yang, M.; Zhang, Q.; Cho, E. C.; Cobley, C. M.; Claus, C.; Kim, C.; Wang, L. V.; Welch, M. J.; Xia, Y. *Adv. Funct. Mater.* **2010**, *20*, 3684.
- [17] Song, K. H.; Kim, C.; Cobley, C. M.; Xia, Y.; Wang, L. V. *Nano Lett.* **2009**, *9*, 183.
- [18] Cho, E. C.; Kim, C.; Zhou, F.; Cobley, C. M.; Song, K. H.; Chen, J.; Li, Z.; Wang, L. V.; Xia, Y. *J. Phys. Chem. C* **2009**, *113*, 9023.
- [19] Song, K. H.; Wang, L. V. *J. Biomed. Opt.* **2007**, *12*, 060503-1.
- [20] Song, K. H.; Kim, C.; Maslov, K.; Wang, L. V. *Eur. J. Radiol.* **2009**, *70*, 227.
- [21] Soltesz, E. G.; Kim, S.; Laurence, R. G.; DeGrand, A. M.; Parungo, C. P.; Dor, D. M.; Cohn, L. H.; Bawendi, M. G.; Frangioni, J. V.; Mihaljevic, T. *Ann. Thorac. Surg.* **2005**, *79*, 269.
- [22] Moghimi, S. M.; Rajabi-siahboomi A. R. *Prog. Biophys. molec. Biol.* **1996**, *65*, 221.
- [23] Zhang, G.; Yang, Z.; Lu, W.; Zhang, R.; Huang, Q.; Tian, M.; Li, L.; Liang, D.; Li, C. *Biomaterials* **2009**, *30*, 1928.
- [24] Padera, T. P.; Kadambi, A.; di Tomaso, E.; Carreira, C. M.; Brown, E. B.; Boucher, Y.; Choi, N. C.; Mathisen, D.; Wain, J.; Mark, E. J.; Munn, L. L.; Jain, R. K. *Science* **2002**, *296*, 1883.
- [25] Kwon, S.; Sevick-Muraca, E. M. *Lymphat. Res. Biol.* **2007**, *5*, 219.

- [26] Shayan, R.; Achen, M. G.; Stacker, S. A. *Carcinogenesis* **2006**, *27*, 1729.
- [27] Stamenkovic, I. *Semin. Cancer Biol.* **2000**, *10*, 415.
- [28] Xia, X.; Yang, M.; Oetjen, L. K.; Zhang, Y.; Li, Q.; Chen, J.; Xia, Y. *Nanoscale* **2011**, *3*, 950.
- [29] Zhang, Q.; Li, W.; Wen, L. P.; Chen, J.; Xia, Y. *Chem. Eur. J.* **2010**, *16*, 10234.
- [30] Maslov, K.; Stoica, G.; Wang, L. V. *Opt. Lett.* **2005**, *30*, 625.

Chapter 4

Gold Nanocages for Controlled Release by High Intensity Focused Ultrasound (HIFU)

4.1. Introduction

Hollow nanostructures have attracted intensive attention as drug delivery systems owing to their unique capability to encapsulate and release drugs.^[1,2] Most of these structures are composed of lipids, including liposomes (uni- and multi-lamellar vesicles) and multi-channeled cubo- or hexosomes.^[3-5] Polymeric nanoparticles with various compositions, structures, and porosities have also been investigated for similar applications.^[6-9] Typically, the interiors of these hollow nanostructures are loaded with drugs (hydrophilic or hydrophobic), which escape through diffusion or degradation-triggered release. The release can also be triggered and regulated in response to environmental changes, for example, pH and temperature. Recently, inorganic and composite hollow nanostructures have also received attention for drug delivery applications. A number of groups have reported delivery systems based on mesoporous silica particles containing water-insoluble drugs,^[10,11] and metal-organic framework (MOF) particles incorporated with drugs.^[12,13] Although the inclusion of inorganic components such as metal ions may cause potential toxicity issues, it offers advantages such as multi-functionality, a feature required for future theranostic applications. For example, the metal ions can serve as contrast agents for magnetic

resonance imaging (MRI), adding a unique capability to resolve and track the *in vivo* location of a drug delivery system.^[14-16]

Hollow nanostructures of noble metals, such as Au nanocages (AuNCs), represent another attractive platform for drug delivery because it offers a great advantage of multi-functionality, a vital feature required for theranostic applications. Thanks to their strong, highly tunable scattering and absorption in the NIR from 700-900 nm, AuNCs have been successfully used as superb optical tracers or contrast agents for a variety of imaging modalities including optical coherence tomography,^[17] photoacoustic tomography,^[18-20] and multi-photon luminescence-based detection.^[21,22] Therefore, the availability of AuNCs loaded with drugs provides a great benefit to theranostic applications because the locations of nanocages can be monitored with optical imaging techniques while the drug is released at the targeted site in a controllable fashion. The surface of AuNCs can be easily functionalized with a variety of targeting moieties based on the well-established Au-thiolate chemistry, guiding the nanocages to the specific site of interest, and thus the drugs can be selectively released at the targeted region, greatly minimizing the side effect. Our previous work has demonstrated the use of AuNCs covered with smart polymers for controlled release under the irradiation of NIR laser through the photothermal effect.^[23] As expected, the released drug can greatly enhance the efficacy of photothermal cancer treatment, which has been demonstrated with success in the absence of an anticancer drug. However, a drawback of this light-triggered drug delivery system is that the penetration depth of the laser is limited by the strong light scattering of the tissue, hindering its potential use in clinical applications. Therefore,

it is critical to seek alternatives that can trigger the drug release at desirable depths.

HIFU has been a subject of interest for decades in medical research and is often considered to be attractive for cancer treatment because it is non-invasive or minimally invasive.^[24] Unlike conventional radiation therapy, there is no maximum cumulative dose for focused ultrasound, so the treatment can be repeated until a tumor is destroyed. Because of the significant acoustic energy deposition at the focus of HIFU, temperature rises rapidly, generating tissue necrosis at a small spot with pinpoint accuracy. Additionally, a local temperature rise at the focus can be used for drug delivery to a specifically targeted region with minimum side effect on the surrounding tissue.

In this chapter, I will discuss two temperature-regulated systems for controlled release by combining AuNCs with HIFU. Because HIFU can penetrate more deeply into soft tissues than NIR light, it could be a more effective external stimulus for rapid, on-demand drug release. While the NIR laser-triggered release has to rely on the photothermal effect of AuNCs, HIFU can directly deposit acoustic energy in the focal volume to rapidly raise the temperature. The first system I have developed is based on AuNCs covered with smart, thermally-responsive polymers.^[25] The polymer chains will collapse as the temperature increases beyond a certain point, opening the pores and thus releasing the pre-loaded drugs. In the second system, the hollow interiors of AuNCs were filled with a biocompatible phase-change material (PCM).^[26] The PCM would melt when the temperature was raised above its melting point, diffusing from the interiors of nanocages and concurrently releasing the drugs encapsulated in the PCM. We can remotely control the released dosage by

manipulating the power of HIFU and/or the duration of exposure. Localization and depth capability of the HIFU-controlled release have also been investigated. I believe that the AuNC-based drug delivery system can be further developed into a promising theranostic platform with multi-functionality, including the capabilities for *in vivo* molecular imaging and chemo- and photothermal therapy.

4.2. A Controlled Release System Based on Gold Nanocages Covered with Smart Polymers

4.2.1. Experimental Setup and Mechanism

Figure 4.1A shows a schematic of the experimental setup. The HIFU transducer (TX 009, Philips) was operated at a central frequency of approximately 1.6 MHz, with a focal length of 40 mm and a focal spot 0.9 mm in diameter. It was driven by a continuous sinusoidal voltage produced by a function generator (33250A, Agilent) and passed through a radiofrequency amplifier (240L, ENI). The HIFU transducer and the targeted sample were both immersed in a water bath to provide ultrasound coupling between them. Figure 4.1B illustrates how the controlled-release system works. The surface of the AuNCs was functionalized with thermally-responsive copolymers, poly(NIPAAm-*co*-AAm) (NIPAAm: N-isopropylacrylamide; AAm: acrylamide), by means of the Au-thiolate linkage. These copolymers can change conformation in response to temperature variations at a transition point known as the low critical solution temperature (LCST).^[27] When the temperature of the solution is below its LCST, the polymer is hydrophilic and solvated by water. As the

temperature increases beyond its LCST, the polymer undergoes a phase transition and becomes collapsed and highly hydrophobic. This conformational change with temperature is reversible, allowing one to control the dosage of drug release by altering the duration in which the polymer chains are kept at the high-temperature state. When a significant amount of acoustic energy is delivered to the focus using HIFU, the temperature in the focal volume of the sample increases rapidly. As the temperature rises beyond the LCST of the copolymer, the polymer chains change from a stretched conformation to a collapsed state. As a result, the pores on the nanocages are opened, releasing the chemical or drug pre-loaded in the nanocages. When HIFU is turned off, the temperature drops to its original state and the polymer chains relax back to their extended conformation, blocking the pores and thus terminating the release. The released dosage can be remotely controlled by manipulating the power and/or the duration of HIFU irradiation.

4.2.2. Synthesis of Thermally-Responsive Polymers

The smart copolymers, poly(NIPAAm-*co*-AAm), used in the present work were prepared by reversible addition-fragmentation chain transfer (RAFT) radical polymerization instead of the atom-transfer radical polymerization (ATRP) method used in our previous study.^[23] RAFT radical polymerization offers a number of advantages over ATRP: *i*) it can eliminate the tedious purification step that often involves dialysis over a long period of time; *ii*) it is free of residual Cu species (associated with the catalyst for ATRP), which could complicate their applications in biomedical research; and *iii*) copolymers prepared with RAFT show a much narrower

molecular weight distribution, with a polydispersity index (PDI) of 1.3, compared to those synthesized using ATRP (PDI >1.6). As schematically shown in Figure 4.2, RAFT copolymerization of NIPAAm and AAm monomers (at a molar feeding ratio of 9 to 1) was carried out in 1,4-dioxane at 65 °C in the presence of a disulfide-containing chain transfer agent (CTA) and 2,2'-azobis(isobutyronitrile) (AIBN, a thermal initiator). The ¹H-NMR spectra of the purified copolymers shown in Figure 4.3A clearly indicates the existence of CTA (resonances at 2.74, 2.91, and 7.10-7.30 ppm) across the copolymer backbone, with corresponding integral ratios of 1:1:2.2, further confirming a well-defined structure for the poly(NIPAAm-co-AAm) copolymers. The composition of the copolymer was determined using quantitative ¹³C-NMR spectroscopy (Figure 4.3B) through a comparison of the integral values of two types of amide carbonyls: primary amide for the AAm residue at 178.2 ppm and secondary amide for the NIPAAm residue at 174.7 ppm. From the quantitative ¹³C NMR analysis, the molar ratio between the two different repeating units was determined to be $N_{\text{NIPAAm}}/N_{\text{AAm}} \approx 9:1$, which was very close to the feeding ratio of the monomers. Furthermore, our thermo-responsive measurements showed that the LCST of the copolymer in deionized water and PBS buffer solution was 38.5 and 37.7 °C (Figure 4.4), respectively, which are between the human physiological temperature (37 °C) and hyperthermia (42 °C).

4.2.3. Surface Modification of Gold Nanocages

Figure 4.5A shows typical TEM images of the AuNCs after being functionalized with poly(NIPAAm-co-AAm). The nanocages were about 52 nm in edge length, with

a wall thickness of around 9 nm. The pores on the surface of the nanocages were, on average, 7 nm in size, and the thickness of the copolymer on the cage surface was around 3 nm in the dry state (inset of Fig. 4.5A). The hydrodynamic diameter (measured by dynamic light scattering) of the nanocages increased from 110 to 137 nm after surface functionalization with the copolymer. Also, the LSPR peak of the nanocages shifted from 754 to 780 nm (Fig. 4.5B). Both results indicate that the copolymers were successfully grafted to the surface of the nanocages.

4.2.4. HIFU-Controlled Release for the Gold Nanocages Covered with Smart Polymers

I used rhodamine 6G (R6G) as a fluorescent dye to demonstrate the capability of controlled release. This dye is similar to doxorubicin, a commonly used drug for cancer chemotherapy, in terms of molecular weight (similar size) and surface charges.^[28] Since R6G has a strong absorption peak at 527 nm, its release could be easily monitored by UV-vis spectra of the supernatants at different time points after the nanocages had been centrifuged down. To load the dye, the copolymer-covered nanocages were added to an aqueous solution of R6G and stirred at 42 °C overnight. Then, the suspension was quickly cooled with an ice bath to trigger a conformational change for the copolymer, blocking the pores and keeping the loaded dye inside the nanocages.

Figure 4.6, A and B, compares the release of R6G when the dye-loaded nanocages were heated at 40 °C and irradiated by HIFU at a power of 10 W, respectively, for different periods of time. It can be seen that the intensity of optical absorption peak

for R6G increased with the duration of heating or HIFU irradiation, indicating that the released dosage could be controlled by varying the amount of heat delivered to the system. As heating was prolonged, the total amount of R6G released into the solution kept increasing, but eventually leveled off. By referring to a calibration curve separately prepared for the same dye, I determined the exact concentration of R6G released from the nanocages at different time points, as shown in Figure 4.6C. The release profiles indicate that more dye was released within the same period of time when the release was triggered by HIFU than by conventional heating, and the release rate was also higher for the system with HIFU. The concentration of the released R6G was about 2.15 μM when exposed to HIFU for 5 min, while it took more than 20 min for the same concentration of R6G to be released by conventional heating. In addition, when HIFU was used to trigger the release, most of the dye was released in 10 min, and the concentration of the released dye increased only about 0.1 μM from 10 to 20 min, and then essentially did not change after 20 min. A control experiment of release at the human physiological temperature (37 °C) was also conducted, and no obvious release was observed (less than 0.06 μM) after the dye-loaded nanocages had been heated at 37 °C for 48 h (Figure 4.7).

4.2.5. Localization of the HIFU-Controlled Release

The fast response associated with HIFU can be attributed to the rapid local temperature rise within the focal volume achieved by the focused-ultrasound wave. Figure 4.8 shows the temperature increase measured at the focal volume of HIFU (about 4.26 μL , the focal volume was considered as a cylinder with a diameter of 0.9

mm and a height of 6.7 mm) for aqueous suspensions of AuNCs (0.1 nM) after exposure to HIFU for different periods of time and at different powers. The temperature could increase from about 35 °C to 41.2, 39.6, 37.6 °C in 1 min, and saturated at 43, 41 and 39 °C after 2 min, at powers of 10 W, 8 W, and 6 W, respectively. In addition, the rate of temperature rise increased with the power. Because more heat was generated by HIFU than conventional heating, the copolymer could maintain its conformation in an extended state for a longer period of time, keeping the pores on the nanocages open for a longer period of time to release more dye molecules.

The rapid temperature rise within the focal volume induced by HIFU can be used to trigger a highly localized release. I investigated this feasibility by using gelatin phantoms made from a mixture of gelatin solution and AuNCs pre-loaded with the dye. As described in the experimental section, the mixture was added into a petri dish to cast into a uniform, dark-blue gelatin film (inset of Figure 4.9A). The dark-blue color can be attributed to the presence of AuNCs. In a typical procedure, I first focused the HIFU on the bottom surface of the petri dish at a relatively high power (15 W) for 5 second to generate a tiny white spot, which would allow us to easily locate the release spot under a fluorescence microscope. I then reduced the power to a lower level (e.g., 10 W or a less) and moved the focal point vertically into the gelatin phantom. Figure 4.9A shows fluorescence microscopy image taken from the gelatin phantom with dye-loaded nanocages before HIFU irradiation and it served as a control. The dye molecules encapsulated in the AuNCs were not expected to fluoresce due to the quenching effect of the Au surface.^[29,30] Figure 4.9, B and C,

show two typical fluorescence microscopy images of the gelatin phantoms after exposed to HIFU at a power of 10 W for 2 and 20 min, respectively. It can be observed that only a small area around the focal volume exposed to HIFU showed release of the dye. The fluorescence intensity of the released dye was obviously increased from 2 to 20 min. The release pattern was more or less circular in each image, suggesting the involvement of dye diffusion and heat dissipation from the focal point. The contrast difference in the center of each image (the relatively dark area) was caused by the mark we generated on the bottom surface of the petri dish. We also took fluorescence microscopy images of the gelatin phantoms after exposed to HIFU at powers of 6 and 8 W, respectively, for 2, 5, 10, and 20 min. The images were similar to those in Figure 4.9, B and C, except the difference in fluorescence intensity. Figure 4.9D shows the normalized fluorescence intensity as a function of time, where the data were calculated from the fluorescence images. The average value from the image shown in Figure 4.9A was considered as the background. The corresponding fluorescence intensity of each image was obtained by eliminating the background and averaging the values of the remaining pixels. Each data point was then normalized against the average fluorescence intensity for the image of a gelatin phantom taken after exposed to HIFU at a power of 6 W for 2 min. It can be observed that the fluorescence intensity increased with the duration of time exposed to HIFU for the same power, which is consistent with the results obtained from the UV-vis measurements (shown in Figure 4.6B). At the same duration of HIFU exposure, the fluorescence intensity increased with increasing power.

4.2.6. Depth Capability of the HIFU-Controlled Release

I further evaluated the capability to release at a deep penetration depth with HIFU by adding chicken breast tissue to the top of the gelatin phantom. Figure 4.11A shows fluorescence microscopy image of the sample (containing dye-loaded AuNCs) covered with a chicken breast tissue of 15 mm thick, after HIFU irradiation at a power of 10 W for 20 min. The fluorescence intensity was reduced relative to the sample under the same experimental conditions without chicken tissue (Figure 4.9C), indicating stronger attenuation of ultrasound by soft tissue than by water. However, the release of dye was still visible as indicated the strong fluorescence signal shown in Figure 4.11A, indicating the excellent penetration ability of HIFU. The diameter of the released region was about 6 mm. When a second layer of chicken breast tissue was added (with a total thickness of 30 mm), release of the dye could still be observed, even though the fluorescence intensity was further reduced (Figure 4.11B). We did not add more layers of chicken breast tissue because the HIFU transducer we used was limited to a focal length of 40 mm. However, we believe that deeper penetration depths can be achieved by modifying the focal length of the transducer as well as by manipulating the power and irradiation time.

4.3. A Controlled Release System Based on Gold Nanocages Loaded with Phase-Change Material (PCM)

4.3.1. Mechanism

The second controlled release system we develop simply involves filling the hollow interiors of AuNCs with a PCM. The PCM was used as the medium to help load the drug, which can also serve as a “gate-keeper” to control the release of drug in response to temperature increase.^[31,32] In principle, the encapsulated drug should not be released until the PCM has been melted due to heating by a thermal, photothermal, or ultrasonic means. Figure 4.11A shows a schematic diagram of the encapsulation and release mechanisms. Since a PCM reversibly changes its physical states between solid and liquid over a narrow temperature range, it can perfectly confine drug molecules inside the AuNCs at a temperature below its melting point (the solid state). When the local temperature is raised beyond the melting point of the PCM, it will begin to melt (the liquid state) and the drug will be released from the melted PCM through diffusion. As long as the drug is miscible with the PCM phase, it can be conveniently loaded into the hollow interiors of AuNCs as the PCM diffuses into the nanocages. This requirement can be readily met by choosing PCMs with the surfactant-like behavior, such as those containing both long hydrophobic tails and hydrophilic heads. Here, we choose 1-tetradecanol, a fatty alcohol characterized by attractive features such as immiscibility with water, good biocompatibility, and a melting point (38-39 °C) slightly higher than the normal human body temperature (37.0 °C). It can also be mixed with a range of hydrophilic and hydrophobic substances. Furthermore, 1-tetradecanol is an ingredient widely used in cosmetics due to its low toxicity (oral, rat LD₅₀ >5 g/kg).^[33,34] Figure 4.11, B and C, shows TEM images of the AuNCs before and after loading of the PCM/dye mixture. Compared with the pristine sample, nanocages loaded with the PCM/dye mixture showed a

conspicuous difference in contrast.

4.3.2. HIFU-Controlled Release for the Gold Nanocages Loaded with PCM/Dye

For encapsulation, we used R6G and methylene blue (MB) as two examples of drugs with different solubilities in water. As a major advantage over most real drugs, the release of these two dyes can be easily monitored and quantified through the use of UV-vis absorption spectroscopy. The PCM and the dye molecules were loaded into the nanocages at the same time. For the loading process, in a typical experiment, the PCM was added to a glass vial and placed in an oil bath set to 90 °C to melt the PCM into a liquid, followed by the addition of a dye. After the dye and PCM had been thoroughly mixed, we introduced the AuNCs as a suspension in methanol. Even after the methanol had been evaporated due to stirring and heating, the AuNCs were still well dispersed in the liquid PCM. During this process, the mixture of PCM and dye molecules slowly entered the hollow interior of each nanocage by diffusion through the pores on the surface. After the system had been continued with heating at 90 °C for 2 h, a small amount of hot water was added to generate two separated phases, one being the PCM/dye mixture and the other containing the loaded AuNCs and water, as a result of immiscibility between the PCM and water. The AuNCs were preferentially extracted into the water phase due to their hydrophilic surfaces. Interestingly, both PCM and dye molecules inside the nanocages were effectively retained because it was difficult for the PCM molecules to quickly diffuse into water due to their immiscibility. Finally, the AuNCs encapsulated with the PCM/dye mixture were

collected by centrifugation and then re-dispersed in deionized water.

Figure 4.12 shows the release of R6G from the AuNCs by direct heating and HIFU heating, respectively. As shown in Figure 4.12A, the amount of R6G released was negligible at room temperature because the dye was entrapped by solid PCM inside the nanocages, which makes it difficult for the dye molecules to diffuse into the surrounding medium. At 37 °C, there was a slight increase in the release of R6G (still below 5% over a period of 3 days) although the melting point of 1-tetradecanol (38-39 °C) was still slightly higher than this temperature. In comparison, 28% of the encapsulated R6G was released from the AuNCs in 3 days when the sample was held at 40 °C. As an important feature, the PCM-based release could be easily regulated by controlling the temperature. We confirmed this feature by investigating the release behaviors during repeated heating-cooling cycles at temperatures below and above the melting point of 1-tetradecanol (Fig. 4.12B). Note that the release of dye was only observed when the sample was heated to 40 °C and held for 2 h.

Due to its good compatibility with both hydrophobic and hydrophilic substances, we found that the PCM could also be used as a matrix for the encapsulation and release of a drug more soluble in water than R6G. We demonstrated this capability by switching to MB, a dye more hydrophilic than R6G. In this case, we found that the loading capacity of MB was much lower than that of R6G (57% vs. 84% for the MB and R6G, respectively, see Section 4.4 for calculation of the loading capacity). As a result, the cumulative release of MB was three times higher than that of R6G (Fig. 4.12C). Since MB was quickly photo-bleached (Fig. 4.13), the cumulative release percentage corrected for bleaching showed that 80% of the loaded MB was released

in 24 h (Fig. 4.14). These results clearly demonstrate that the PCM works for chemical species with different solubilities in water, making this new system a useful platform for a wide variety of drugs. Figure 4.12D shows the release profiles of R6G as a function of the power of HIFU. As expected, the quick increase in temperature by HIFU caused the R6G to release from the hollow interiors of AuNCs. The release profile also displayed a strong dependence on the power of HIFU, making it possible to control the release dosage on demand.

4.4. Summary

In this chapter, we have successfully demonstrated two temperature-regulated drug release systems by combining the unique features of AuNCs and HIFU. The first one was based upon AuNCs covered with thermally-responsive polymers, while the second one was based upon AuNCs loaded with PCM. Localized release was demonstrated by taking fluorescence microscopy images from gelatin phantoms containing the dye-loaded AuNCs after HIFU exposure at different powers for different periods of time. Only a small region around the focal volume of HIFU showed release of the dye. In addition, by placing chicken breast tissue on top of the gelatin phantom, a penetration depth of at least 30 mm was demonstrated. We believe that the AuNC-based drug delivery system can be further developed into a promising theranostic platform with multi-functionality, including the capabilities for *in vivo* molecular imaging and chemo- and photothermal therapy.

4.5. Experimental Section

Chemicals and materials. *N*-isopropylacrylamide (NIPAAm, 99%) was obtained from Acros Organics (Thermo Fisher Science) and re-crystallized from hexane before use. Acrylamide (AAm, 99%) and 2,2'-azobis(isobutyronitrile) (AIBN, 95%) were both purchased from Aldrich and re-crystallized from methanol before use. Anhydrous diethyl ether, 3,3'-dithiodipropionic acid, 1,4-dioxane, *N,N'*-dicyclohexylcarbodiimide (DCC), 4-(dimethylamino)pyridine (DMAP), glutaric dialdehyde (50 wt%), and methanol ($\geq 99.9\%$) were obtained from Aldrich and used as received without further purification. Rhodamine 6G (R6G, Acros Organics, Thermo Fisher Science) was used as received. Benzyl 2-hydroxyethyl carbonotrithioate was synthesized according to the literature.^[35] Phosphate buffered saline (PBS) was purchased from Invitrogen, GIBCO. In all experiments, we used deionized water with a resistivity of 18 M Ω , which was prepared using an ultrapure water system (MILLIPORE).

Synthesis of disulfide-containing chain transfer agent (CTA). DCC (4.6 g, 22 mmol) and DMAP (0.25 g, 2 mmol) were added into a suspension of benzyl 2-hydroxyethyl carbonotrithioate (5.4 g, 22 mmol) and 3,3'-dithiodipropionic acid (2.1 g, 10 mmol) in 60 mL of anhydrous diethyl ether. The reaction mixture was stirred for 24 h and then filtered with celite. The filtrate was stored at 4 °C overnight and filtered with celite again. The crude product was further purified by silica gel flash column chromatography (15% ethyl acetate/hexane, v/v) to obtain the disulfide-containing CTA as yellow oil (1.6 g, 22% yield). ¹H NMR (300 MHz, CD₂Cl₂) δ 2.74 (t, *J* = 7.0 Hz, 4H), 2.92 (t, *J* = 7.0 Hz, 4H), 3.68 (t, *J* = 6.3 Hz, 4H), 4.33 (t, *J* = 6.3 Hz, 4H), 4.63 (s, 4H), 7.30-7.36 (m, 10H).

Synthesis of poly(NIPAAm-co-AAm through RAFT polymerization. Disulfide-containing CTA (50 mg, 0.08 mmol) and 1,4-dioxane (40 mL) were added into a 100 mL argon-dried Schlenk flask and magnetically stirred for 5 min to obtain a homogeneous solution. NIPAAm (4.07 g, 36 mmol), AAm (0.284 g, 4 mmol), and AIBN (2.6 mg, 16 μ mol) were added to this solution and stirred for 10 min. The reaction mixture was degassed through three cycles of freeze-pump-thaw. After the last cycle, the reaction mixture was stirred for 10 min before being immersed in a pre-heated oil bath at 65 °C to start the polymerization. After 4.5 h, the NIPAAm monomer conversion reached ~75%, as measured by analyzing the collected aliquots with ^1H -NMR spectroscopy. The polymerization was quenched by cooling the reaction flask with liquid N_2 . The copolymer was purified by precipitating it three times in 700 mL of diethyl ether at 0 °C. The precipitates were collected, washed with 200 mL of cold ether, and dried under vacuum overnight to obtain the copolymer as a yellow solid (3.0 g, 90% yield based on monomer conversion). ^1H NMR (600 MHz, CD_2Cl_2) δ 0.90 (br, $\text{N}(\text{CH}_3)_2$ Hs from the NIPAAm), 1.40 (br, copolymer backbone protons), 2.74 (t, CH_2 Hs from the CTA), 2.91 (t, CH_2 Hs from the CTA), 4.00 (br, $\text{CHN}(\text{CH}_3)_2$ Hs from the NIPAAm), 4.63 (br, 2Hs from the copolymer backbone methine terminus connected to trithiocarbonate), 6.50 (br, amide Hs from NIPAAm and AAm), 7.20 (br, Ar Hs); ^{13}C NMR (150 MHz, CD_2Cl_2) δ 23.0, 26.1, 30.6, 36.0, 41.8, 43.0, 67.6, 71.1, 125.8, 125.9, 128.8, 132.2, 136.5, 152.0, 164.8, 171.7, 174.7, 178.2.

Surface modification of AuNCs with poly(NIPAAm-co-AAm) copolymers. The AuNCs were synthesized using the galvanic replacement reaction between Ag

nanocubes and chloroauric acid in water according to our published protocol.⁷ A 5 mL aqueous suspension of AuNCs (~8 pmol) was added dropwise, at a rate of 0.2 mL/min, into a 10 mL aqueous solution of poly(NIPAAm-*co*-AAm) copolymer (425 mg) in the absence of light. The mixture was stirred at 800 rpm for 5 days at room temperature. The solution was then centrifuged at 14,000 rpm for 15 min, and the supernatant was discarded. The copolymer-covered nanocages were then washed with water four times and re-suspended in 0.6 mL water.

Loading the copolymer-covered AuNCs with a dye. The aqueous suspension (0.6 mL) of copolymer-covered nanocages was mixed with 1.0 mL of R6G solution (5 mg/mL). The mixture was vortexed and sonicated for 5 min before being immersed in a pre-heated oil bath at 42 °C. After incubation at 42 °C overnight, the mixture was cooled in an ice bath for 1 h, and then centrifuged at 14,000 rpm and 20 °C for 15 min. The supernatant was discarded, and the R6G-loaded nanocages were washed with deionized water several times, until the absorbance of the supernatant at 527 nm measured using an ultraviolet-visible (UV-vis) spectrometer was less than 0.01.

Dye release from the copolymer-coated AuNCs by conventional heating. Before dye release, the R6G-loaded AuNCs were centrifuged and the supernatant was decanted. Warm water (40 °C, 0.6 mL) was added into the sample, which was immediately vortexed and incubated in a 40 °C oil bath for increasing periods of time. At intervals, the solution was cooled with an ice bath for 5 min, followed by centrifugation at 14,000 rpm and 20 °C for 15 min. The supernatant was then taken out for UV-vis spectral measurement, after which it was returned to the sample for further interval testing.

Dye release from the copolymer-coated AuNCs by HIFU. Aqueous suspension (0.6 mL) of R6G-loaded nanocages was placed in a 1.5-mL centrifuge tube and then exposed to HIFU for different periods of time at a fixed power of 10 W. After exposure, the solution was cooled with an ice bath for 5 min, and centrifuged at 14,000 rpm and 20 °C for 15 min. The supernatant was taken out for UV-vis spectral measurement. A uniform gelatin film was cast to study the localized release of R6G by HIFU. The copolymers-covered AuNCs (loaded with dye) were mixed with an aqueous gelatin solution (10 wt%) and added to a petri dish. Glutaric dialdehyde, a cross-linker, was then added into the mixture. The petri dish was sealed with parafilm and put in the aqueous medium for HIFU treatment.

Loading AuNCs with PCM/Dye. The AuNCs dispersed in methanol were added to a dye solution (R6G or MB) in 1-tetradecanol at 50 °C, followed by increasing the temperature to 90 °C to evaporate methanol. The above mixture was stirred for 5 h and then centrifuged with hot DI water at 14,000 rpm for 5 min to obtain the AuNCs loaded with 1-tetradecanol and dye. The retrieved AuNCs were washed with cold DI water at least 8 times before the release test.

Dye Release from the PCM loaded AuNCs by heating and by HIFU. The AuNCs loaded with 1-tetradecanol and dye were added into a vial and placed in an oil bath set to the designated temperature (25, 37, or 40 °C) and heated for different periods of time. At intervals, the solution was cooled with an ice bath, followed by centrifugation at 14,000 rpm for 5 min. The supernatant was then taken out for UV-vis spectral measurement. Likewise, HIFU was used to heat the sample and trigger the dye release at different powers (4, 8, and 12 W) for different periods of time.

Estimate of loading capacity of R6G and MB in AuNCs. To obtain the mole of dye in each AuNC, a sample of AuNCs loaded with PCM and dye was added into methanol to fully dissolve the PCM and release all the dye molecules from the AuNCs. The concentration of AuNCs we used was about 1.2 nM and there were 7.2×10^{12} nanocages in each sample. The total mole of dye in the sample ($N_{\text{dye, total}}$) was obtained by comparing its peak absorbance with a calibration curve:

$$N_{\text{R6G, total}} = 5.81 \times 10^{-7} \text{ mol}$$

$$N_{\text{MB, total}} = 3.35 \times 10^{-7} \text{ mol}$$

Therefore, the mole of dye molecules encapsulated in each AuNC can be calculated as:

$$N_{\text{Au cage}} = 7.2 \times 10^{12} \text{ per sample}$$

$$N_{\text{R6G}} = N_{\text{R6G, total}}/N_{\text{Au cage}} = 8.06 \times 10^{-20} \text{ mol/cage}$$

$$N_{\text{MB}} = N_{\text{MB, total}}/N_{\text{Au cage}} = 4.65 \times 10^{-20} \text{ mol/cage}$$

These data indicate that the loading capacity of MB was about 57% of that of R6G.

Instrumentation. The ^1H , ^{13}C , and quantitative ^{13}C NMR spectra of the as-prepared copolymers were recorded on a Varian 600 MHz spectrometer with CD_2Cl_2 as solvent and internal standard. Chemical shifts were referred to the proton resonance of the solvent. Gel permeation chromatography (GPC) with *N,N*-dimethylformamide (DMF) as a mobile phase was conducted on a chromatography system (Waters, Milford, MA) equipped with an isocratic pump model 1515, a differential refractometer, model 2414, and a two-column set of Styragel HR 4 and HR 4E $5 \mu\text{m}$ DMF $7.8 \times 300 \text{ mm}$ columns. The system was equilibrated at $70 \text{ }^\circ\text{C}$ in pre-filtered DMF containing 0.05 M LiBr, a polymer solvent and eluent (flow rate set

to 1.00 mL/min). Polymer solutions were prepared at a concentration of ~ 3 mg/mL and injected at a volume of 200 μ L. Data collection and analysis were performed with Empower Pro software (Waters). The system was calibrated with poly(ethylene glycol) standards (Polymer Laboratories) ranging from 615 to 442,800 Da. The LCST of a polymer is defined as the temperature at which the light transmission of the polymer solution drops to 90% of the original value.^[27] For the poly(NIPAAm-*co*-AAm) copolymer, we measured its LCST in both deionized water and PBS buffer solution (with a concentration of ~3 mg/mL) using a Varian Cary 100 Bio UV-vis spectrophotometer. The transmittance of the polymer solution at 600 nm was recorded over temperatures ranging from 25-70 $^{\circ}$ C, while the solution was heated at a rate of 1.0 $^{\circ}$ C/min.

TEM images were obtained with a Technai G2 Spirit microscope operated at 120 kV (FEI, Hillsboro, OR). Samples were prepared by dropping an aqueous suspension of particles on carbon-coated copper grids and drying at ambient temperature. The concentration of AuNCs was determined using an inductively coupled plasma mass spectrometer (ICP-MS, Perkin Elmer): the concentration of Au ions was converted to the concentration of nanocages once the geometric dimensions of the nanocage had been determined from TEM images. Hydrodynamic diameters for the polymer-covered AuNCs in aqueous solutions were determined using dynamic light scattering (DLS) with a Malvern Nano ZS DLS system (Malvern Instrument, Westborough, MA). UV-vis extinction spectra were recorded using a Cary 50 spectrometer (Varian, Palo Alto, CA). Fluorescent micrographs were taken using a QICAM Fast Cooled Mono 12-bit camera (Q Imaging, Burnaby, BC, Canada) attached to an Olympus

microscope with Capture 2.90.1 (Olympus). All the images were taken with the same exposure parameters.

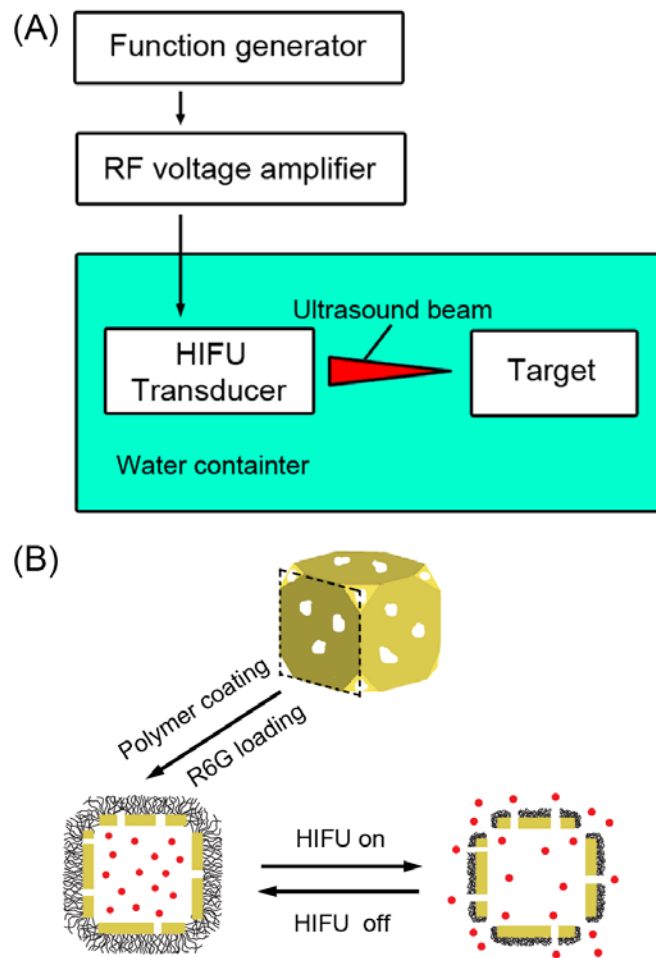


Figure 4.1. Schematic illustrations showing (A) setup for the high-intensity focused ultrasound (HIFU) experiments, (B) how the controlled-release system works.

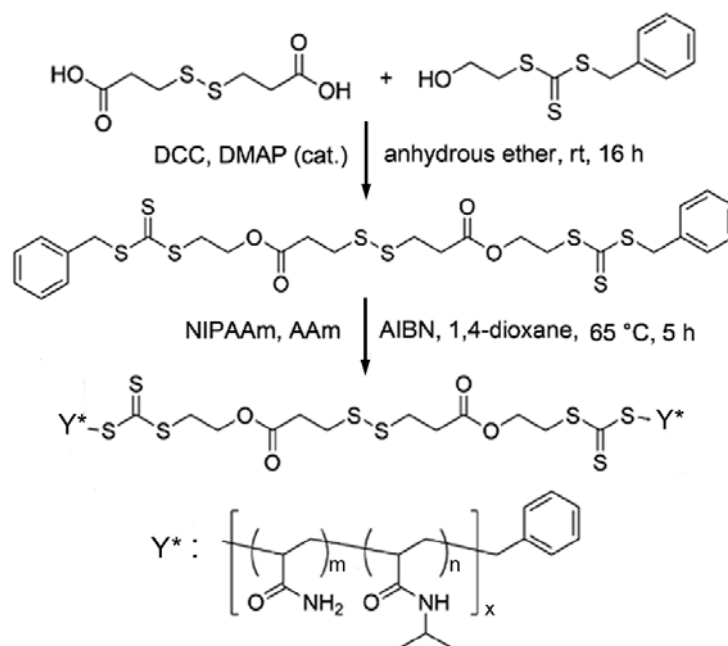


Figure 4.2. Procedure for the synthesis of poly(NIPAAm-co-AAm) copolymers through RAFT copolymerization. DCC: *N,N'*-Dicyclohexylcarbodiimide; DMAP: 4-Dimethylaminopyridine.

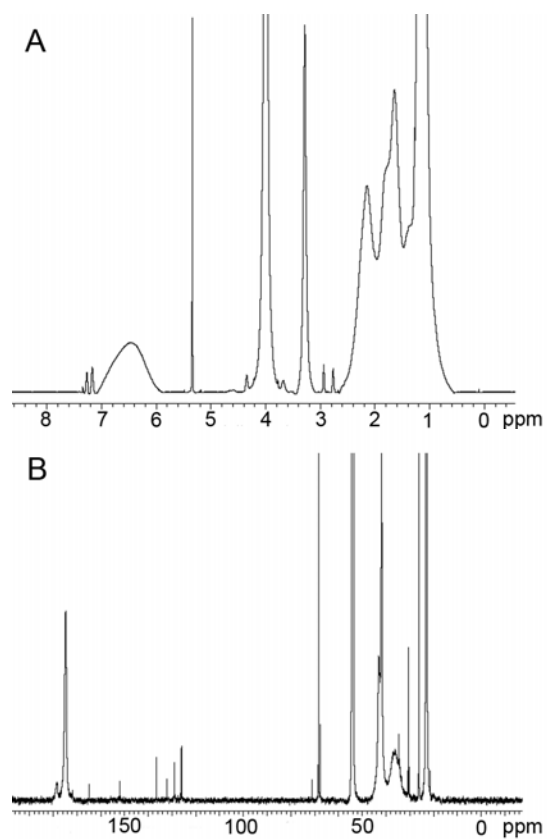


Figure 4.3. (A) ^1H -NMR and (B) quantitative ^{13}C NMR spectra of the as-prepared poly(NIPAAm-*co*-AAm) copolymers.

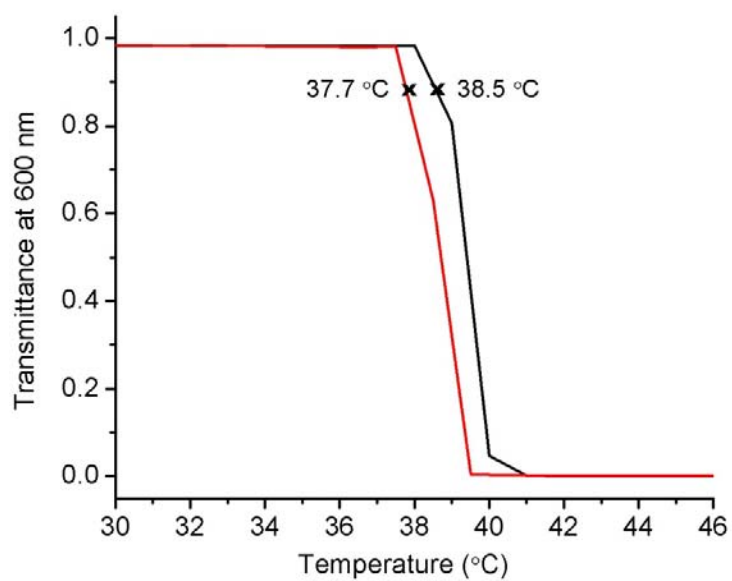


Figure 4.4. The LCST measured spectrophotometrically, with the solution being heated at a rate of 1.0 °C/min. The measurement was conducted in water (black line) and PBS buffer (red line), respectively. The temperature at 90% light transmittance (at 600 nm) of the original polymer solution was defined as the LCST.

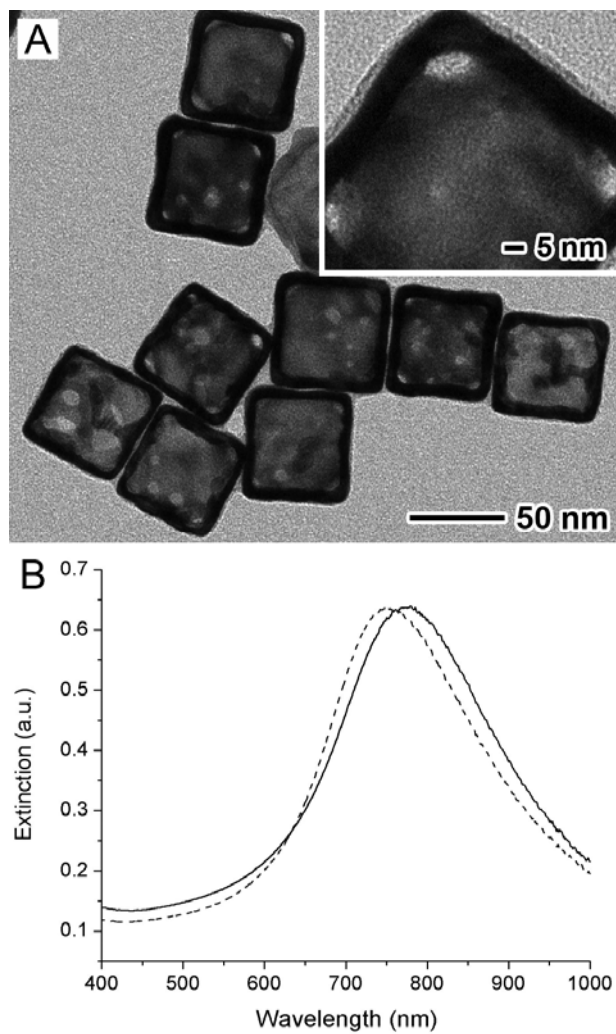


Figure 4.5. TEM images of (A) the AuNCs functionalized with poly(NIPAAm-*co*-AAm). The inset of (A) shows a magnified TEM image of the corner region of such a nanocage. (B) UV-vis extinction spectra of an aqueous suspension of AuNCs before (dashed line) and after functionalization with poly(NIPAAm-*co*-AAm) copolymers (solid line).

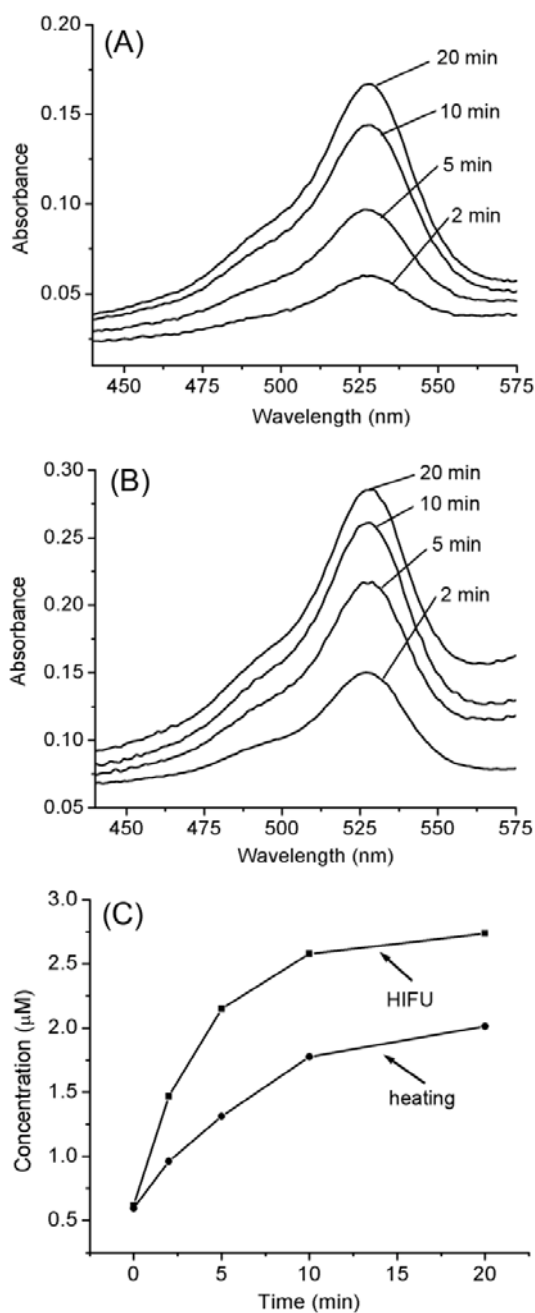


Figure 4.6. Controlled release of R6G from AuNCs covered by a copolymer with an LCST at 38.5 °C. The absorption spectra were taken after the samples had been (A) heated at 40 °C for 2, 5, 10, and 20 min and (B) exposed to HIFU at a power of 10 W for 2, 5, 10, and 20 min. (C) A comparison of the concentration profiles of R6G released from the nanocages triggered by conventional heating and HIFU, respectively.

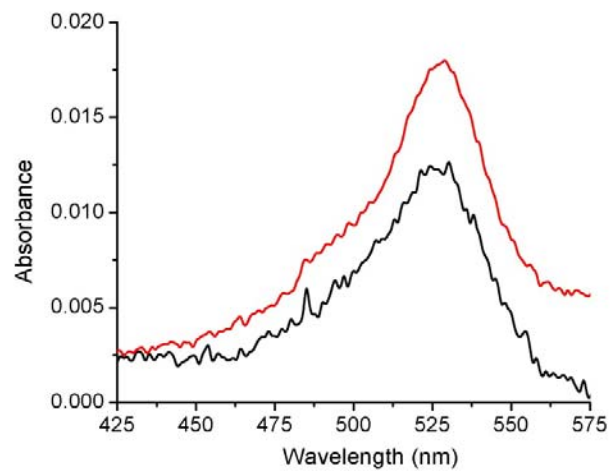


Figure 4.7. The absorption spectra taken before the release (black line) and after the samples had been heated at 37 °C for 48 h (red line).

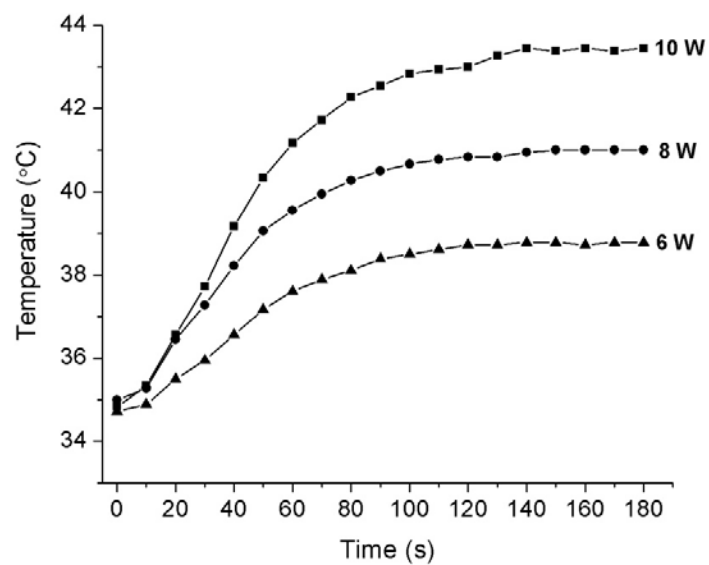


Figure 4.8. The changes in temperature measured at the focal volume of HIFU for aqueous suspensions of AuNCs (0.1 nM) after exposed to HIFU at different powers for different periods of time.

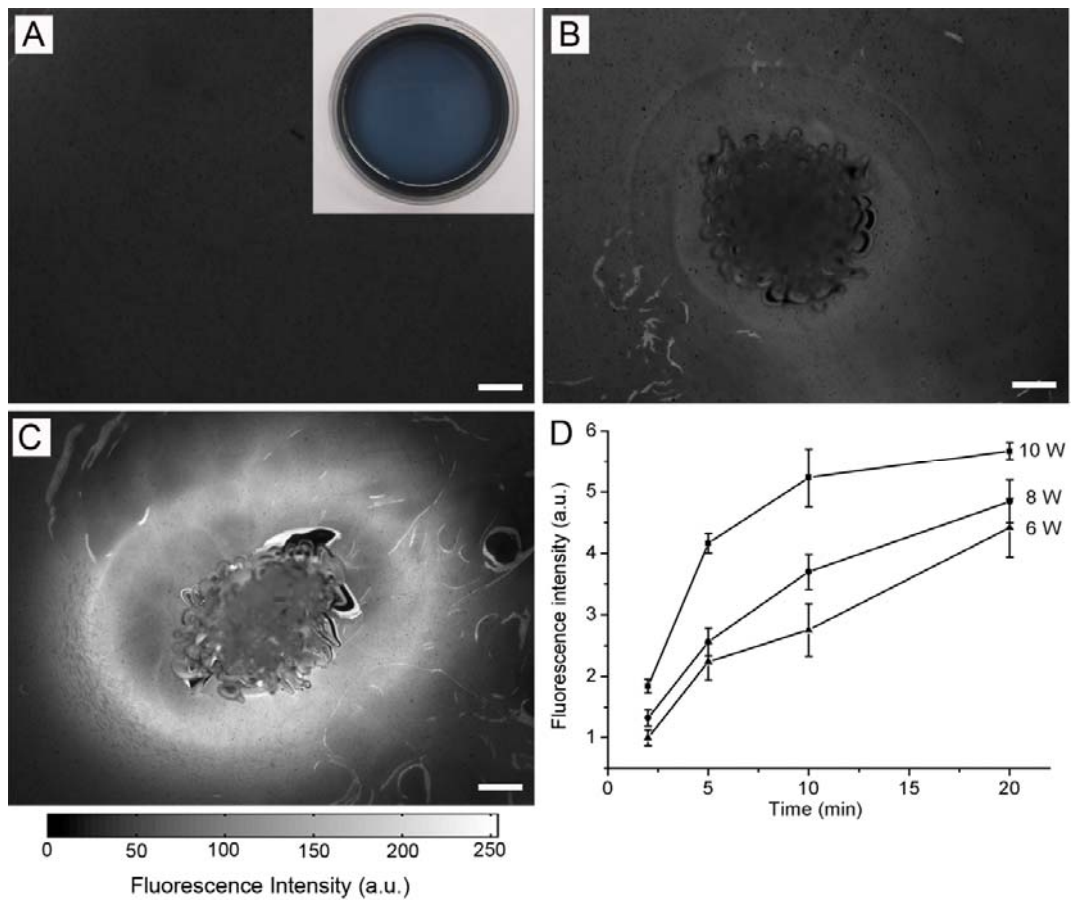


Figure 4.9. Fluorescence microscopy images of the gelatin phantom with dye-loaded AuNCs (A) before and (B, C) after exposure to HIFU at a power of 10 W for 2 and 20 min, respectively. The scale bar corresponds to 500 μm , and applies to all images. The inset of (A) shows a photograph of the gelatin phantom in a petri dish prepared from a mixture of gelatin solution and AuNCs pre-loaded with the dye. (D) The normalized fluorescence intensity as a function of time calculated from fluorescence microscopy images of the gelatin phantoms after exposure to HIFU for different periods of time (2, 5, 10, and 20 min) and at different powers (6, 8, and 10 W). Each data point represents three measurements and was obtained by normalizing against the average fluorescence intensity of the sample exposed to HIFU at a power of 6 W for 2 min.

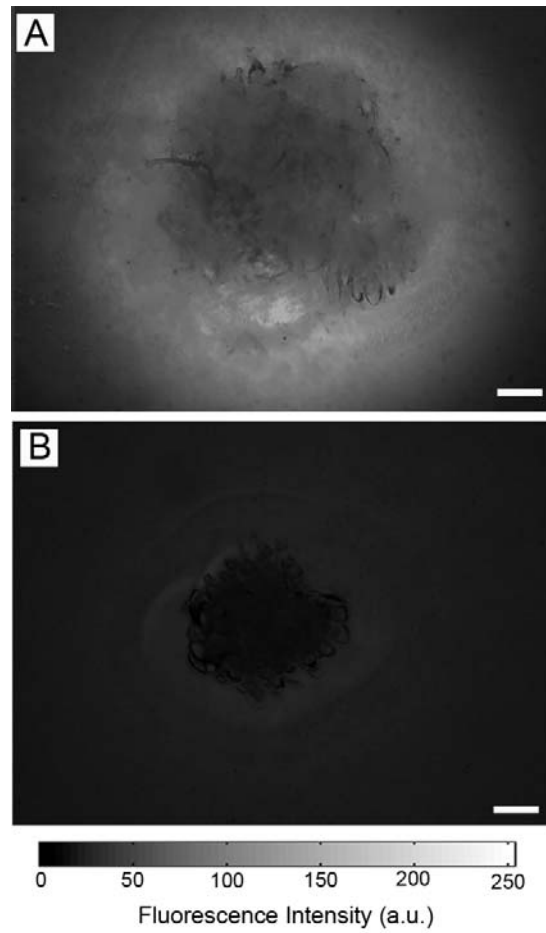


Figure 4.10. Fluorescence microscopy images of the gelatin phantoms that were covered with chicken breast tissues of two different thicknesses and then exposed to HIFU: (A) 15 mm and (B) 30 mm. The scale bars correspond to 500 μm .

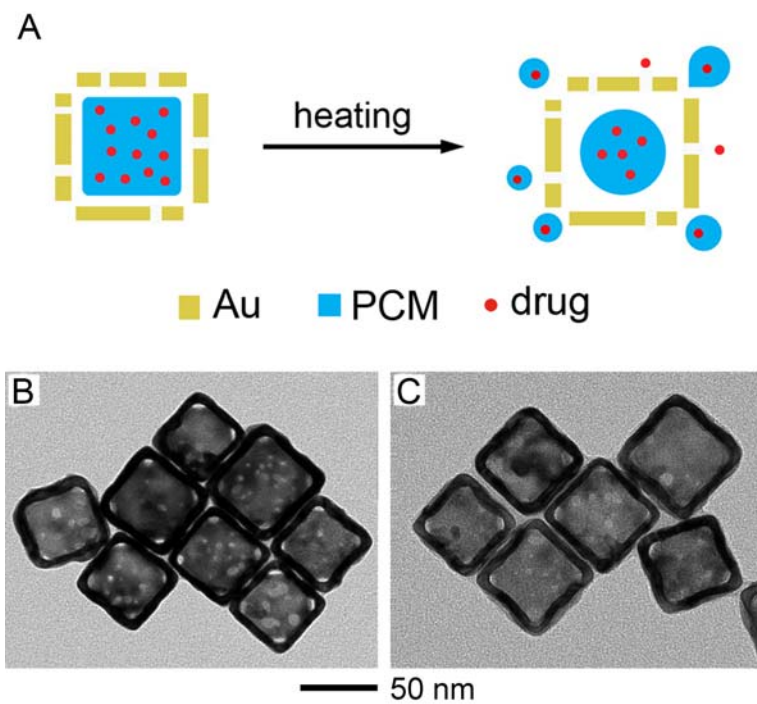


Figure 4.11. (A) Schematic illustrating the release of drugs from AuNCs loaded with a drug-doped PCM. TEM images of (B) the as-prepared AuNCs and (C) AuNCs after loading with 1-tetradecanol and R6G.

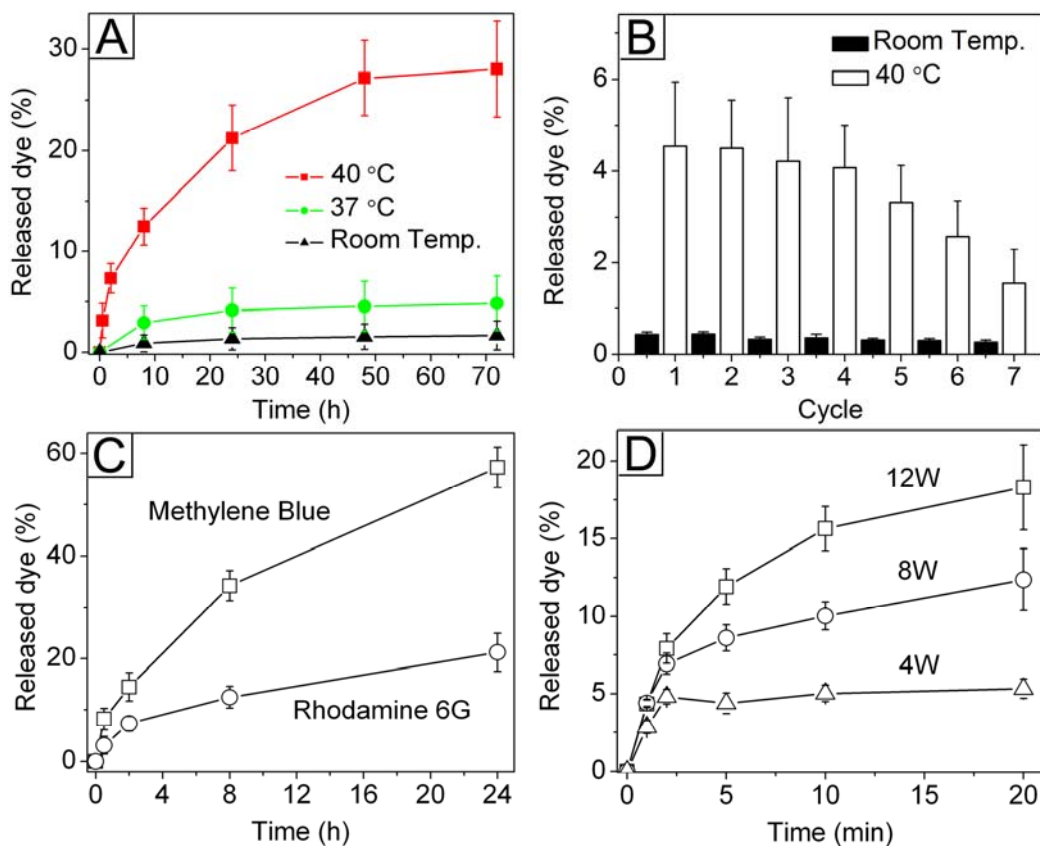


Figure 4.12. Release profiles of (A) R6G under direct heating to various temperatures for different periods of time, (B) R6G through different cycles of heating (40 °C, for 2 h) and cooling (to room temperature), (C) R6G and MB by direct heating to 40 °C for different periods of time, and (D) R6G by HIFU at different applied powers.

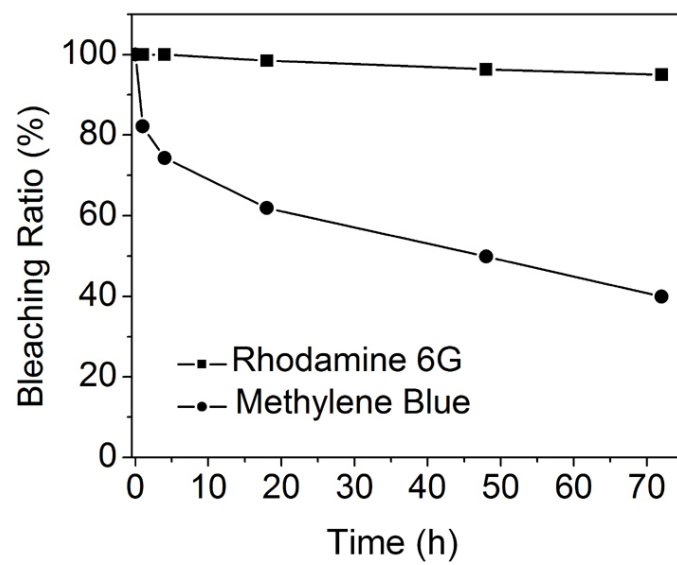


Figure 4.13. Photobleaching ratio of R6G and MB in aqueous solutions as a function of exposure time at room temperature.

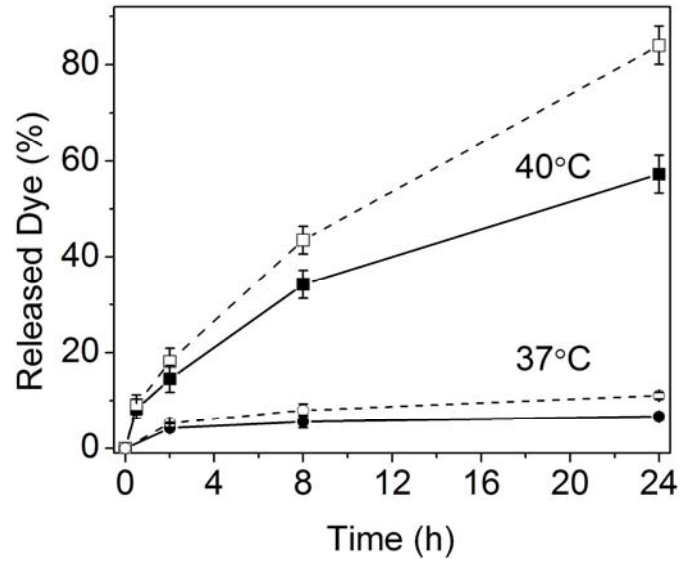


Figure 4.14. Release profiles of MB at 37 °C and 40 °C. The solid lines represent experimental data and the dashed lines are the release profiles corrected by considering photobleaching of MB.

4.6. References for Chapter 4

- [1] Lou, X. W.; Archer, L. A.; Yang, Z. *Adv. Mater.* **2008**, *20*, 3987.
- [2] Li, Z.-Z.; Wen, L.-X.; Shao, L.; Chen, J.-F. *J. Control. Release* **2004**, *98*, 245.
- [3] Lasic, D. D. *Trends Biotechnol.* **1998**, *16*, 307.
- [4] Drummond, D. C.; Meyer, O.; Hong, K.; Kirpotin, D. B.; Paapahadjopoulos, D. *Pharmacol. Rev.* **1999**, *51*, 691.
- [5] Zamboni, W. C. *Oncologist* **2008**, *13*, 248.
- [6] Nasongkla, N.; Be, E.; Ren, J.; Ai, H.; Khemtong, C.; Guthi, J. S.; Chin, S.-F.; Sherry, A. D.; Bothman, D. A.; Gao, J. *Nano Lett.* **2006**, *6*, 2427.
- [7] Medina, S. H.; El-Sayed, M. E. H. *Chem. Rev.* **2009**, *109*, 3141.
- [8] De Cock, L. J.; De Koker, S.; De Geest, B. G.; Grooten, J.; Vervaet, C.; Remon, J. P.; Sjihorukov, G. B.; Antipina, M. N. *Angew. Chem. Int. Ed.* **2010**, *49*, 2.
- [9] Tong, R.; Christian, D.A.; Tang, L.; Cabral, H.; Baker, J.R. Jr.; Kataoka, K.; Discher, D.; Cheng, J. *MRS Bulletin*, **2009**, *34*, 422.
- [10] Rosenholm, J. M.; Peuhu, E.; Eriksson, J. E.; Sahlgren, C.; Linden, M. *Nano Lett.* **2009**, *9*, 3308.
- [11] Wang, Y.; Yan, Y.; Cui, J.; Hosta-Rigau, L.; Heath, J. L.; Nnice, E. C.; Caruso, F. *Adv. Mater.* **2010**, *22*, 4293.
- [12] Horcajada, P.; Serre, C.; Vallet-Regi, M.; Sebban, M.; Taulelle, F.; Ferey, G. *Angew. Chem. Int. Ed.* **2006**, *45*, 5974.
- [13] Uemura, K.; Kitagawa, S.; Kondo, M.; Fukui, K.; Kitaura, R.; Chang, H.-C. Mizutani, T. *Chem. Eur. J.* **2002**, *8*, 3586.

- [14] Lin, W.; Hyeon, T.; Lanza, G. M.; Zhang, M.; Meade, T. J. *MRS Bulletin*, **2009**, 34, 441.
- [15] Que, E. L.; Chang, C. J. *Chem. Soc. Rev.* **2010**, 39, 51.
- [16] Della Rocca, J.; Lin, W. *Eur. J. Inorg. Chem.* **2010**, 3725.
- [17] Chang, H.; Sun, T.; Li, Z. Y.; Chen, J.; Wiley, b. J. Xia, Y.; Li, X. *Opt. Lett.* **2005**, 30, 3048.
- [18] Kim, C.; Cho, E. C.; Chen, J.; Song, K. H.; Au, L.; Favazza, C.; Zhang, Q.; Cobley, C. M.; Gao, F. Xia, Y.; Wang, L. V. *ACS Nano* **2010**, 4, 4559.
- [19] Yang, X.; Skrabalak, S.; Li, Z.; Xia, Y.; Wang, L. V. *Nano Lett.* **2007**, 7, 3798.
- [20] Song, K. H.; Kim, C.; Cobley C. M.; Xia, Y.; Wang, L. V. *Nano Lett.* **2009**, 9, 183.
- [21] Au, L.; Zhang, Q.; Cobley, C. M.; Gidding, M.; Schwartz, A. G.; Chen, J.; Xia, Y. *ACS Nano* **2010**, 4, 35.
- [22] Tong, L.; Cobley, C. M.; Chen, J.; Xia, Y.; Cheng, J.-X. *Angew. Chem. Int. Ed.* **2010**, 49, 3485.
- [23] Mustafa, S. Y.; Cheng, Y.; Chen, J.; Cobley, C. M.; Zhang, Q.; Rycenga, M.; Xie, J.; Kim, C.; Song, K. H.; Schwartz, A. G.; Wang, L. V.; Xia, Y. *Nat. Mater.* **2009**, 8, 935.
- [24] Kennedy, J. E.; ter Haar, G. R.; Cranston, D. *Brit. J. Radiol.* **2003**, 76, 590.
- [25] Li, W.; Cai, X.; Kim, C.; Sun, G.; Zhang, Y.; Deng, R.; Yang, M.; Chen. J.; Achilefu, S.; Wang, L. V.; Xia, Y. *Nanoscale* **2011**, 3, 1724.
- [26] Moon, G. D.; Choi, S. -W.; Cai, X.; Li, W.; Cho, E. C.; Jeong, U.; Wang, L. V.; Xia Y. *J. Am. Chem. Soc.* **2011**, 133, 4762.

- [27] Hoffman, A. S. *Adv. Drug Deliv. Rev.* **2002**, *43*, 3.
- [28] Wu, E. C.; Park, J. H.; Park, J.; Segal, E.; Cunin, F.; Sailor, M. J. *ACS Nano* **2008**, *2*, 2401.
- [29] Mayilo, S.; Kloster, M. A.; Wunderlich, M.; Lutich, A.; Klar, T. A.; Nichtl, A.; Kürzinger, K. F.; Stefani, D.; Feldmann J. *Nano Lett.* **2009**, *9*, 4558.
- [30] Dulkeith, E.; Morteani, A. C.; Niedereichholz, T.; Klar, T. A.; Feldmann J. *Phys. Rev. Lett.* **2002**, *89*, 203002.
- [31] Mondal, S. *Appl. Therm. Eng.* **2007**, *28*, 1536.
- [32] Choi, S.-W.; Zhang, Y.; Xia, Y. *Angew. Chem. Int. Ed.* **2010**, *49*, 7904.
- [33] Gosselin, R. E.; Hodge, H. C.; Smith, R. P.; Gleason, M. N. *Clinical Toxicology of Commercial Products*. 4th ed.; Baltimore: Williams and Wilkins, **1976**, p.II-118.
- [34] MSDS ALCH 414-1.
- [35] Hales, M.; Barner-Kowollik, C.; Davis, T. P.; Stenzel, M. H. *Langmuir* **2004**, *20*, 10809.